Study on fatigue crack initiation and propagation mechanisms in Al based cast hybrid metal matrix composite reinforced with SiC particles and Al_2O_3 whiskers

SiC 粒子とアルミナウィスカでハイブリッド強化された Al 鋳造合金の疲労き裂発生および進展機構に関する研究

2013 年 9 月

埼玉大学大学院理工学研究科（博士後期課程）

理工学専攻（主指導教員：荒居善雄）

AKM Asif Iqbal

Study on fatigue crack initiation and propagation mechanisms in Al based cast hybrid metal matrix composite reinforced with SiC particles and Al_2O_3 whiskers

A Dissertation submitted to the Saitama University in fulfillment of the requirements for the degree of Doctor of Philosophy

In

Mechanical Engineering and Science

By

AKM Asif Iqbal

Examining Committee:

Prof. Yoshio ARAI

Prof. Kenichiro HORIO

Prof. Kensuke KAGEYAMA

Prof. Wakako ARAKI

Graduate School of Science and Engineering

Saitama University, Japan

September 2013

Dedicated to

Md. Azizul Haque
&
Kawsari Zannat

My beloved parents whose inspiration boosted me up to a position I am here now.

ABSTRACT

The development of metal matrix composites (MMCs) has set the stage for a new revolution in materials. The cast hybrid MMC reinforced with 21 vol% of SiC particles and 9 vol% of Al_2O_3 whiskers is developed to use as a brake disc of high speed rail way coach. The fatigue properties of this material are of critical interest as MMC materials suffer cyclic plastic deformation in the structural applications. When a component is subjected to relatively high cyclic loads, high densities of microcracks form simultaneously. From one crack, a larger crack grows that eventually propagates and causes failure. Elucidating the mechanisms of the initiation and growth of this main crack are essential to understanding and predicting the fatigue life of a material. Therefore, the evaluation of fatigue life and the fracture mechanism of cast hybrid MMC have been proposed in this research. The initiation mechanism of fatigue microcracks and stage by stage growth till to final failure as well as fatigue crack growth in the near-threshold and stable-crack-growth regions were examined in three different types of materials: cast hybrid MMC (SiC_p+ Al_2O_3 whisker), cast MMC with Al_2O_3 whisker and monolithic cast Al alloy. The effect of hybrid reinforcement on the fatigue crack initiation and propagation mechanisms were explained through the comparison of the observed mechanism in the three materials. Conventional three point bending fatigue tests were performed in a rectangular bar smooth specimen. The plastic replica technique was used to observe the initiation and early propagation of microcracks at various times during the fatigue life. The tensile and fracture surfaces were comprehensively examined using scanning electron microscopy (SEM) and energy-dispersive x-ray spectroscopy (EDS) to characterize the crack initiation site. In Al alloy,

microcracks were observed to initiate in the Al grain, but when the matrix was reinforced, the initiation location changed to the whisker–matrix and particle–matrix interfaces and the hybridization effect reduced the resistance to crack initiation. Moreover, the two MMC materials exhibited similar interface debonding in fracture, which created additional secondary microcracks due to continued fatigue cycling. Numerous voids were formed ahead of the crack tip, and the microcracks intersected with other nearby microcracks. However, in the Al alloy, the microcracks propagated through the boundaries between Si particle clusters and the Al grain through void nucleation and coalescence or through striation formation in the Al grain. To observe the fatigue crack growth (FCG) in the near-threshold and stable-crack growth regions in hybrid MMC during high cycle fatigue, experiments were carried out on rectangular bar single edge notched specimen in accordance with the guidelines in ASTM E647. The hybrid MMC showed a higher threshold stress intensity factor range, ΔK_{th}, than the MMC with Al_2O_3 whisker and Al alloy, indicating better resistance to crack growth in a lower stress intensity factor range, ΔK. This effect occurred due to the higher roughness induced crack closure in hybrid MMC. Moreover, in the near-threshold region with decreasing ΔK, the two composite materials exhibited similar debonding of the reinforcement–matrix interface due to the modulus mismatch followed by void nucleation and coalescence in the Al matrix. At higher ΔK in the stable- or mid-crack-growth region, in addition to the debonding of the particle–matrix and whisker–matrix interface caused by cycle-by-cycle crack growth on the interface, the FCG occurred predominantly by striation formation in the Al matrix. Moreover, void nucleation and coalescence in the Al matrix and transgranular fracture of SiC particles and Al_2O_3 whiskers at high ΔK were also observed as the local unstable fracture mechanisms.

However, the FCG of the monolithic Al alloy was dominated by void nucleation and coalescence at lower ΔK, whereas the FCG at higher ΔK was controlled mainly by striation formation in the Al grains followed by void nucleation and coalescence in the Si clusters. In order to validate the experimental results, numerical analysis was conducted by using finite element method (FEM) to observe the characteristics of the elastic-plastic stress field in the clustering and non-clustering regions of cast hybrid MMC. The numerical analysis confirmed that the high stress was developed in the reinforcements located in the clustering region and stress concentration occurred on the particle–matrix interfaces. Moreover, the high volume fraction reinforced hybrid clustering region is found to be highly vulnerable to initiate crack in cast hybrid MMC during low cycle fatigue.

ACKNOWLEDGEMENTS

I would like to express my sincere thanks and gratitude to my supervisor, Prof. Yoshio ARAI whose invaluable advice and guidance in all stages of this research has made this work possible. His intelligent supervision with continuous and overflowing enthusiasm, unrelenting efforts, great patience and invaluable inputs made it easy to put the research ideas in the form that this dissertation presents. He has introduced me to the challenge and excitement of this topic. He has attempted to teach me the rigors and discipline needed to be a good researcher and I will value these lessons always.

I would like to express my sincere thanks and gratitude to Prof. Wakako ARAKI, for her valuable suggestion, constructive criticism and continuous encouragement throughout the period of this research work. I am deeply grateful to my dissertation committee members, Prof. Kenichiro HORIO and Prof. Kensuke KAGEYAMA for graciously agreeing to review this dissertation, and their helpful comments. My special appreciation is extended to Mr. Toyomi Uchiyama for his kind help during the study. Sincere thanks to all the members of strength of materials laboratory, with whom I spent a colorful life in Japan. In addition, I would like to acknowledge the Ministry of Education, Science, Sports and Culture of the Government of Japan for providing financial assistance during this research work.

Finally, the patience, adoration, sympathy and empathy extended to me by my family members including my parents, my beloved wife Begum Mustari and dearest daughter Hridita Nawrin were also a source of inspiration for completing the dissertation in final form.

TABLE OF CONTENTS

LIST OF FIGURES

LIST OF TABLES

CHAPTER-1

INTRODUCTION

1.1 Background

In recent years, stringent requirements of materials quality in automotive and aerospace industries have necessitated the development of lightweight materials. In order to obtain more efficient product for structural applications, it is necessary to improve wear and fatigue behaviour, weight reduction, high thermal conductivity, low coefficient of thermal expansion of the materials. Therefore, metal matrix composites (MMCs) have been widely considered as the possible substitute which could comply with those characteristics.

The development of MMCs has set the stage for a new revolution in materials. A metal matrix composite (MMC) combines into a single material a metallic base with a distinct phase of reinforcing constituent, which is usually non-metallic and is commonly a ceramic. The reinforcements can be either particles or fibers or the combination of both. The MMC materials can be classified according to the type and contribution of reinforcement component on the metallic matrix as:

- Particle reinforced MMCs.
- Short fiber/whisker reinforced MMCs
- Continuous fiber/whisker reinforced MMCs.
- Monofilament reinforced MMCs.

These composites, which possess higher stiffness, strength-to-weight ratio and wear resistance when compared with unreinforced matrices, have been cited for eventual use in

many structural, tribological and environmental applications. Recently, MMCs have become attractive materials for structural applications such as aerospace, automotive industry and wear applications, especially in the frictional area of braking systems because of their great advantages and mechanical performance. The major advantages of MMCs compared to unreinforced material are as follows:

- Greater strength
- Improved stiffness
- Reduced density (weight)
- Improved high temperature properties
- Controlled thermal expansion coefficient
- Improved abrasion and wear resistance
- Improved damping capability

The above advantages made these MMC materials more and more attractive and alternative in the engineering applications. The reinforcement and the matrix system for the MMCs are mainly determined by the intended application of the composites. For example, high thermal conductivity with improved ductility is needed for the MMC materials used in the frictional area e.g. brake disc rotor. Therefore, ceramics and high toughness aluminium should be chosen as reinforcement and matrix respectively. Besides, the combined application of two or more reinforcement is possible by using hybrid techniques. A brake disc structure made by partially reinforced MMC is shown in Fig. 1.1. Despite their great advantages, the high production cost, poor ductility and low toughness of MMCs are the major barriers for their structural applications. For minimizing these limitations, a clear

understanding of the micro-mechanisms of damage characteristics of MMCs is necessary to design the microstructure of these materials. Many researchers have investigated the damage characteristics of MMCs during the past few decades [1-64]. According to their study, Fabrication process of the MMCs plays an important role to minimize the limitation (high cost, low toughness) in the structural applications. The MMC materials can be manufactured by many different techniques [1, 2]. The fabrication techniques basically divided into two categories:

(1) Solid state includes powder metallurgy and diffusion bonding and

(2) Liquid state includes infiltration, dispersion and spraying.

MMCs of commercial applications are now produced by the liquid state process because of the following advantages over the solid state process:

- Less expensive.
- Liquid metal is easier to handle than are powders.
- Complex shape can be produced by liquid state process.

Among the various types of the liquid state fabrication techniques, squeeze casting have now become one of the most feasible techniques for the production of low cost MMCs and complex shape components [2]. The emergence of squeeze casting as a production process has given materials and process engineers a new alternative to traditional approaches of casting and forging [3, 4]. Squeeze casting is the process designating solidification of liquid metal under pressure. Pressure during solidification helps to achieve zero defects with improved metallurgical properties. Additionally, compared to another casting method e.g. gravity or die casting, a wide range of alloy can be cast using squeeze casting. Preparation

of the whisker/particle perform is an important step in the fabrication of MMCs by squeeze casting method. Reinforcement breakage, porosity, inhomogeneous reinforcement orientation and bad interfacial bonding in the composites are the barriers to obtain adequate strength and mechanical properties of MMCs.

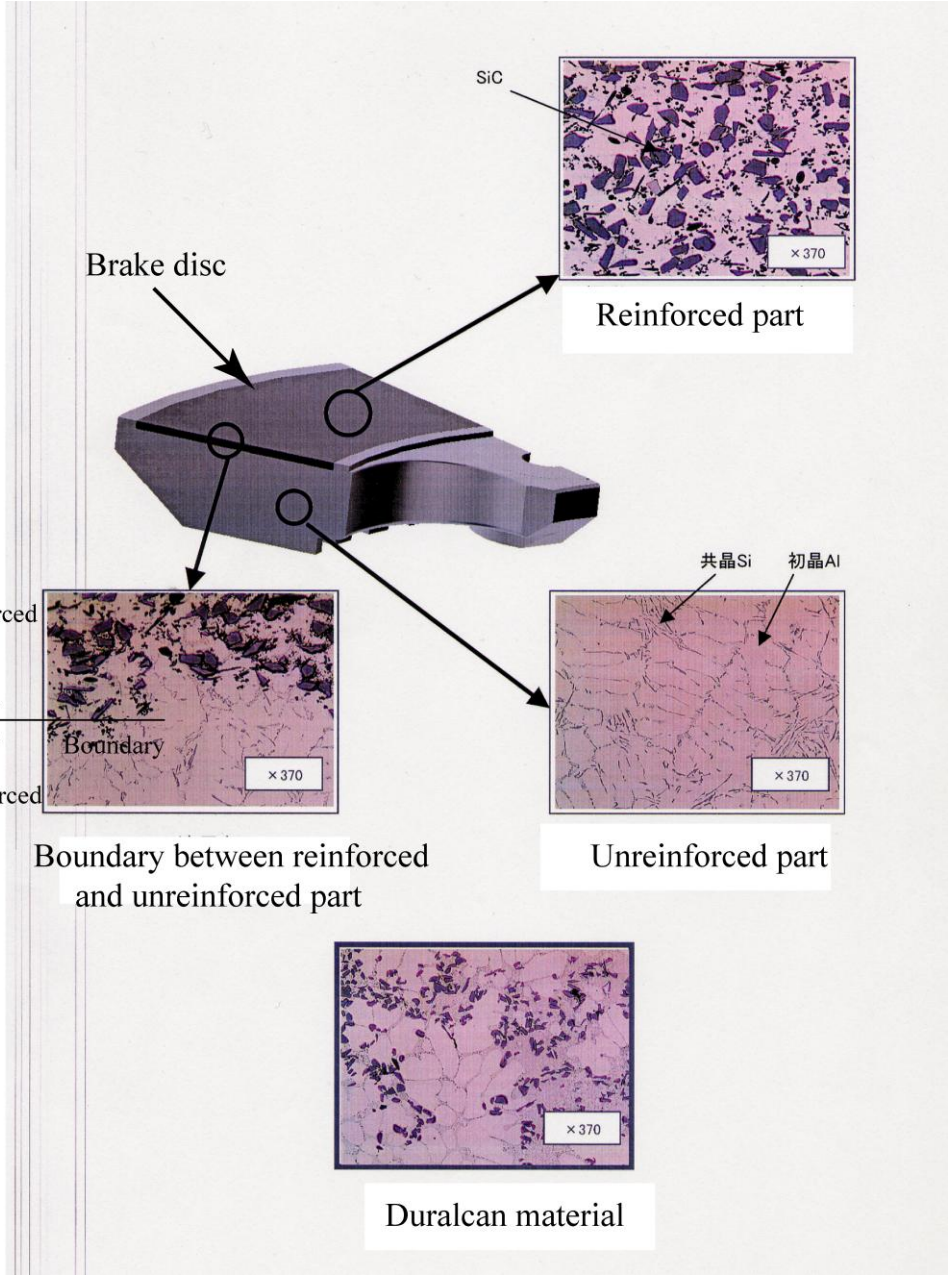

Fig. 1.1 Brake disc structure made by partially reinforced MMC

1.2 Application of MMCs

In the past 15-20 years, MMCs have emerged as a class of materials capable of advanced structural, aerospace, automotive and wear applications. These materials provide the specific mechanical properties necessary for elevated and ambient temperature applications. Up to now, the major applications served by the MMCs in the automotive industries include selectively reinforced pistons for diesel engines, selectively reinforced cylinder bores in Al engine blocks, intake and exhaust valves, drive-shafts and prop-shafts, brake components (discs, rotors and calipers) and power module components for hybrid and electric cars [5]. Reduction of overall vehicle weight is important for improving fuel economy. Therefore, the application of MMCs for disc brake rotor has been receiving considerable world wide attention. It has been found that, approximately 52% weight saving is possible for a brake rotor if it is substituted by MMC than the cast iron [6]. Moreover, owing to the high thermal conductivity, SiC particles reinforced aluminium composites provides additional advantages for the thermal management of the brake system. Metal matrix composites are finding a wide range of applications in aerospace industries. Aeronautical MMC applications have been established in the aero-structural, aero-propulsion and subsystem categories. Aero-structural components include ventral fins, fuel access door covers and rotor blade sleeves. Moreover, few MMC applications have been established in the space systems [5]. The MMC materials are also used in the industrial, recreational and infrastructure applications. Industrial applications include cemented carbide and cermet materials, electroplated and impregnated diamond tools, Cu and Ag MMCs for electrical contacts, erosion resistance cladding for the petrochemical industry, Cu-infiltrated steel components, and TiC-reinforced Fe and Ni alloys. The TiC-reinforced

Fe and Ni based MMCs are used in the wide range of industrial operations such as cutting, rolling, pelletizing, stamping, piercing, warm metalworking, drawing, forming and punching. Components include hammers, impact dies, canning tools, crimp rollers, check valves, extruder nipples, bending dies, extrusion dies and hot forging die inserts [7]. Moreover, MMC components used in the recreational purpose include golf club shafts and heads, skating shoes, base ball shafts and bicycle frames. Infrastructure applications include Al/B_4C MMCs for nuclear waste containment and continuously reinforced Al/Saffil MMCs for overhead power transmission conductors. MMCs are also in use as microprocessor lids and integrated heat sinks in electronic packaging [5].

1.3 Literature review

Although MMCs have many advantages, problems related to their poor damage tolerance under monotonic or cyclic loads remain [8]. Many applications for MMC materials involve cyclic loading, making the fatigue properties of these materials of critical interest. When a component is subjected to relatively high cyclic loads, high densities of microcracks form simultaneously. From one crack, a larger crack grows that eventually propagates and causes failure. Elucidating the mechanisms of the initiation and growth of this main crack are essential to understanding and predicting the fatigue life of a material. Despite this fact, the exact role of the reinforcement phase in fatigue crack initiation and growth processes as well as their influence in fracture mechanism is not well understood. Although it has been shown that reinforcement can increase the fatigue life of mono-reinforced composite materials, this effect is reportedly dependent on the strengths of the

matrix and the reinforcement/matrix interfaces [9-12]. Based on this fact, the literature review has been carried out as follows.

1.3.1 Fatigue damage and crack initiation in MMC

Fatigue failure of metallic materials is induced by the nucleation of one or several microcracks which propagate slowly during cyclic loading until one of them reaches the critical size and catastrophic failure occurs. In moderate lifetime regime, fatigue life is dominated by the crack initiation stage, while the life is dominated by crack propagation stage at high applied strain amplitude in a very short lifetime regime [13]. The total fatigue life of the material is determined by the combination of the crack initiation life and the crack propagation life. In addition the fatigue limit of smooth specimens is often determined by the ability of nucleating a crack from microstructural inhomogenities and surface defects [14]. Numerous studies have been performed to observe the progressive development of damage during cyclic deformation in MMCs. These studies investigated that damage was initially generated randomly throughout the specimens, and the dominant damage micro-mechanisms detected at this stage were reinforcement fracture [15-18], decohesion at the matrix/reinforcement interface [8, 18], and the formation of the matrix cracks [8]. This situation of homogeneous damage continued until a dominant microcrack was nucleated at the specimen surface, and damage was then rapidly localized around the propagating crack. The broken reinforcements were usually fractured by cracks perpendicular to the loading axis. This failure mechanism is normal to particulate reinforced MMCs tested in tension [19] and this indicated that the ceramic particles were fractured during the tensile part of the fatigue cycle. As in the specimens tested in tension,

the fracture probability increased with reinforcement size. In addition, elongated reinforcements oriented in the loaded direction were more prone to fail than equiaxed ones. All studies reported that particle clusters, where the local volume fraction of reinforcements is very high, were preferential sites for damage nucleation [17, 18]. Ceramic particles broken by cracks parallel to the loading axis were also found in two Al-matrix composites reinforced with alumina particles [15]. Their fracture morphology was similar to that found in MMC tested in compression [20], and is representative of particles broken by splitting during the compressive part of the fatigue cycle. Damage by interface decohesion and matrix cracking was also observed throughout the specimen in other MMC composites. They were mainly concentrated at or near the ends of the elongated reinforcements and whiskers [8, 18] but no influence were found of the reinforcement size in the failure probability. In addition, decohesion was often observed in particle clusters and this was partially attributed to the difficulties to infiltrate the matrix in this regions, which led to poor interfacial bonding. Moreover, few researchers have also explained the progression of damage during cyclic deformation [17, 18, 21]. These simulations demonstrate that the stresses transferred from the matrix to the particles increased during cyclic loading as a result of the cyclic hardening of the matrix. The stresses acting on the reinforcements and on the interface increased progressively during cyclic loading thus increasing the number of damaged particles.

1.3.2 Preferential sites for crack initiation in MMC

The microstructural features which led to the initiation of a fatigue crack were determined from analysis of the fracture surfaces as well as of longitudinal sections under

the scanning electron microscope (SEM). These studies provided different results depending on the stress level during fatigue. A large numbers of microcracks were rapidly initiated at the specimen surface from broken or decohered particles when the fatigue stress amplitude was similar to the composite yield strength [22, 23]. These microcracks grow quickly and coalesce to form a dominant crack, which leads to specimen failure. Thus, the stiff ceramic reinforcements act as preferential sites for crack nucleation, and are ultimately responsible for the poor low cycle fatigue properties of MMCs. Many researchers have observed that in cast composites, cracks were initiated by debonding at the interface in materials reinforced with particles, whiskers and short fibers. Chawla et al. [24] found microcracks 10 μm in length early in the fatigue life at the particle/matrix interface while studying 2080 Al/SiC_p composite. This study also found that the number of cycles necessary to initiate a crack was significantly lower in the composites than in the unreinforced alloy, even if the inclusion size was similar in both materials. Moreover, Levin and Karlsson [25] reported that cracks in a 6061/15 vol% SiC p composite initiated near the particle/matrix interface, in regions of high volume fraction of reinforcement, or by fracturing of individual particles, which were stressed more highly than particles completely within the matrix. This study indicates that fatigue crack initiation and failure may be more likely to take place at defects at the surface of the specimen. Chen and Tokaji [26] observed that the addition of SiC particles in Al alloy matrix makes the crack initiation easier and the fatigue crack initiates at the particle/matrix interface. Bonnen et al. [11] explained the fatigue behaviour of 2xxx series aluminium alloy reinforced with 15 vol% SiC_p. They observed that fatigue cracks occasionally originated at large SiC particles or clusters of SiC particles. The onset of fatigue crack initiation has also been studied in some

whisker-reinforced MMCs. In case of whisker-reinforced composites, debonding was always localized at the end of the whiskers and fibers where the interfacial stresses were greatest [27]. This crack initiation mechanism in composites was attributed to the formation of weak interfaces due to either lack of complete infiltration or to excessive contact between the molten matrix and the ceramic whiskers. Chen et al.[25] have investigated the crack initiation mechanism in SiC whisker-reinforced Al matrix composite. They observed that in the low cycle regime, cracks originated early in fatigue life at the whisker-matrix interface. Williams [27] studied a cast SiCw/2124-T6 A1 composite in which cracks initiated at approximately 70 to 80% of the total lifetime at reinforcement/matrix interfaces. Besides, Ochi et al. [28] found that the crack initiation sites in both aluminium and magnesium alloy based MMCs were large size short fibers and clusters of short fibers.

1.3.3 Fatigue crack growth (FCG) in MMC

The effects of reinforcement characteristics (composition, morphology, size and volume fraction), processing parameters, and matrix heat treatment on fatigue crack growth (FCG) mechanism of MMCs have been extensively reviewed [1, 10, 29, 30]. A large number of systematic experimental studies have been conducted to determine the FCG responses of a variety of aluminium alloys reinforced with either SiC or Al_2O_3 particulates [31-37]. These studies concluded that, in general, composite materials had higher threshold values in the stress intensity factor range, ΔK_{th} as compared to their monolithic materials. The crack growth rate in the near threshold regime was very sensitive to the microstructure. The crack driving force in this regime was very small and crack propagation followed the weakest path in the material as the crack circumvents of the obstacles. Shang and Ritchie

[38] also explained this behaviour that at low applied stress intensity factor range ΔK where particle fracture is less likely, coarser SiC particles improved nominal fatigue thresholds (ΔK_{th}) of MMCs due to enhanced roughness-induced crack closure. Moreover, Chawla et al. [24] have observed that increasing volume fraction and decreasing particle size resulted in an increase in ΔK_{th}. They described the mechanisms responsible for this behaviour in terms of load transfer from the matrix to the high stiffness reinforcement, increasing obstacles for dislocation motion and the decrease in strain localization with decreasing inter-particle spacing as a result of reduced particle size. Besides, the analysis of the micro-mechanisms of crack propagation in the near threshold region in MMC showed that the stress field around the crack tip was not intense enough to fracture the ceramic reinforcements [29, 38, 39] Botstein et al. [40] measured higher crack growth rates in the mid-growth rate (Paris Law) regime compared to the monolithic alloy while doing experiment with Al 2014-40% SiCp and Al 7091-30% SiCp composites. Sugimura and Suresh [33] also explained that large SiC particulate reinforced composite demonstrated lower FCG performance with increased ΔK because of a particle fracture dominated growth mechanism. In addition, several researchers have investigated the effect of particle clustering on FCG in Al-MMC [40, 41]. They determined that particle clustering significantly increased crack growth in the mid-growth rate (Paris Law) regime. Moreover, the effect of load ratio on FCG behavior of MMCs has also been investigated [34, 42]. In general, an increase in load ratio (positive R-ratio) resulted in a decrease in threshold stress intensity. Crack closure was generally considered to be the primary reason for the effect of load ratio on fatigue threshold. It has been widely demonstrated that the FCG response of a SiC particulate reinforced composites strongly depended on the nature of the underlying interaction

between the reinforcing particles and the advancing fatigue crack front. Several studies have explained this interaction in the form of particle matrix interfacial debonding [32, 35], particle fracture [33, 43], crack deflection around the reinforcing particles and subsequently FCG through the matrix [31, 43, 44] and particle crack trapping [45]. Besides, a few researches have pointed out the effect of whisker reinforcement on FCG. The orientation of whisker plays a vital role in advancing fatigue crack. Mason and Ritchie [39] observed higher threshold value in whisker reinforced composites compared to particulate reinforced materials when measured along the rolling direction. They attributed the effect to crack tip shielding by whisker pull-out and roughness induced closure. It has also been reported that when whiskers were aligned in the loading direction, the crack opening displacement reduced. The fatigue cracks were attracted to the whisker ends-which act as stress concentrators- inducing crack deflection [39, 46]. However, when the crack propagated parallel to the whisker, crack growth resistance of whisker-reinforced composites in the near threshold region was highly anisotropic [46].

1.3.4 Deformation and fracture of MMC

Many researchers have investigated the monotonic and cyclic fracture behavior and the fracture mechanisms of ceramic particulates/aluminium based MMCs. Large difference in strain carrying capability of elastically deforming reinforcement and plastically deforming matrix alloy determines the key mechanism of fracture of MMCs [48-55]. Thus, stress is concentrated near the interface edge between reinforcement and matrix or concentrated in the reinforcement, which causes interfacial debonding or reinforcement fracture. This reinforcement fracture or interfacial debonding may decrease the ductility of MMCs [48].

Plastic constraint developed in the matrix has strong effect on cyclic and monotonic deformation of MMCs. Deformation and failure of MMCs by the nucleation and growth of voids and within the ductile matrix were studied by Lorca et al. [54-56]. They demonstrated that due to constrained plastic flow of the matrix between the reinforcement particles in the MMCs, hydrostatic stresses develop in the matrix which plays an important role in the failure mechanism during monotonic and cyclic deformations [15, 54]. This hydrostatic stress enhances the nucleation of the voids in the matrix alloy. Different constraint levels on the matrix flow may control the local failure process (e.g. particle fracture, interfacial debonding and dimple fracture of matrix alloy). In the particulate composites, the plastic strain and voids around the inclusions spread throughout the matrix, whereas, in the whisker reinforced composite they are localized in the vicinity of the reinforcement [54]. The failure mechanism is greatly influenced by different loading conditions (e.g. monotonic and cyclic load). Poza et al. demonstrated the difference of fracture mechanism of a metal matrix composite under monotonic and cyclic loading condition [15]. The tension loaded reinforcements in the matrix are subjected to higher tensile stress than those loaded in fatigue results in high degree of reinforcement fracture. During the loading and unloading process in the cyclic deformation, cyclic hardening occurs due to the accumulation of plastic strain. During the monotonic deformation the plastic strain also develop, especially at the interface between reinforcement and matrix, but significantly lower than in cyclic deformation [15].

1.3.5 Research on hybrid MMC

A few investigations have been made recently [57-62] in which the influence of hybrid reinforcements such as silicon carbide + graphite, Al_2O_3 + silicon carbide and carbon fiber + alumina on the wear and tribological behavior was investigated. Moreover, some studies have focused on the fatigue crack growth behaviour and the fracture mechanism of hybrid MMC. For example, Song et al. [57] have investigated the wear behavior of $Al/Al_2O_3/C$ hybrid metal matrix composites. They observed that the wear resistance was remarkably increased compare with Al/Al_2O_3 composite due to hybrid effect. Other literature shows that wear resistance of hybrid MMCs are higher under dry sliding condition but lower under lubricated sliding condition compared with the non-hybrid MMCs [58]. An analytical analysis considering tensile strength and stiffness enhancement in particle/fiber reinforced aluminium hybrid metal matrix composites was investigated by Jung et al. [59]. They have demonstrated that the strength and stiffness of hybrid composites were much larger than the fiber composite due to the cluster structure which increased the bending rigidity and change the fracture mechanism. Mason and Ritchie [39] have investigated the effects of whiskers and particles on fatigue crack growth in SiC_p and SiC_w hybrid composites. They observed that crack growth resistance in the composites was superior to that in a monolithic alloy at low stress intensity ranges, ΔK, owing to the formation of tortuous crack paths, which in turn enhanced roughness-induced crack closure. Oh and Han [47] pointed out that the increase in ΔK_{th} with increasing particle content in hybrid MMCs reinforced with Al_2O_3 short fibers and Al_2O_3 particles indicated that the crack growth resistance was enhanced over the entire ΔK, and thus hybrid-reinforced composites provided better control of damage tolerance properties over conventional particle-reinforced composites. Moreover,

the fracture mechanisms in cast hybrid MMC under monotonic and cyclic loads were investigated by Rafiquzzaman et al. [63, 64]. They observed that the fracture of hybrid MMC was dominated by the debonding of the particle–matrix and whisker–matrix interfaces followed by void nucleation and coalescence in the Al alloy matrix. This interfacial debonding was due to the cyclic hardening caused by the accumulation of plastic strain at the interface between the matrix and the reinforcement.

The above results concerning microcrack initiation and propagation mechanism as well as damage and failure criteria weigh in favor of either particulate or whisker reinforced MMCs. At present, studies of cast hybrid MMCs are limited in the investigation of fracture mechanism and wear behaviour. Moreover, the studies of the effect of hybridization on fatigue crack initiation and propagation mechanisms are rare. As hybrid MMC materials have the interfaces between the particle/matrix and whisker/matrix, the resulting strength of the interfaces for microcrack initiation and propagation mechanism will undoubtedly play an important role in many structural applications. The crack initiation location and the crack initiation mechanism as well as their stage by stage growth to final failure give critical information for the design or placement of the mechanical component made by MMC materials. Therefore, it is believed by the authors that a through understanding of the low and high cycle fatigue behaviour of cast hybrid reinforcement composites would contribute significantly to the use of these materials in large scale structural applications, e.g., the brake disc of a high speed railway coach. Therefore, it is necessary to understand the initiation and early propagation mechanisms of fatigue microcracks in cast hybrid MMCs during low cycle fatigue as well as the behaviour of the fatigue crack growth during high cycle fatigue owing to evaluate the overall fracture mechanism and the fatigue life. In

the present study, the initiation, interaction, and coalescence of fatigue microcracks in smooth specimens of cast hybrid MMC reinforced with SiC particles and Al_2O_3 whiskers were investigated. In addition, the crack growth behaviour in a notched specimen of hybrid MMC during high cycle fatigue was also investigated. To compare the results of crack initiation and propagation mechanisms in low and high cycle fatigue, another two types of materials were used, cast MMC reinforced with Al_2O_3 whiskers, and unreinforced cast Al alloy. The effect of hybrid reinforcement on the fatigue crack initiation and early propagation mechanisms in low cycle as well as the crack growth behaviour in high cycle fatigue is discussed through the comparison of the observed mechanisms in the three materials.

1.4 Scope and objectives

The aim of this research is to investigate the microcrack initiation and propagation mechanisms in Al based cast hybrid metal matrix composites reinforced with SiC particles and Al_2O_3 whiskers. The specific objectives of the present research are as follows:

- To investigate the role of reinforcement on fatigue crack initiation.
- To investigate the effect of cyclic load on crack initiation and early propagation mechanism of MMC.
- To investigate the hybridization effect on fatigue crack initiation and propagation mechanism.
- To investigate the fatigue crack growth behaviour in the near-threshold region and stable-crack growth regions.

- To evaluate the fracture mechanism of hybrid MMC in low cycle and high cycle fatigue.

1.5. Outline of the thesis

The thesis has been organized into five chapters. The contents of each chapter are summarized below:

Chapter 1 presents an introduction of the research, which describes the background, the motivation, an extensive literature review, the objectives and the scope of this research.

In **Chapter 2**, materials fabrication and its microstructure, the experimental set up and the experimental procedures were thoroughly discussed.

In **Chapter 3**, results and discussion of the experimental results are presented. The results of the initiation of microcracks, their growth and final failure during low cycle fatigue were enumerated in this chapter. In addition, the results of the fatigue crack growth mechanism during high cycle fatigue were discussed.

Chapter 4 presents the results of the numerical analysis conducted in this research. Three dimensional unit cell models were developed using finite element method (FEM) to characterize the crack initiation and propagation mechanism and the interface strength of hybrid MMC.

Chapter 5 presents the general conclusions and directions of the future investigation of this research.

CHAPTER- 2

MATERIALS AND EXPERIMENTAL PROCEDURES

2.1 Introduction

This chapter describes the details of the fabrication method of the materials used in the test. The specimen preparation for the monotonic and fatigue test as well as for the investigation of the microcrack initiation and propagation mechanism in low cycle and high cycle fatigue is explained in this chapter. For minimizing the limitation of MMCs, cast hybrid MMC reinforced with SiC particles and Al_2O_3 whiskers was introduced in this research for structural applications especially in the application of a brake disc of a high speed rail way coach. Other two materials cast MMC with Al_2O_3 whisker and cast Al alloy were also tested. Finally the microcrack initiation and propagation phenomena and fracture mechanism of cast hybrid MMC in low cycle and high cycle fatigue were explained through the comparison of the observed mechanism of other two materials. The MMC materials were fabricated successfully by the squeeze casting method. Monotonic and cyclic fatigue tests were conducted by MTS servopulser machine with a special bending fixture. The fracture surfaces of the specimens were thoroughly examined by the SEM and EDS. The three-dimensional (3-D) analysis was also carried out to examine the roughness of the fractured surfaces by Alicona Mex software.

2.2 Materials Fabrication

Metal Matrix composites generally produced either by liquid metallurgy (Stir casting and liquid metal infiltration) or powder metallurgy techniques [1, 2, 5]. In the liquid metallurgy, the reinforcement particulates are incorporated into a molten metallic matrix,

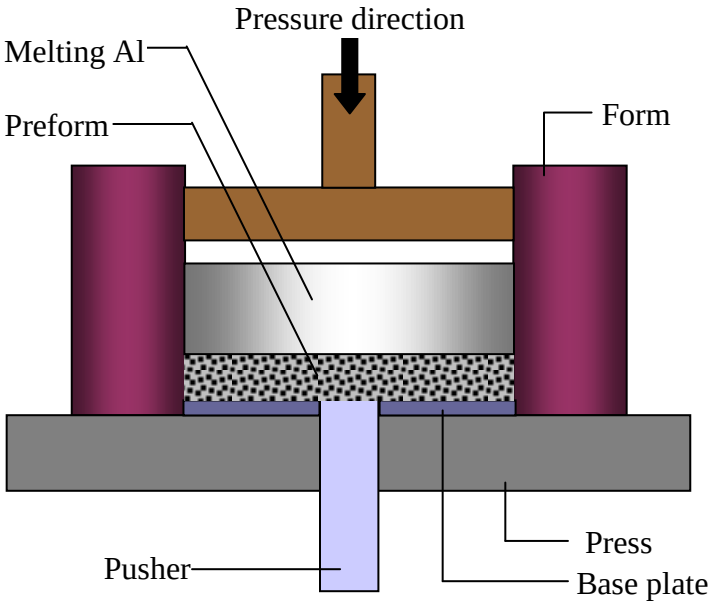

Fig.2.1 Squeeze casting method

followed by mixing and casting of the resulting MMC [65]. For the production of low cost and complex shaped MMCs, squeeze casting technology have now become the most feasible techniques. In the squeeze casting process, liquid metal is injected into the interstices of particles and whiskers usually called as a preform. Preforms are made up of reinforcement particles and whiskers with a known volume fraction of particles and whiskers and it is designed with specific shapes to form an integral part of finished products in the as-cast form [66]. Very high pressure is applied to develop the effective bonding between the liquid metal and the reinforcement particles and whiskers. Since, pressure is applied throughout the process, molten metal flows into the shrinkage cavities and the gasses like hydrogen gets dissolved and remains there in the solution. Thereby, defects like porosity and shrinkage is eliminated [67]. The schematic diagram of squeeze casting method is shown in Fig. 2.1.

In the present study, three types of materials were used: cast aluminum alloy JIS-AC4CH [68], cast MMC with 9 vol% Al_2O_3 whiskers as reinforcement, and cast hybrid MMC. The hybrid MMC was fabricated with 21 vol% SiC particles and 9 vol% Al_2O_3 whiskers as reinforcements and the aluminum alloy JIS-AC4CH as matrix. The three types of materials were fabricated using the squeeze casting process with a 100 MPa maximum pressure, using a hybrid preform made of SiC particles and Al_2O_3 whiskers for the hybrid MMC and a preform of Al_2O_3 whiskers for MMC with Al_2O_3. The squeeze casting pressure of 100 MPa was applied to overcome the resistance against flow and to press the melt into all the open pores of the hybrid preform. The materials were heat treated using the T7 process. The chemical composition of AC4CH alloy is listed in Table 2.1.

Table 2.1 Chemical composition of AC4CH alloy, (wt%)

Si	Fe	Mg	Ti	Al
7.99	0.2 (max.)	0.57	0.07	Bal.

2.3 Specimen Preparation

To investigate the hybrid effect in the microcrack initiation mechanism and stage by stage growth till to final failure in low cycle fatigue, rectangular bar smooth specimens were prepared for all three materials. The specimen dimensions were as follows: length of 100 mm, thickness of 6 mm and width of 8 mm. The shape and dimension of the specimen are shown in Fig 2.2. Moreover, for the crack propagation test in the high cycle fatigue, rectangular bar single edge notched specimens were prepared as shown in Fig 2.3. The specimen dimensions for the high cycle fatigue were as follows: length of 100 mm,

thickness of 8 mm width of 6 mm and a notch width of 0.5 mm. All the specimens were cut out from a disc. The machined surfaces of the specimens were polished using a polishing machine with 15, 3, and 1 µm diamond particles sequentially until all scratches and surface machining marks were removed. Due to the formation process of the preform the whiskers in the both MMCs are randomly oriented in a plane. In this study, 'Longitudinal cross section' is defined as the plane and 'lateral cross section' is defined as the one perpendicular to the plane.

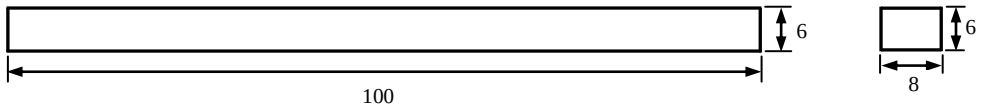

Fig. 2.2 Shape and dimension of the rectangular bar smooth specimen prepared for microcrack initiation test in low cycle fatigue.

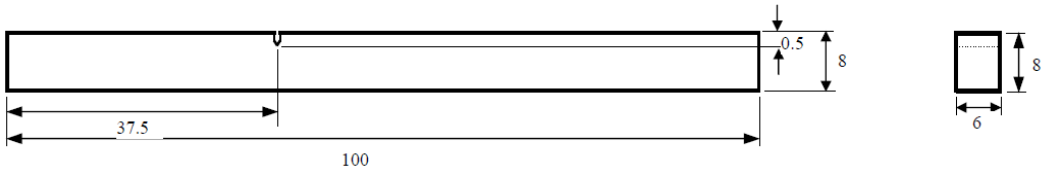

(a)

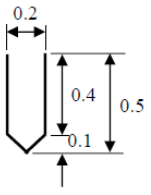

(b)

Fig. 2.3 (a) Shape and dimension of a single edge notched specimen prepared for crack propagation test in high cycle fatigue (b) dimension of the notch.

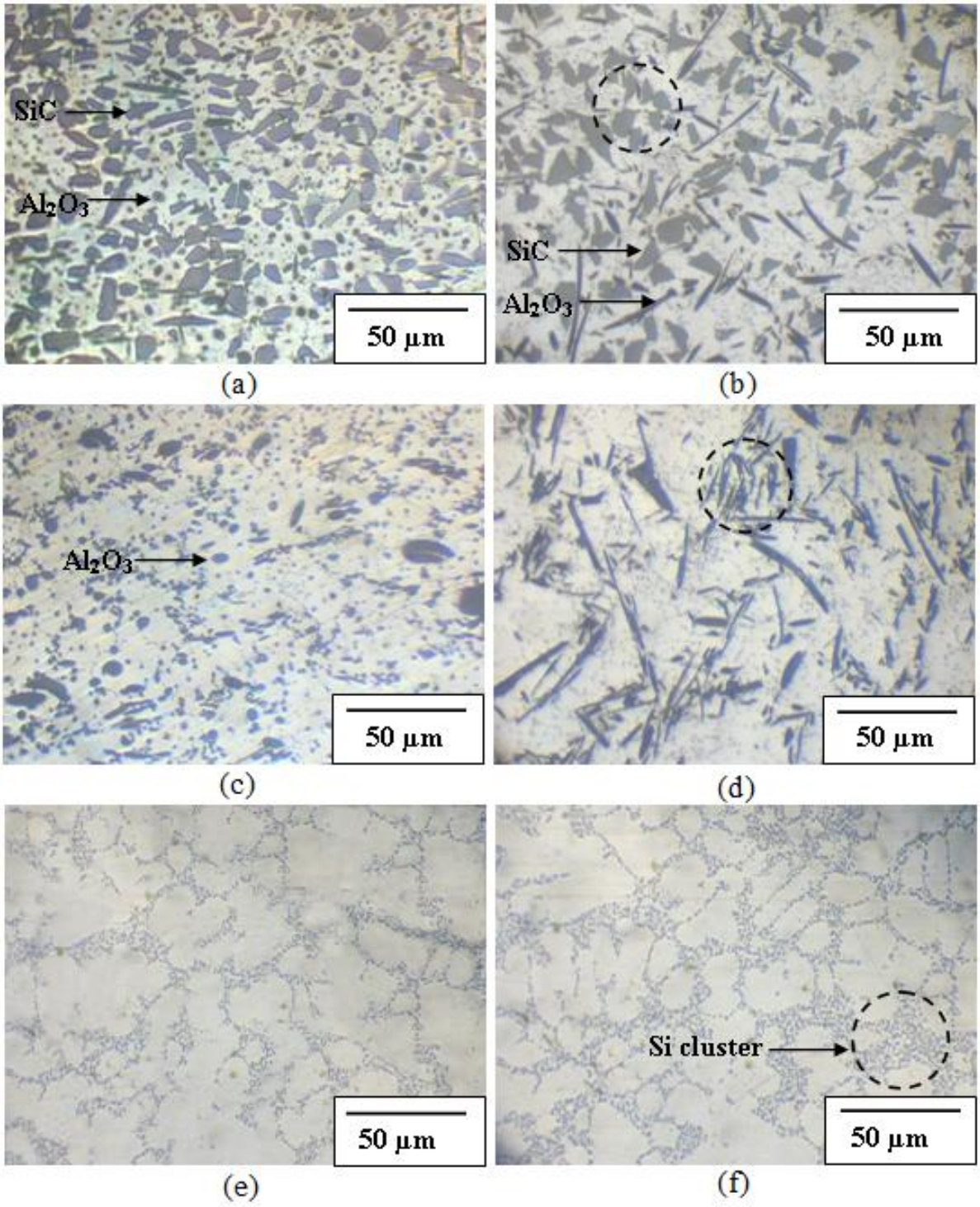

Fig. 2.4. Microstructure in lateral and longitudinal direction (a and b) Hybrid MMC, (c and d) MMC with Al_2O_3 whiskers and (e and f) Al alloy.

2.4 Microstructural features

The microstructures of the three materials in the lateral and the longitudinal cross sections are shown in Fig. 2.4. Most of the SiC particles in the hybrid MMC were rectangular with sharp corners (Fig. 2.4a, b), and most of the Al_2O_3 whiskers in both MMC materials were roller-shaped (Fig. 2.4 a,b and c,d). The SiC particles had an average length of 23 μm. The average diameter of the Al_2O_3 whiskers was 2 μm in both MMCs. The average length of the Al_2O_3 whiskers in hybrid MMC was 35 μm and in MMC with Al_2O_3 whiskers 38 μm. The Al_2O_3 whiskers were randomly oriented in the same plane as the longitudinal direction of the specimen. In the Al alloy, the average grain size was found to be 48 μm. The Si particles in the Al alloy were round with an average diameter of 3 μm. At frequent intervals, clusters of SiC particles and Al_2O_3 whiskers were observed in both of the MMC materials, as indicated by the broken lines in Fig. 2.4 b and d, respectively. Clustering of Si was also observed in the Al alloy, as shown by the broken line in Fig. 2.4f. The mechanical properties of reinforcement and tested materials are shown in Table 2.2. The listed properties for both MMCs are along the longitudinal direction.

Table 2.2. Mechanical properties of reinforcement and tested materials

Parameters	Al_2O_3	SiC	Al alloy AC4CH	Hybrid MMC	MMC with Al_2O_3
Young's modulus (GPa)	380	450	70.0	142	104
Poisson's ratio	0.27	0.20	0.33	0.28	0.29
Yield strength (MPa)	-	-	131	166	141
Tensile strength (MPa)	-	-	262	228	200
Tensile elongation (%)			9.22	2.77	5.44

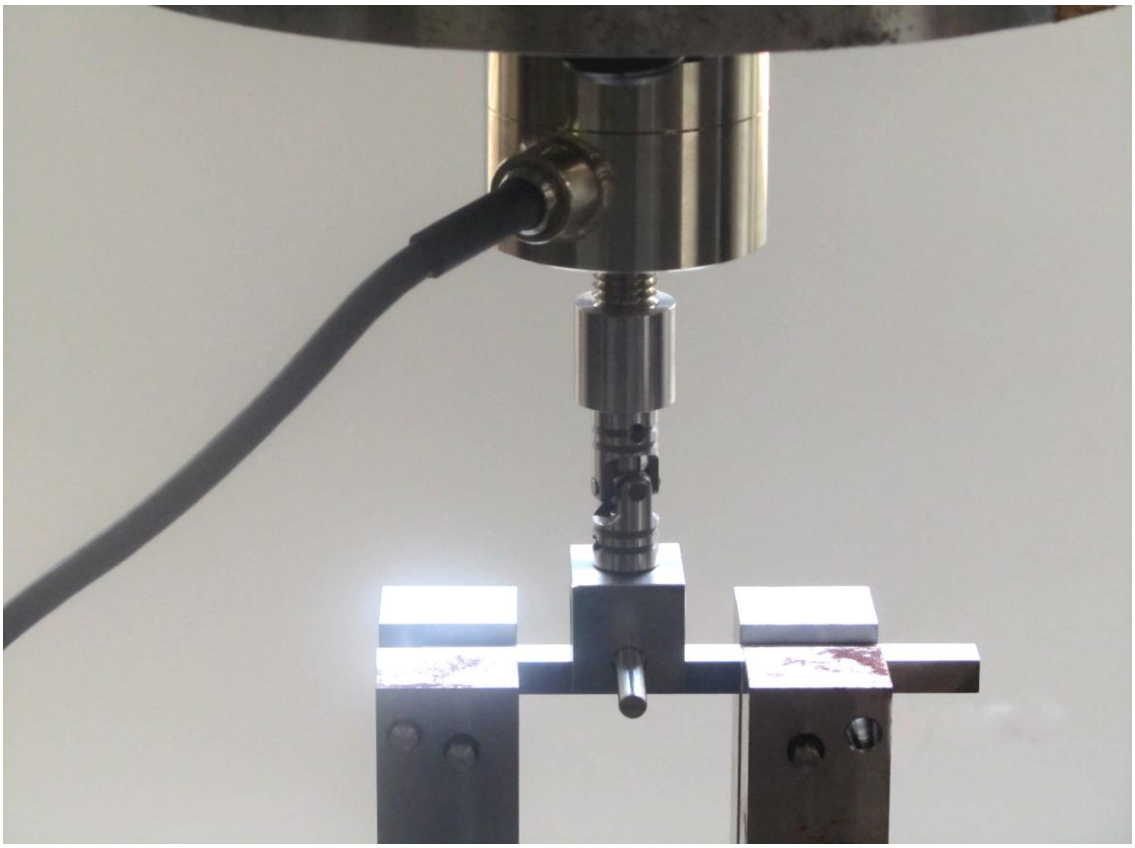

Fig. 2.5 Experimental setup

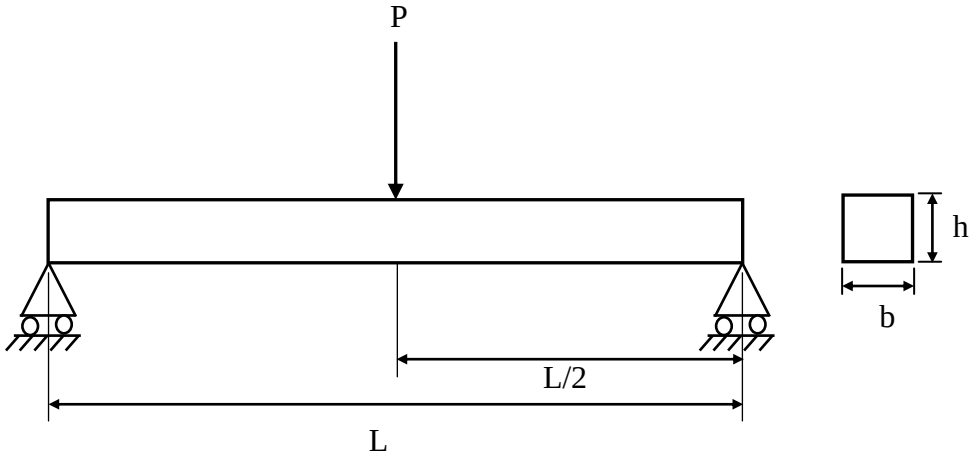

Fig. 2.6 Schematic illustration of three point bending test in smooth specimen

2.5 Experimental set up and Procedure

2.5.1 Microcrack initiation test in low cycle fatigue

For microcrack initiation study in low cycle fatigue, conventional three point bending tests were carried out on a rectangular bar smooth specimens to reduce the observation area in the maximum stress location. The three point bending tests were performed using special bending fixtures equipped with a 5 kN load cell in a Shimazu ServoPulser. The span distance was 60 mm. Load and deflection data were recorded by a computer data acquisition system. The experimental set up is shown in Fig. 2.5. First the monotonic bending tests were conducted at a displacement rate of 0.0025 mm·s-1. The strength of the three different materials was calculated from the maximum load at failure as a nominal bend stress σ_c. Schematic illustration of three point bending test in smooth specimen is shown in Fig 2.6. The nominal bending stress was calculated from the following equation,

$$\sigma = \frac{3PL}{bh^2} \qquad (2.1)$$

Where, P is the applied load. The specimen dimension L, b and h are defined in figure 2.6. Thereafter, cyclic fatigue tests were conducted in the load control mode under the load ratio R = 0.1 at the frequency of 0.5 Hz. Three tests for each material were conducted with the maximum stress of 0.7 σ_c, 0.8 σ_c, and 0.9 σ_c. All tests were carried out at room temperature. The number of cycles to failure was taken as the fatigue life (N_f). For one stress amplitude, one specimen was used; therefore error bars in the number of cycles were not employed. The plastic replica technique was used to study the initiation and early propagation of microcracks at various times during the fatigue life. During replication, the specimen was held at mean load to ensure that any cracks that might be present would be fully opened.

Replicas were taken using Bioden replicating films softened in acetone. Finally, the replicas were examined using an optical microscope. The tensile surface of the broken specimens was also examined with an optical microscope to determine the crack initiation location. Fracture surfaces were comprehensively examined in a scanning electron microscopy (SEM) to determine the microcrack initiation mechanism and microscopic fracture mode as well as microscopic mechanism governing fracture. Energy-dispersive x-ray spectroscopy (EDS) analysis was used to identify the constituents on the fracture surfaces. Special effort was made to take the matching photographs from the two halves of the broken specimens to assess the relative incidence of particle/whisker cracking and particle/matrix or whisker/matrix interfacial debonding. Prior to testing, no cracks were seen but the shape of large Al_2O_3 whiskers could be identified in the microscopy images. In this study, "crack initiation" is defined as the point at which a black line of several micrometers is first observed in the magnified replica image, during the cyclic loading test.

2.5.2 Crack propagation test in high cycle fatigue:

Experiments of the fatigue crack growth in high cycle fatigue were carried out on rectangular bar single edge notched specimen. A conventional three point bending tests were performed using special bending fixtures equipped with a 5 kN load cell in a Shimazu ServoPulser as similar to the microcrack initiation test previously described. A schematic illustration of the three point bending test in a single edge notched specimen is shown in Fig. 2.7. The span distance was 60 mm. Load and deflection data were recorded by a computer data acquisition system. Tests were conducted under ΔK control mode with a constant stress ratio $R = 0.1$ in sinusoidal loading in accordance with the guidelines in

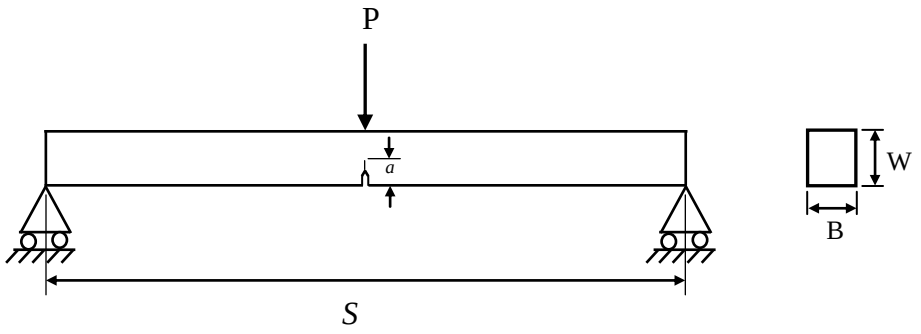

Fig. 2.7 Schematic illustration of three point bending test in a single edge notched specimen.

ASTM E647. The instantaneous stress intensity during the experiment was measured by using the following equation:

$$K_1 = \frac{P}{B\sqrt{W}} f(a/W) \quad \text{.....(2.2)}$$

Where, P is the applied load, a is the crack length and $f(a/W)$ is a dimensionless geometry function. The specimen dimensions B and W are defined in Fig. 2.7. The geometry function was calculated by using the following equation:

$$f(a/W) = \frac{3\frac{S}{W}\sqrt{\frac{a}{W}}}{2\left(1+2\frac{a}{W}\right)\left(1-\frac{a}{W}\right)^{3/2}}\left[1.99-\frac{a}{W}\left(1-\frac{a}{W}\right)\left\{2.15-3.93\left(\frac{a}{W}\right)+2.7\left(\frac{a}{W}\right)^2\right\}\right] \text{.(2.3)}$$

Where, S is the span distance. A decreasing ΔK procedure was used to determine the threshold stress intensity. The stress intensity corresponding to a crack growth rate of 10^{-11} m/cycle was taken as the threshold stress intensity, ΔK_{th}. Once the threshold stress intensity was determined, the crack growth was continued by increasing ΔK. Crack growth was

measured using a Bioden replicating films softened in acetone. The replicas were examined using an optical microscope. The tensile and fracture surfaces were comprehensively examined using scanning electron microscopy (SEM) and energy-dispersive x-ray spectroscopy (EDS) to characterize the near threshold region and stable or mid-growth rate region. Moreover, the three-dimensional (3-D) analysis was carried out to examine the roughness of the fracture surface using the Alicona Mex software [69]. Additionally, the areas of dimples, interfacial debonding of particle/matrix and whisker/matrix, particle and whisker fracture were also examined. To determine the area fraction of the particle/whisker fracture and interfacial debonding in the near threshold region and stable crack growth region, a particular area of 300 x 300 μm^2 is selected in both the regions. Therefore, the fraction of the particle and whisker fracture area is defined as the total particle and whisker fracture area divided by the total area measured. The area fraction of particle/matrix and whisker/matrix debonding in both the regions as well as the area fraction of striation formed in the stable crack growth region are also measured by the same procedure.

CHAPTER-3

EXPERIMENTAL RESULTS

3.1 Introduction

This chapter describes the experimental results of this research. The specimens are monotonically and cyclically deformed to failure at room temperature under conventional three-point bending test. The initiation of the microcracks and their stage-by-stage propagation till to final failure during low cycle fatigue and crack growth behaviour during high cycle fatigue are described by using the plastic replica observation. Moreover, SEM observations of the fracture surfaces are made to describe the fracture mechanism of the materials and EDS mapping analysis is used to identify the constituents on the fracture surfaces. The measured areas of dimples, interfacial debonding and particle/whisker fractures on the fracture surfaces are also examined. In addition, the roughness of the fracture surfaces is examined by the three-dimensional (3-D) analysis and the results are presented in this chapter. The mechanism of fatigue crack initiation and propagation during low and high cycle fatigue is thoroughly discussed in this chapter.

3.2 Monotonic test

In order to obtain the strength of the materials, monotonic bending tests were conducted. The strength of the three different materials was calculated from the maximum load at failure as a nominal bend stress σ_c. The nominal bending stress and deflection curves measured by the three point bending test under monotonic loading are presented in

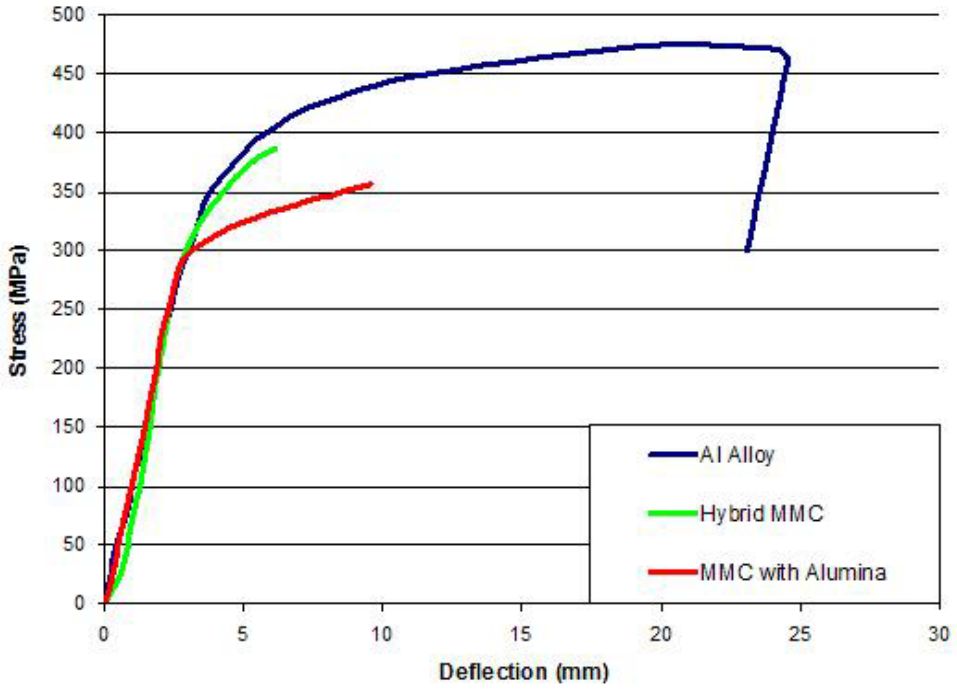

Fig. 3.1 Nominal bending stress versus deflection curves under monotonic loading.

Table 3.1 Fracture stress σ_c of three materials under bending

Materials	Fracture stress σ_c (MPa)
Hybrid MMC	386
MMC with Al_2O_3	357
Al alloy	475

Fig.3.1. The specimens composed of hybrid MMC and MMC with Al_2O_3 whiskers fractured at 386 and 357 MPa, respectively; the Al alloy, rather than fracturing, plastically collapsed at 475 MPa. The fatigue test was conducted based on the fracture stress of these three materials. The collapse stress of the Al alloy was used as the fracture stress during fatigue testing. The fracture stress σ_c of the three materials is listed in Table 3.1.

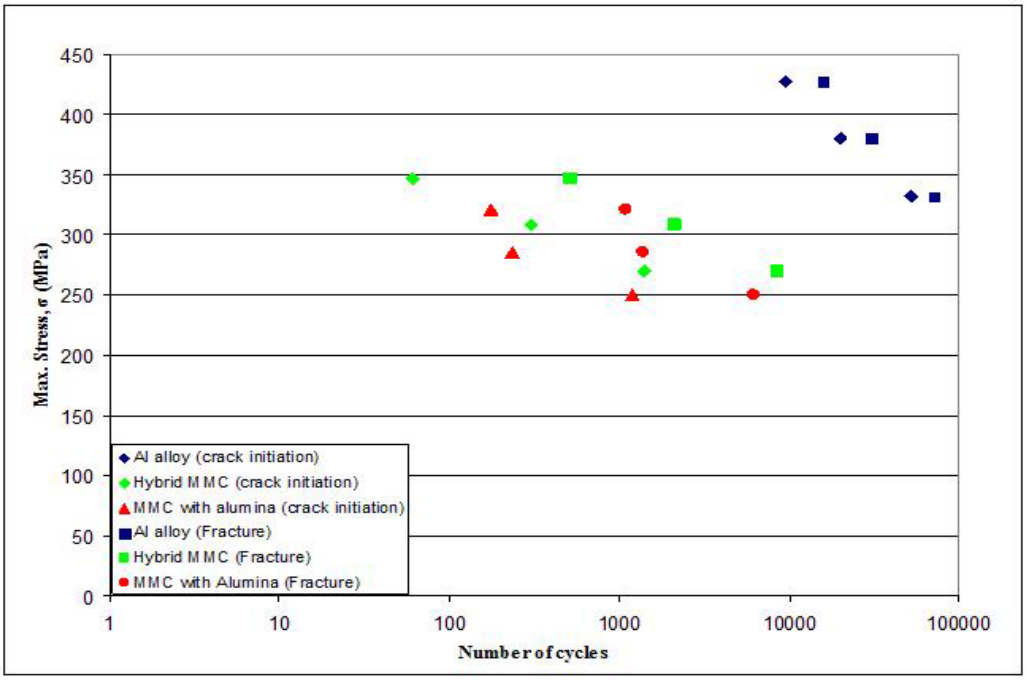

Fig. 3.2 Number of cycles to crack initiation and final failure at different stress levels.

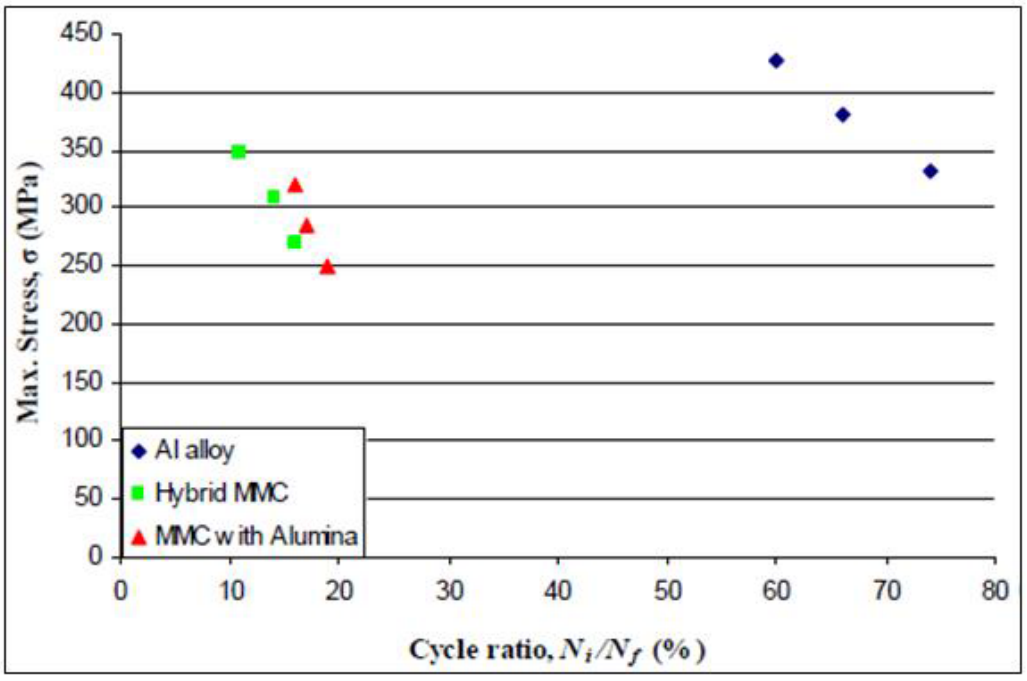

Fig. 3.3 Initiation of microcracks at different stresses and cycle ratios.

3.3 Low cycle fatigue test

In order to obtain the crack initiation and propagation mechanism as well as the fatigue life, fatigue tests were conducted in the load control mode. Fig. 3.2 shows the number of cycles needed to initiate microcracks, N_i, and final failure, N_f, at different stress levels of the specimens composed of hybrid MMC, MMC with Al_2O_3 whiskers, and unreinforced Al alloy. Moreover, Fig. 3.3 displays the microcrack initiation at different cycle ratios, N_i/N_f, of these materials. The crack initiation life and the total fatigue life of the hybrid MMC were found to be superior to those of the MMC with Al_2O_3 whiskers in low cycle fatigue, as shown in Fig. 3.2. In the hybrid MMC, microcracks were initiated very early in the fatigue life. For example, at the 0.7 σ_c stress level, microcracks were initiated only at 1400 cycles (Fig. 3.2), which is 16% (Fig. 3.3) of the fatigue life. At the same stress level, microcracks were initiated at 1200 cycles (Fig. 3.2), which is 19% (Fig. 3.3) of the fatigue life of the MMC with Al_2O_3 whiskers, and at 52,000 cycles (Fig. 3.2), which is 74% (Fig. 3.3) of the fatigue life of the unreinforced Al alloy. Similar phenomena of micro-crack initiation were also observed under 0.8 σ_c and 0.9 σ_c. This clearly demonstrates that the propagation life in the cycle ratio for the hybrid MMC was large compared to that of the other two materials.

3.4 Microcrack initiation and propagation in low cycle fatigue

3.4.1 Hybrid MMC

The evolution of fatigue microcracks on the surface of the materials can be observed from optical micrographs of the same areas on replicas. The optical micrographs of replicas obtained at various stages of fatigue testing of the hybrid MMC specimen at 0.7 σ_c = 270

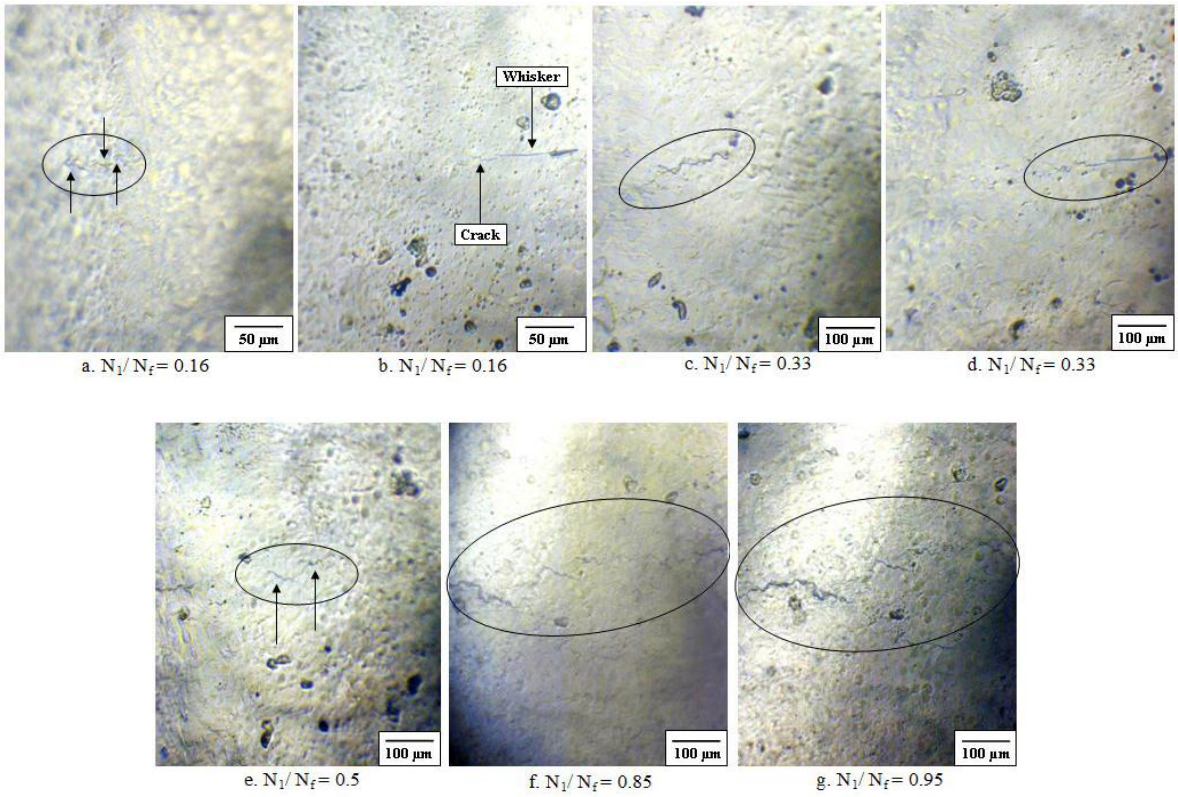

Fig. 3.4 Crack initiation and propagation at various stages of fatigue life of hybrid MMC: σ_c = 270 MPa, N_f = 8580 cycles

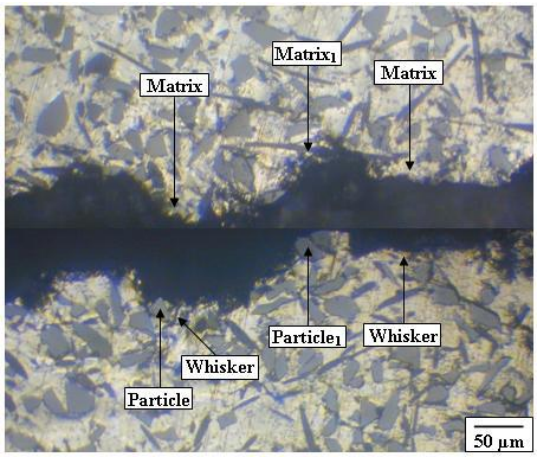

Fig. 3.5 Optical micrograph of crack initiation site at the matching tensile surface of the fractured specimen: hybrid MMC, 0.7 σ_c = 270 MPa

MPa peak stress are shown in Fig. 3.4. At 16% of the fatigue life (Fig. 3.3), several cracks were initiated (indicated by arrows in Fig. 3.4a). Another crack was initiated simultaneously in a region next to the edge of an Al_2O_3 whisker (arrow labeled "Crack" in Fig. 3.4b). These cracks had an initial size of 15-20 μm. The cracks shown in Fig. 3.4a then coalesced, and at 33% of the fatigue life, the length of the crack extended to 190 μm (Fig. 3.4c). At the same time, the crack near the edge of the whisker grew to 175 μm (Fig. 3.4d). In both cases, secondary microcracks were formed ahead of the crack tip, and their length increased cycle by cycle until they joined with the main crack, thus increasing the length of the main crack. At 50% of the fatigue life, a few cracks 25-50 μm in length formed in between the two main cracks (arrows in Fig. 3.4e). At 85% of the Fatigue life, all of these cracks coalesced (Fig. 3.4f), and at 95% of the fatigue life, a fatal crack was produced (Fig. 3.4g). The size of the fatal crack was around 650 μm on the specimen surface. The final failure took place at 8580 cycles. Similar microcrack initiation and coalescence phenomena were observed under the other maximum stress values tested. Fig. 3.5 shows the optical micrograph of the crack initiation site at the matching tensile surface of the fractured specimen. It is apparent that the microcracks initiated at the particle/matrix interface (as indicated by the "Matrix" and the "Particle" arrows on the left in Fig. 3.5, which correspond to the microcracks in Fig. 3.4a and 3.4c). The crack initiated SiC particle was located at the boundary of a cluster of SiC particles where the interface was facing the outside of the cluster. An Al_2O_3 whisker was also found located very close to the crack initiated SiC particle (as indicated by the "Whisker" arrow on the left side of Fig. 3.5). The microcracks coalesced with fracture in the Al alloy. The microcracks initiated at the

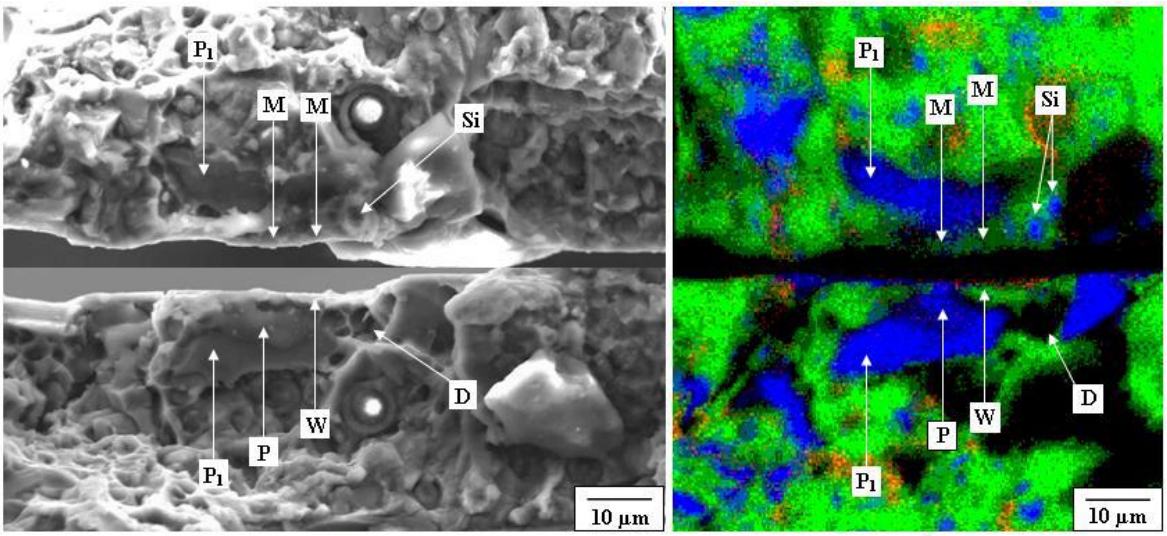

Fig. 3.6 Matching fracture surface of microcrack initiation site at the cluster of SiC particles (a) SEM micrograph (b) EDS mapping analysis: hybrid MMC, 0.7 σ_c = 270 MPa

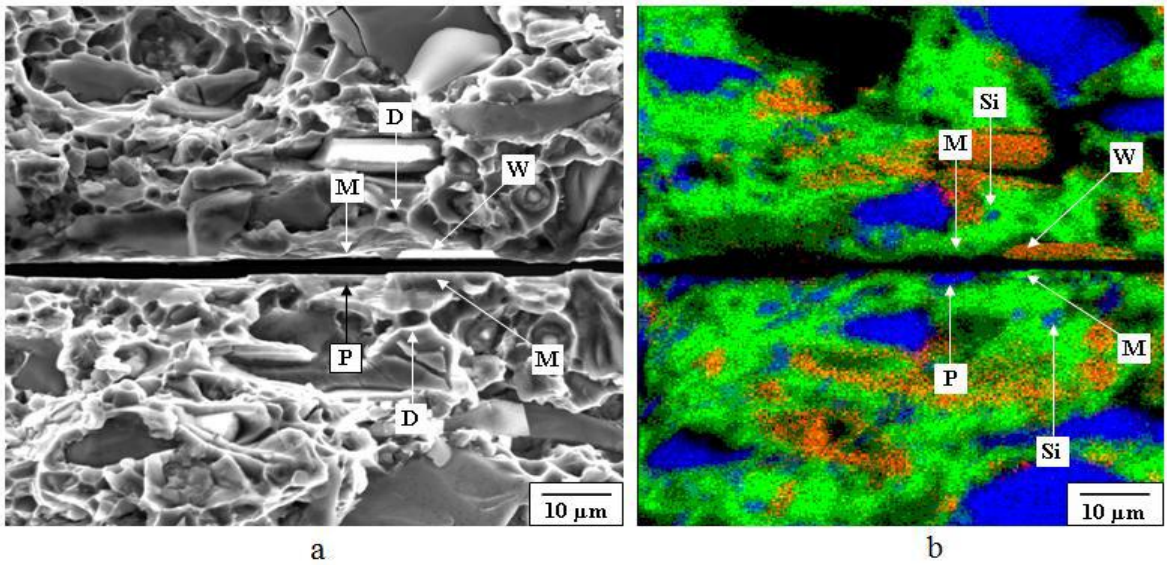

Fig. 3.7 Matching fracture surface of microcrack initiation site next to the edge of Al_2O_3 whisker (a) SEM micrograph (b) EDS mapping analysis: hybrid MMC, 0.7 σ_c = 270 MPa

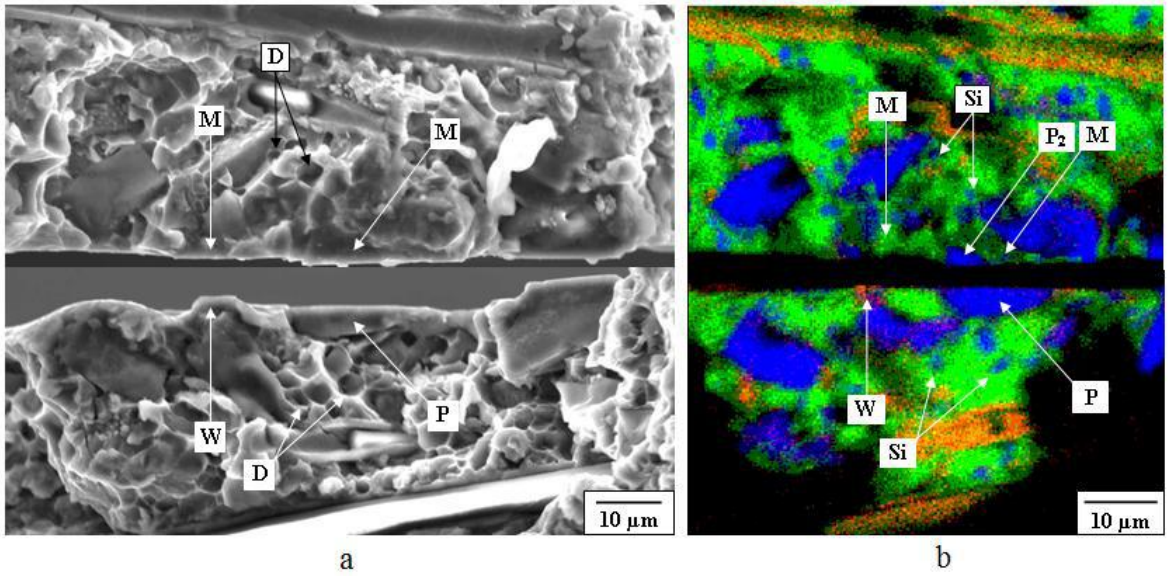

Fig. 3.8 Matching fracture surface of secondary microcrack initiation and coalescence site (a) SEM micrograph (b) EDS mapping analysis: hybrid MMC, 0.7 σ_c = 270 MPa

whisker/matrix interface (as indicated by the "Whisker" and "Matrix" arrows on the right in Fig.3.5, which correspond to the microcracks in Fig. 3.4b and 3.4d), and the secondary microcracks in between these two main cracks on the particle/matrix interface (as indicated by the "$Particle_1$" and "$Matrix_1$" arrows in Fig. 3.5, which correspond to the microcracks in Fig. 3.4e) are also shown. Figure 3.6 shows the SEM image of the matching fracture surface of the microcrack initiation site at the cluster of SiC particles in the hybrid MMC. In Fig. 3.6a, the dark flat area indicated by *P* corresponds to the location indicated by the "Particle" arrow in Fig. 3.5, and the area *M* on the left side corresponds to the location indicated by the "Matrix" arrow on the left in Fig. 3.5. Fig. 3.6b shows the EDS mapping analysis results on the areas corresponding to Fig. 3.6a. The green, blue, and red colors in Fig. 3.6b indicate the presence of Al, Si, and O, respectively, on the fracture surfaces. In

Fig. 3.6b, the blue area indicated by *P* contains a significant amount of Si (96%) and a small amount of Al (4%), identifying the area as a SiC particle (corresponding to *P* in Fig. 3.6a). The green area indicated by *M* on the left contains a large amount of Al (93%) and a small amount of Si (7%), indicating that this area is Al matrix (corresponding to *M* on the left in Fig. 3.6a). Therefore, the blue and green area indicated by the *P-M* pair in the matching halves denote the crack initiation site (Fig. 3.4a) where SiC particle/matrix interfacial debonding occurred. The blue P_1-P_1 pair in Fig. 3.6b indicates the presence of SiC particles on both sides of the fractured surface, meaning that interface debonding was followed by transgranular fracture in this crack initiation site (corresponding to the P_1-P_1 pair in Fig. 3.6a). The coexistence of green and red, indicating the presence of both Al and O, identifies this area as an Al_2O_3 whisker, denoted by *W* in Fig. 3.6b (corresponding to *W* in Fig. 3.6a). This Al_2O_3 whisker was located very close to the debonded SiC particle. Interfacial debonding was also found in this Al_2O_3 whisker, as indicated by the *W-M* pair on the right in Fig. 3.6a. Between the *P-M* pair and the neighboring SiC particle on the specimen surface in Fig. 3.6a, a number of dimples were nucleated (indicated by the *D* arrows in Fig. 3.6a) in the aluminum alloy matrix. EDS mapping analysis confirmed the presence of a few Si particles on the opposite side of the dimples (as indicated by the *Si* arrow in Fig. 3.6b). Dimple formation indicated the occurrence of void nucleation, which was induced by plastic deformation of the Al matrix at the second phase Si particles. The edges of the dimples were not as clear as those in the unstable fracture region are, likely due to the mutual contact effect due to cyclic loading. In addition, the SEM micrograph of another crack initiation site where the microcrack was initiated at the edge of an Al_2O_3 whisker is shown in Fig. 3.7. In Fig. 3.7a, the areas indicated by *W* and *M* correspond to the

locations indicated by the “Whisker” and “Matrix” arrows, respectively, on the right in Fig. 3.5. Results from the EDS mapping analysis on the corresponding areas are shown in Fig. 3.7b. The combined green and red area at the edge of the fracture surface in Fig. 3.7b contained a large amount of Al (86%) and a small amount of O (14%), indicating the presence of an Al_2O_3 whisker (corresponding to *W* in Fig. 3.7a). The green area indicated by *M* on the opposite side of the fracture surface indicates the Al matrix (Fig. 3.7b). Therefore, the *W-M* pair in Fig. 3.7b (corresponding to the *W-M* pair in Fig. 3.7a) denoted the Al_2O_3 whisker next to the crack initiation site (Fig. 3.4b) where Al_2O_3 whisker/matrix interfacial debonding occurred. The blue area indicated by *P* in Fig. 3.7b locates the SiC particle found in the crack initiation site very close to the Al_2O_3 whisker (corresponding to *P* in Fig. 3.7a). This SiC particle was also found to be debonded from the matrix (indicated by the blue and green area/*P-M* pair in Fig. 3.7b, which corresponds to the *P-M* pair in Fig. 3.7a). Many dimples were observed around the debonded *P-M* and *W-M* pairs, indicating void formation in this crack initiation site as denoted by *D* in Fig. 3.7a. In addition, EDS analysis revealed the presence of Si particles in the dimples, as indicated by the “*Si*” arrow in Fig. 3.7b. Similar observations were made for the fracture surface of the secondary microcrack initiation and coalescence site shown in Fig. 3.8. The blue and green area indicated by the *P-M* pair in Fig. 3.8b represents the particle-matrix interfacial debonding at the edge of the fracture surface (corresponding to the *P-M* pair in Fig. 3.8a). However, a segment of the debonded SiC particle was observed on the opposite side of the fracture surface (blue area indicated by *'P_2'* in Fig. 3.8b) means a portion of this particle was fractured but the rest of the part being debonded. This implies that the interface debonding was followed by the transgranular fracture in this crack initiation site. Moreover, an Al_2O_3

whisker (combined green and red area pointed out by *'W'* in Fig. 3.8b) was found exist close to this SiC particle (corresponding to *'W'* in Fig. 3.8a). The whisker/matrix interfacial debonding was also observed in this Al_2O_3 whisker along the crack propagation path. Plenty of dimples (indicated by arrows *'D'* in Fig. 3.8a) were observed nucleated between the *P-M* pair and the neighbor *W-M* pair along the specimen surface in aluminium alloy matrix. The existence of Si particles (pointed out by arrow *'Si'* in Fig. 3.8b) on the opposite side of the dimples is confirmed by the EDS mapping analysis implies that the void nucleation is induced by the plastic deformation concentration in Al matrix at the second phase Si particles. However, in these cases also the matching morphologies of dimples around the *P-M* pair show unclear edges compared to the one in the relatively deep area.

From the above observations, the hybrid effect on microcrack initiation and early propagation behaviors in MMCs is clearly perceived. Microcracks were initiated in two places at the same time (Fig. 3.4a and 3.4b). In the first case, an Al_2O_3 whisker was located very near to the crack initiated SiC particle (marked by '*W'* in Fig. 3.6a and 3.6b). Similarly, in the second case, another SiC particle was found very close to the edge of the whisker that was located next to the crack initiation site (indicated by '*P'* in Fig. 3.7a and 3.7b). In addition, an Al_2O_3 whisker was located near the crack initiated SiC particle in the crack propagation path at the secondary microcrack initiation and coalescence site (indicated by '*W'* in Fig. 3.8a and 3.8b). Hence, it appears that locations where SiC particles and Al_2O_3 whiskers coincide are extremely vulnerable to crack initiation, meaning that the effect of hybridization reduces the resistance to crack initiation. The fracture mechanism of hybrid MMCs during cyclic loading was also elucidated from the results presented in Fig. 3.6-3.8. Between the *P-M* pair and the neighboring *W-M* pair in both

microcrack initiation sites as well as the secondary microcrack initiation and coalescence sites along the specimen surface, many nucleated dimples were observed (indicated by '*D'* arrows in Fig. 3.6-3.8) in the aluminum alloy matrix. EDS mapping analysis confirmed the presence of Si particles on the opposite side of the dimples (indicated by '*Si'* arrows in Fig. 3.6b, 3.7b, and 3.8b). The dimples on both sides of the fracture surface clearly indicated void nucleation, which was induced by plastic deformation at the Si particles. However, the edge of the dimples was not as clear as those of dimples far from the initiation and coalescence site were, and this is probably due to the mutual contact effect due to cyclic loading. Debonding at the particle/matrix and whisker/matrix interfaces was observed at the edge of the fracture surfaces in the crack initiation location (Fig. 3.6 and 3.7) as well as the crack coalescence location (Fig. 3.8). SiC particle fracture was also observed in both locations, which were surrounded by nucleated dimples indicating interfacial debonding as well as transgranular fracture in SiC particles followed by void nucleation in the Al alloy matrix, dominating the fatigue fracture of the hybrid MMC.

3.4.2 MMC with Al_2O_3 whisker

Fig. 3.9 shows the optical micrographs of replicas obtained at various stages of fatigue testing of the specimen composed of MMC with Al_2O_3 whiskers at 0.7 σ_c = 250 MPa peak stress. At 19% of fatigue life (Fig. 3.3), several cracks 20-25 μm in length were initiated in a region near the edge of two whiskers (indicated by "Crack" arrows in Fig. 3.9a and 3.9b). The delamination between the Al_2O_3 whisker and Al alloy could not be identified by observation of the replica at this stage. These cracks grew on their own in the Al alloy matrix, and at 33% of the fatigue life, they grew to 220 μm and 130 μm (arrows in Fig.

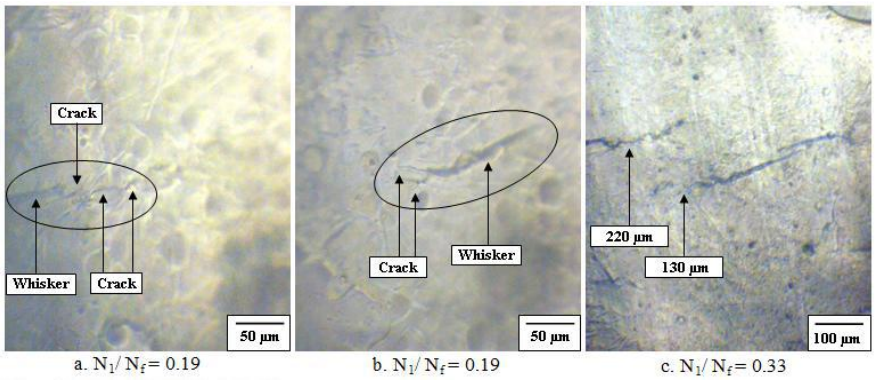

a. $N_1/N_f = 0.19$ b. $N_1/N_f = 0.19$ c. $N_1/N_f = 0.33$

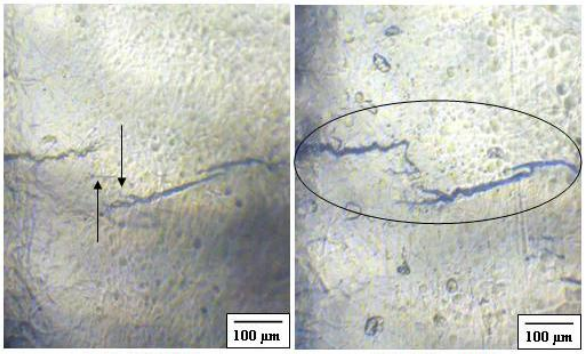

d. $N_1/N_f = 0.5$ e. $N_1/N_f = 0.95$

Fig. 3.9 Crack initiation and propagation at various stages of fatigue life of MMC with Al_2O_3 whisker: σ_c = 250 MPa, N_f = 6200 cycles.

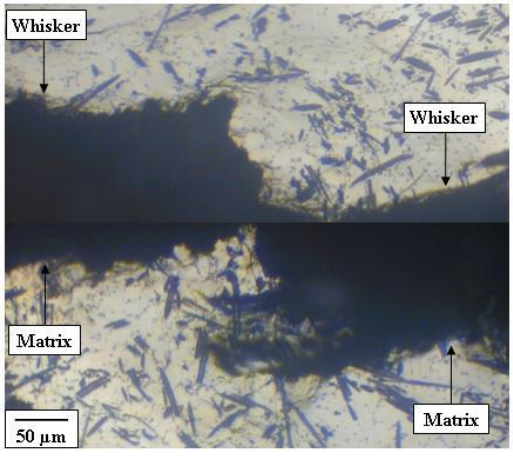

Fig. 3.10 Optical micrograph of crack initiation site at the matching tensile surface of fractured specimen: MMC with Al_2O_3 whisker, 0.7 σ_c = 250 MPa.

3.9c). In addition, at 50% of the fatigue life, a few cracks less than 25 μm long were found in a region next to the edge of a whisker in between these two main cracks (arrows in Fig. 3.9d). At 95% of the fatigue life, all these cracks coalesced, as shown in Fig. 3.9e. The thicknesses of both whiskers where the microcracks initiated were increased, meaning that the whiskers along the line of the cracks were debonded (Fig. 3.9e). The fatal crack was produced by joining the two cracks originating at the debonded whiskers and was around 825 μm in length. The final failure took place at 6200 cycles. The phenomena of microcrack initiation and coalescence were found to be quite similar in subsequent tests performed under greater stress conditions. Figure 3.10 shows the optical micrograph of the crack initiation site at the matching tensile surface of the fractured specimen. It is apparent that the microcracks were initiated at the edge of two whisker/matrix interfaces (indicated by the "Whisker" and "Matrix" arrows on the left in Fig. 3.10, which correspond to Fig. 3.9a and the "Whisker" and "Matrix" arrows on the right in Fig. 3.10, which also correspond to Fig. 3.9b). No large-scale plastic deformation in the Al grain was observed. Figure 3.11 shows the SEM micrograph of the matching fracture surface at the microcrack initiation site. In Fig. 3.11a, the bright white area labeled *W* corresponds to the location indicated by the "Whisker" arrow on the left in Fig. 3.10, and the area *M* corresponds to the location indicated by the "Matrix" arrow on the left in Fig. 3.10. Figure 3.11b shows the EDS mapping analysis results on the areas corresponding to Fig. 3.11a. The detection of Al, Si, and O on the fracture surface is represented by green, blue, and red, respectively. In Fig. 3.11b, the red area labeled *W* contained Al (82%) and O (18%), identifying this feature as an Al_2O_3 whisker (corresponding to '*W*' in Fig. 3.11a.), and the green area *M* contained

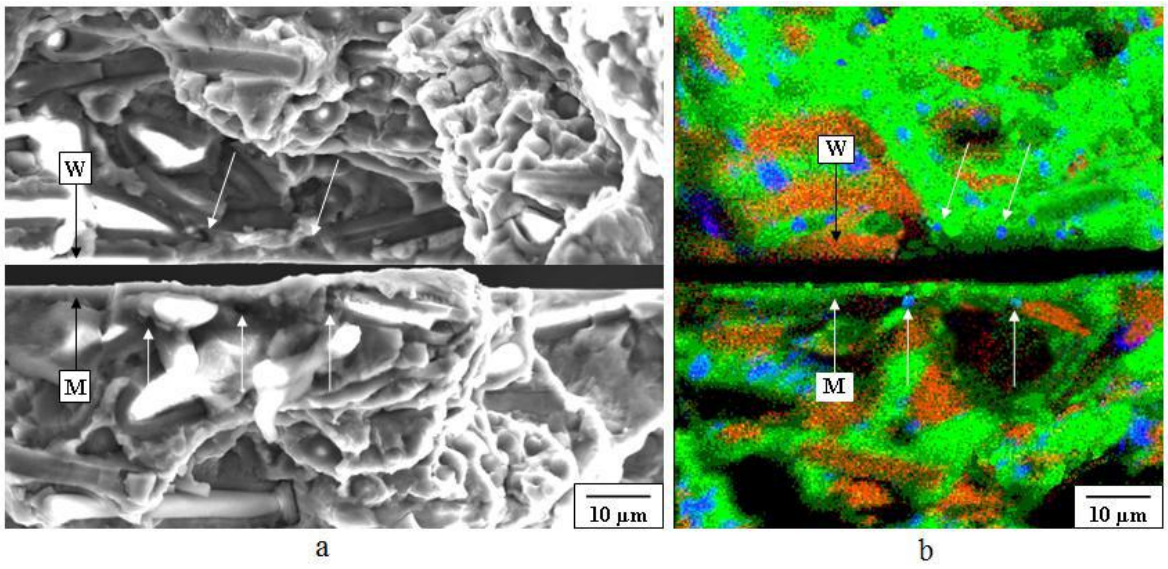

Fig. 3.11 Matching fracture surface of microcrack initiation site (a) SEM micrograph (b) EDS mapping analysis: MMC with Al_2O_3 whisker, 0.7 σ_c = 250 MPa.

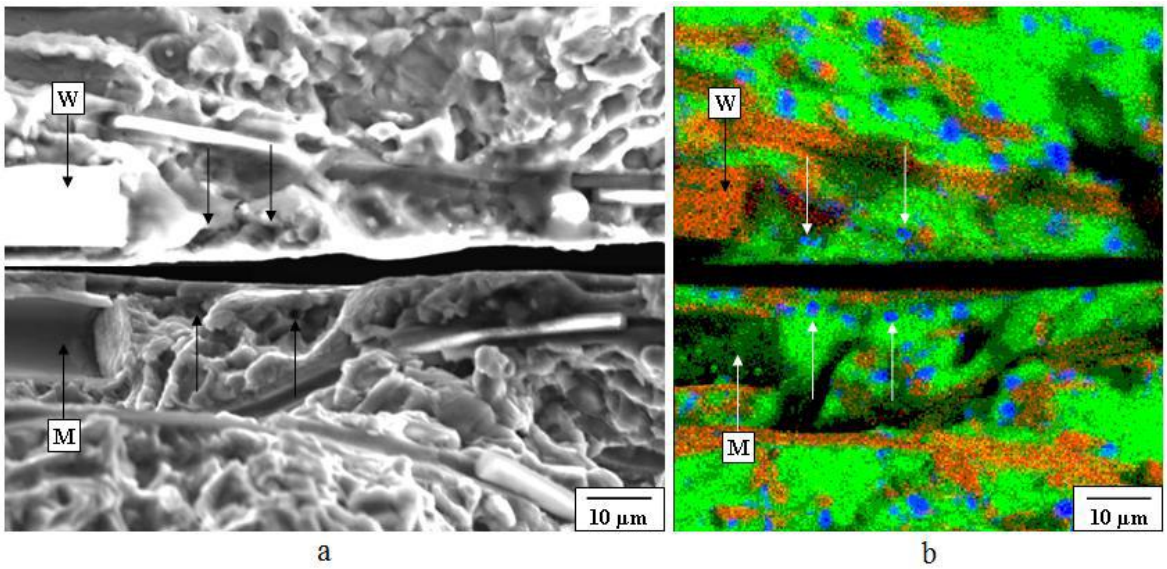

Fig. 3.12 Matching fracture surface of secondary microcrack initiation and coalescence site (a) SEM micrograph (b) EDS mapping analysis: MMC with Al_2O_3 whisker, 0.7 σ_c = 250 MPa

Al (94%) and Si (6%), indicating that this area is composed of Al matrix (corresponding to *M* in Fig. 3.11a). Therefore, the red and green area indicated by the *W-M* pair in the matching halves denoted Al_2O_3 whisker/matrix interfacial debonding where the crack initiation occurred next to the whisker (Fig. 3.9a). A few dimples originated at the crack initiation site (indicated by arrows in Fig. 3.11a) in the Al alloy matrix, but the edges are indistinct as compared with the one in the remote area. EDS analysis revealed the presence of a Si particle on the opposite side of the dimple-like shape (blue points indicated by arrows in Fig. 3.11b), meaning that void nucleation was induced by the plastic deformation at the Si particle. Similar results are shown in Fig. 3.12, which shows the matching fracture surface of the secondary microcrack initiation and coalescence site. The red area indicated by *W* in Fig. 3.12b represents the presence of Al_2O_3 whisker (corresponding to *'W'* in Fig. 3.12a) and the green area indicated by *M* in Fig. 3.12b represents the Al matrix (corresponding to *'M'* in Fig. 3.12a). Therefore, the *W-M* pair in the EDS mapping analysis shows the whisker/matrix interfacial debonding (corresponding to the *W-M* pair in Fig. 3.12a). Plenty of dimple like shape were observed in the fracture surface ahead of the *W-M* pair (indicated by arrows in Fig. 3.12a). The EDS mapping analysis confirmed the existence of Si particles on the opposite side of the dimples implies that the void nucleation is induced by the plastic deformation concentration in Al matrix at the second phase Si particles. However, the edge of the dimples is not so clear compared to the one of dimples in the unstable fracture region which implies the mutual contact effect due to cyclic loading. From these results, the fracture mechanism of the MMC with Al_2O_3 whiskers during cyclic loading is clearly illuminated. The interfacial debonding of Al_2O_3 whiskers and the Al alloy matrix was found at the crack initiation location (Fig. 3.11) as well as at the crack

coalescence location (Fig. 3.12). In addition, many voids and Si particles were observed at the crack initiation site (Fig. 3.11), indicating that the fracture mechanism of the MMC with Al_2O_3 whiskers was directed by whisker-matrix interfacial debonding followed by void nucleation in the Al alloy matrix.

3.4.3 Al alloy

Fig. 3.13 shows the crack initiation and propagation at various stages of fatigue life of the Al alloy at $0.7\sigma_c$ = 332 MPa peak stress. The large particle-shaped marks labeled *B* in Fig. 3.13 do not represent any particle; rather these are bubbles formed in the plastic replica. In the Al alloy, two cracks 25 and 40 μm long were initiated at 74% of the fatigue life (indicated by arrows in Fig. 3.13a). At 80% of the fatigue life, these two cracks joined and lengthened to 120 μm (arrow in Fig. 3.13b on the right). At this stage, many cracks 15-75 μm long were initiated (Fig. 3.13b) that grew on their own and coalesced with other nearby microcracks produced due to continued cycling. At 90% of the fatigue life, a few more microcracks less than 25 μm long were initiated between these cracks (indicated by arrows in Fig. 3.13c). At 98% of the fatigue life, the fatal crack was produced, and it joined all the cracks to attain a total length of 1250 μm (Fig. 3.13d). Similar microcrack initiation and coalescence phenomena were exhibited in the tests performed under other maximum stresses. The optical micrograph of the crack initiation site at the matching tensile surface of the fractured specimen is shown in Fig. 3.14. Microcracks were initiated in the Al grain, which deformed significantly and disrupted the focus of the image. Figure 3.15 shows the SEM micrograph of the matching fracture surface, including the crack initiation site. Plastic slip-like morphologies were observed in the crack initiation site along the specimen surface,

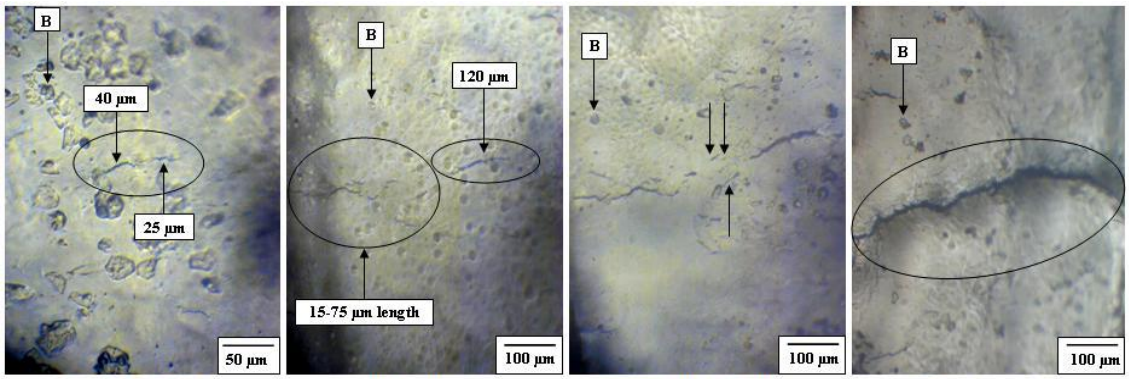

a. $N_1/N_f = 0.74$ b. $N_1/N_f = 0.8$ c. $N_1/N_f = 0.9$ d. $N_1/N_f = 0.98$

Fig. 3.13 Crack initiation and propagation at various stages of fatigue life of Al alloy : $0.7\sigma_c$ = 332 MPa, N_f = 70000 cycles

and many striation marks were observed on the inner side of the fracture surface (indicated by the "Striation" arrows in Fig. 3.15). Figure 3.16a shows the SEM micrograph of the matching fracture surface of the microcrack initiation site, showing a relatively smooth surface with dimples (indicated by arrows) and plastic slip lines. Fig. 3.16b shows the EDS mapping analysis results on the areas corresponding to Fig. 3.16a. EDS confirmed that the "plastic slip" region was Al and also revealed the presence of a few Si particles in the dimples (indicated by the arrow in Fig. 3.16b), meaning that void nucleation was induced by the plastic deformation of the Al matrix at the second phase Si particles. Moreover, Fig. 3.17 shows the fracture surface at the secondary microcrack initiation and coalescence site (corresponding to Fig. 3.13c). Numerous dimples were found in this fracture surface without any plastic slip lines. The presence of Si particles was also confirmed in this location by EDS (indicated by arrows in Fig. 3.17b). Fig. 3.18 shows the matching fracture

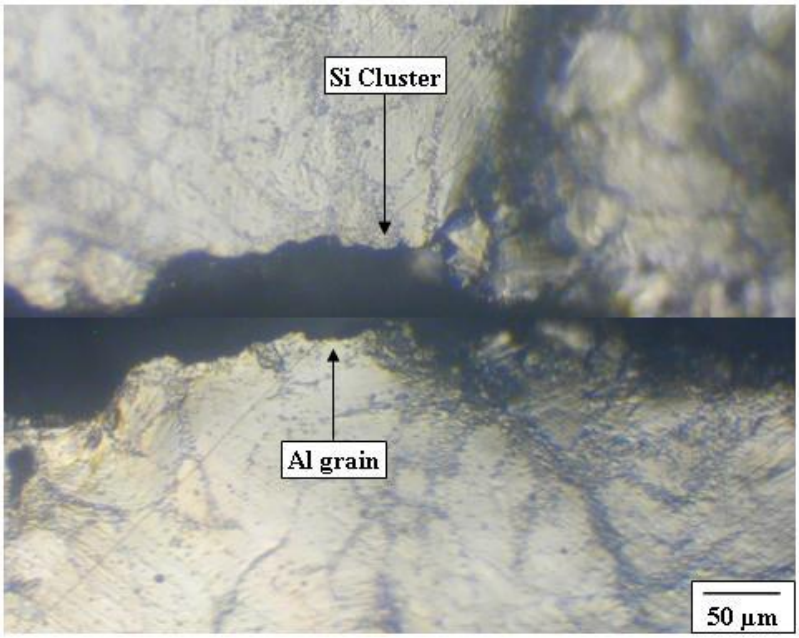

Fig.3.14 Optical micrograph of crack initiation site at the tensile surface of both side of the fractured specimen: Al alloy, $0.7\sigma_c$ = 332 MPa

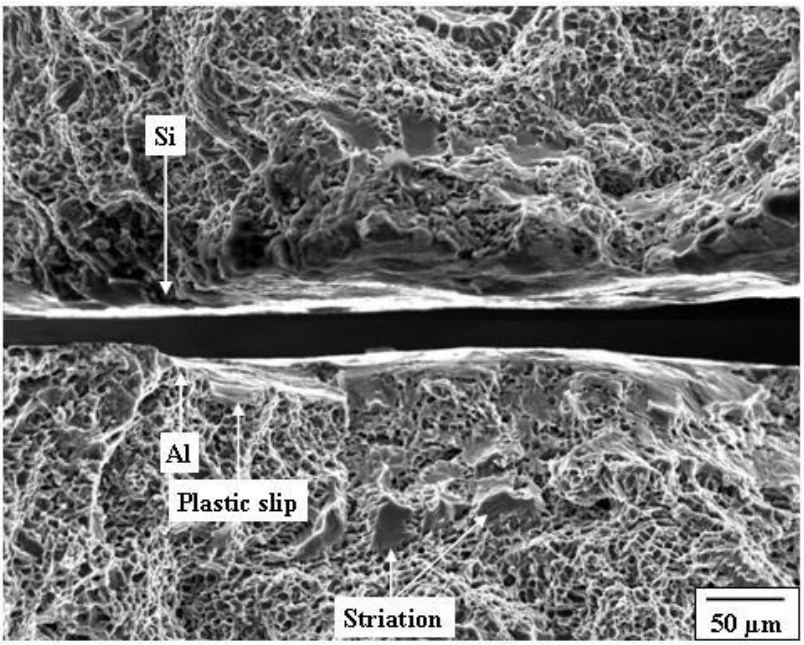

Fig.3.15 SEM micrograph of matching fracture surface: Al alloy, 0.7 σ_c = 332 MPa

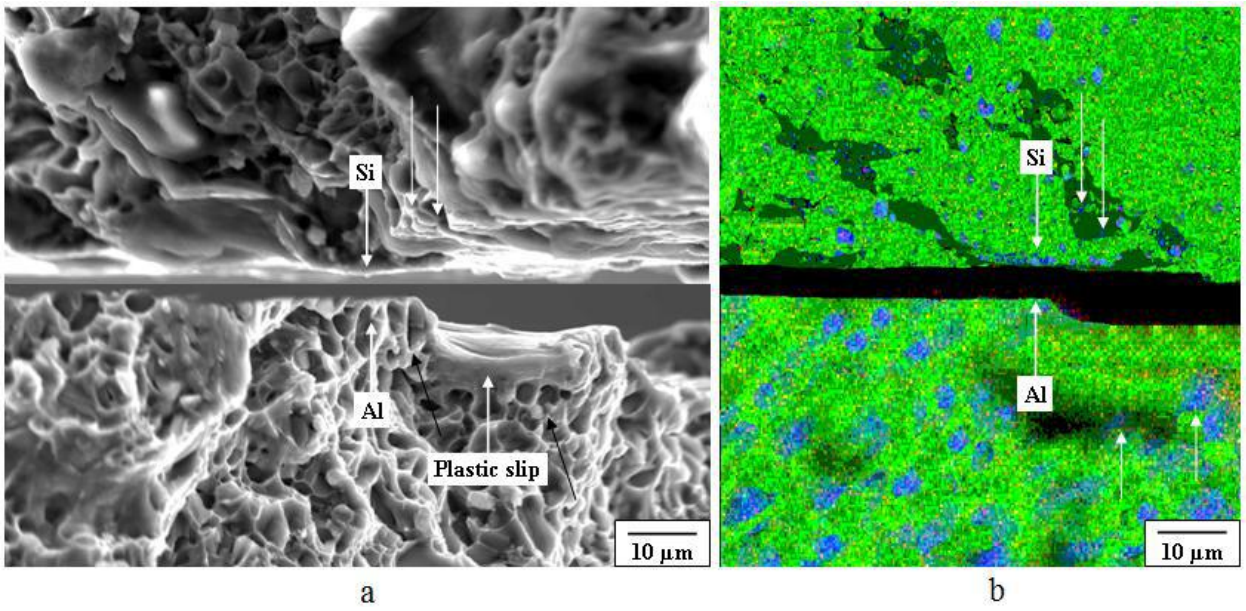

Fig. 3.16 Matching fracture surface of microcrack initiation site (a) SEM micrograph (b) EDS mapping analysis: Al alloy, 0.7 σ_c = 332 MPa

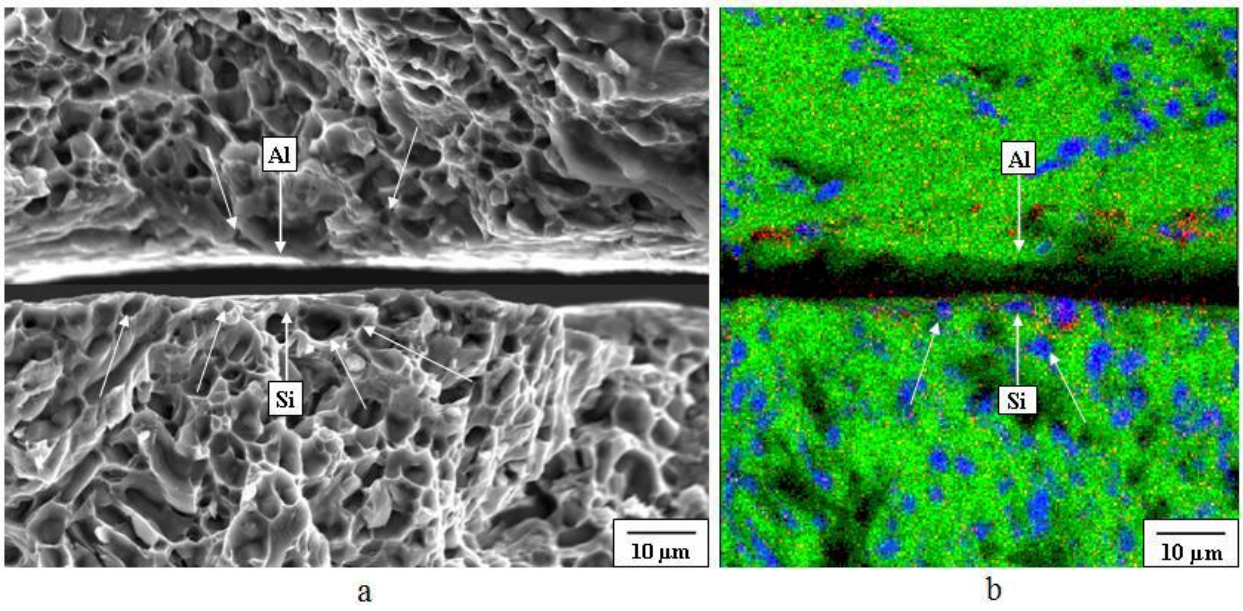

Fig. 3.17 Matching fracture surface of secondary microcrack initiation and coalescence site (a) SEM micrograph (b) EDS mapping analysis: Al alloy: 0.7 σ_c = 332 MPa.

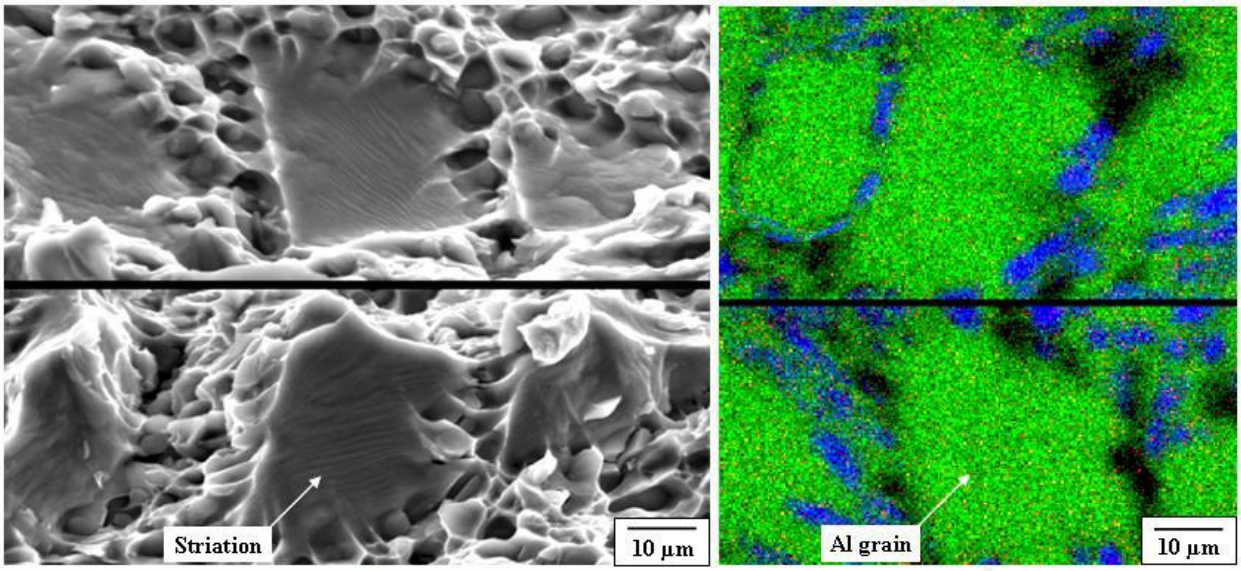

Fig. 3.18 Matching surface of striation (a) SEM micrograph (b) EDS mapping analysis: Al alloy, 0.7 σ_c = 332 MPa

surface of the striation, which was found on the inner side of the fracture surface along the crack propagation path (corresponding to the "Striation" arrow in Fig. 3.15). The large green area in Fig. 3.18b indicates the presence of Al grain where the striation formed (corresponding to the "Striation" arrow in Fig. 3.18a). Due to the presence of large Al grains, the plastic deformation became very high at this location during cyclic loading, and striation morphologies were formed along the crack propagation path. This observation clarifies that the fatigue fracture mechanism of the Al alloy was directed by the localization of the plastic slip in the Al grain followed by void nucleation, coalescence, and formation of striations due to high plastic deformation in the Al grain.

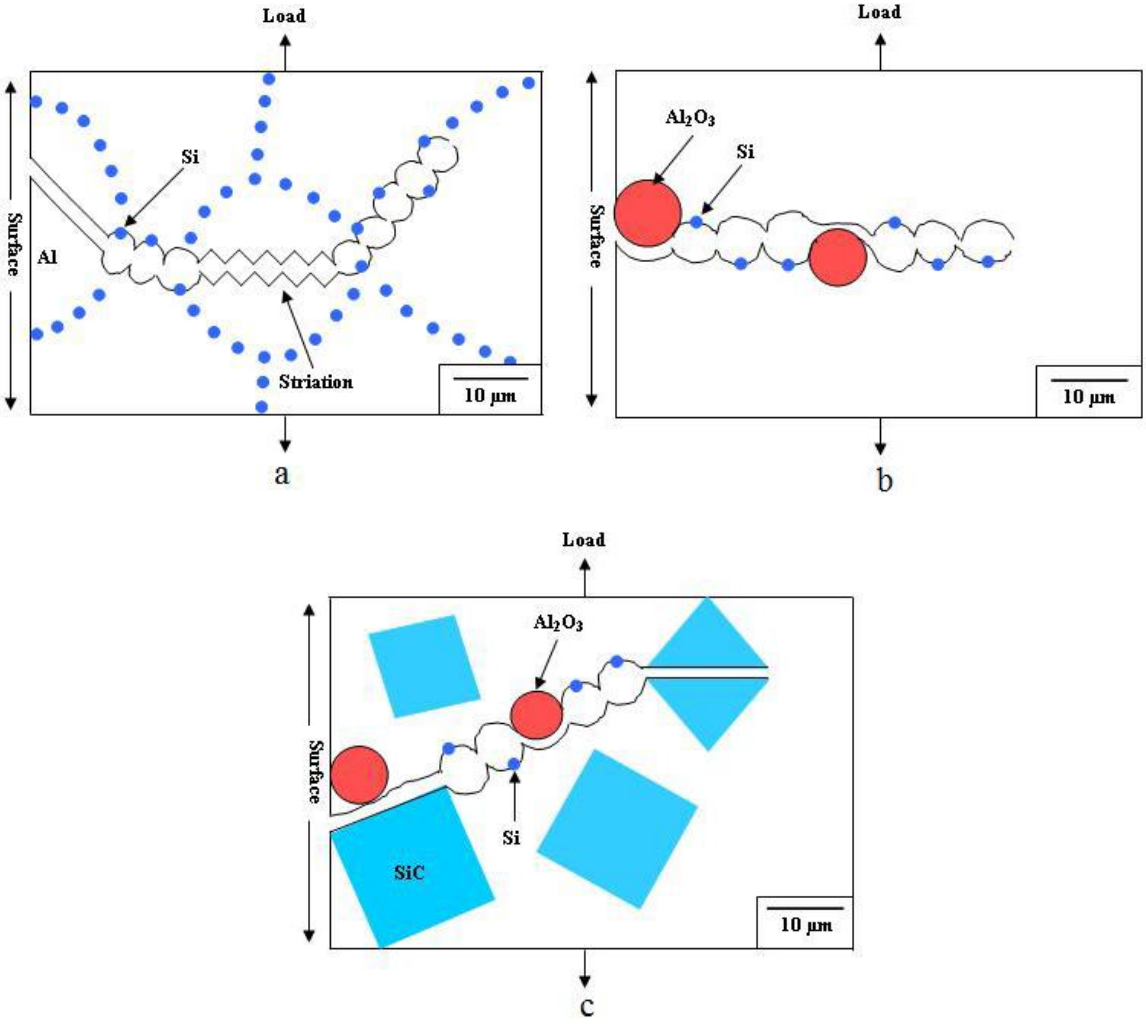

Fig. 3.19 Schematic diagram of fatigue crack initiation and propagation process at the fracture surface (a) Al alloy, (b) MMC with Al_2O_3 whisker and (c) Hybrid MMC

3.4.4 Discussion

Figure 3.19 illustrates the crack initiation mechanisms of Al alloy (a), MMC with Al_2O_3 whiskers (b) and hybrid MMC (c) in low cycle fatigue. From the above results, it is clear that in the unreinforced Al alloy, cracks usually initiated in the Al grain (Fig. 3.19a). In the Al alloy, only Si particles of average diameter 3 µm were present as inclusions.

There were no other high stiffness inclusions present in the Al alloy. Therefore, it experienced large plastic deformation during cyclic loading and crack initiated in the Al grain. Besides, the crack initiation sites in the MMC with Al_2O_3 whiskers were located near the edge of the whisker/matrix interface (Fig. 3.19b). On the contrary, the interface debonding between SiC particles near Al_2O_3 whiskers and the matrix is the main cause of crack initiation in hybrid MMC (Fig. 3.19c). Therefore, it appears that once reinforcement is added to the matrix, the crack initiation sites change from the Al grain to the interface of the reinforcement particles near the whiskers and matrix in hybrid MMCs. Moreover, it is observed in this research that the microcracks initiated very early, at only 11-16% of the fatigue life in the hybrid MMC (Fig. 3.3) under the applied stress conditions, whereas crack initiation was delayed slightly in the MMC with Al_2O_3 whiskers and was significantly delayed in the Al alloy (Fig. 3.3). This hybrid effect occurs because the elastic stiffness of ceramic is one order higher than that of the Si particles and the interaction between SiC particles and Al_2O_3 whiskers. During cyclic loading, the reinforcing particles and whiskers deformed elastically within the plastically deforming matrix alloy in low cycle fatigue. The stress on the particle/matrix or whisker/matrix interfaces was higher in the hybrid MMC because the reinforcements did not experience plastic deformation, and the separation of the particle and the whisker was small as compared with the MMC reinforced by Al_2O_3 whiskers. In addition, the edge of the stiff ceramic reinforcements acted as stress concentrators, localizing the plastic strain between the particles and the whiskers. Thus, a large strain mismatch occurred between these two reinforcement materials and the Al alloy. For this large strain mismatch, the stress became too high on the particle/matrix and whisker/matrix interfaces, and cracks initiated at these locations. Moreover, due to the

presence of high stiffness inclusions, large scale plastic deformation could not occur in the hybrid MMC, causing the nucleated voids in a concentrated area. After crack initiation, interfacial separation occurred in the particle/matrix and whisker/matrix interfaces, and voids formed ahead of the crack tip. The process continued until the crack met with another crack, leading to fatal fracture. The low cycle fatigue response of the composites is reduced compared to the monolithic Al alloy due to the short life for crack initiation at the interfaces.

3.5 Fatigue crack growth in high cycle fatigue

The investigation of the fatigue crack growth behaviour in high cycle fatigue were carried out on rectangular bar single edge notched specimen in accordance with the guidelines of ASTM E647. Figure 3.20 demonstrates the fatigue crack growth characteristics for the hybrid MMC, MMC with Al_2O_3 whiskers, and Al alloy under three regimes: near threshold, stable crack growth, and rapid crack growth. The composite material reinforced with only whiskers showed a higher crack growth rate (da/dN) than the monolithic alloy in the stable- and rapid-crack-growth regions. However, the hybrid MMC had a higher ΔK_{th} than the MMC with Al_2O_3 and the Al alloy, as summarized in Table 3.2. The higher value of ΔK_{th} for the hybrid MMC can be attributed to the higher modulus of the composite, which results in a lower crack-tip-opening displacement (CTOD) for a given applied ΔK. Treating the MMC as a homogeneous material, the CTOD of the three materials at threshold was calculated by using the following Dugdale model assuming small-scale yielding [70] and the results are presented in Table 3.2.

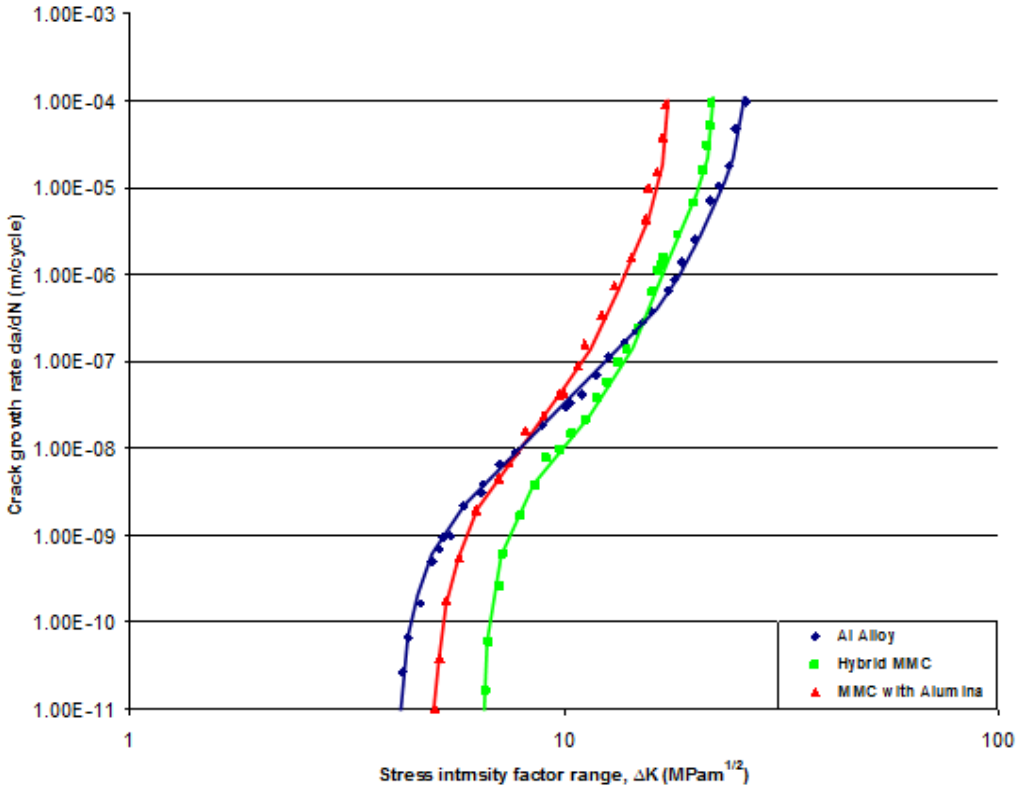

Fig. 3.20 Fatigue crack growth behaviour of hybrid MMC, MMC with Al_2O_3 whisker and Al alloy.

Table 3.2 Fatigue crack growth test results (unit: ΔK (MPa $m^{1/2}$), da/dN (m/cycle), CTOD (m))

Material	Fatigue threshold, ΔK_{th} (MPa $m^{1/2}$)	Paris Constant, C	Paris' exponent, m	CTOD at threshold
Hybrid MMC	6.6	8.7×10^{-15}	6	1.8×10^{-6}
MMC with Al_2O_3	5	2.2×10^{-14}	6.3	4×10^{-6}
Al alloy AC4CH	4.2	7.8×10^{-13}	4.5	1.9×10^{-6}

$$CTOD = \frac{K_1^2}{\sigma_{ys} E} \quad \text{.....(3.1)}$$

Where, K_1 is the stress intensity factor at the threshold, σ_{ys} is the yield strength and E is the young's modulus. These results show that the hybrid MMC had the lowest crack-opening displacement at the threshold stress intensity factor. Furthermore, the two composites showed higher values of the Paris-law exponent (m) than the unreinforced Al alloy, as presented in Table 3.2. The higher Paris-law slope of the composites is thought to be due to lower fracture toughness of the composites relative to the unreinforced alloy. Moreover, the hybrid MMC exhibited better FCG resistance than the MMC with Al_2O_3 over the entire stress intensity range.

3.6 Fatigue crack growth behaviour in high cycle fatigue

3.6.1 Hybrid MMC

Figures 3.21a and c illustrate the replica observation of FCG in the near-threshold and stable-crack-growth regions in the hybrid MMC. The horizontal arrows in the figures indicate the crack propagation direction. The value of da/dN was 1.64×10^{-11} m/cycle in the ΔK_{th} of 6.6 MPa $m^{1/2}$. Significant branching of the crack is seen near the crack tip at the threshold region (Fig. 3.21a). It has been reported that microstructural inhomogeneities such as inclusions, grain boundaries, and interfaces can generate crack kinking or branching, which cause significant retardation or even arrest of the subsequent crack propagation by reducing the crack driving force [11]. In the hybrid MMC, 21 vol% stiff SiC particles and 9 vol% Al_2O_3 whiskers were present as inclusions, and thus the development of crack branching was significant, resulting in a reduction of the crack growth rate. Moreover,

secondary microcracks with lengths of approximately 20–100 μm were observed ahead of the crack tip in both the regions (indicated by arrows in Figs. 3.21a and 3.21c). These secondary microcracks were formed at the interface of the SiC particles and the Al matrix.

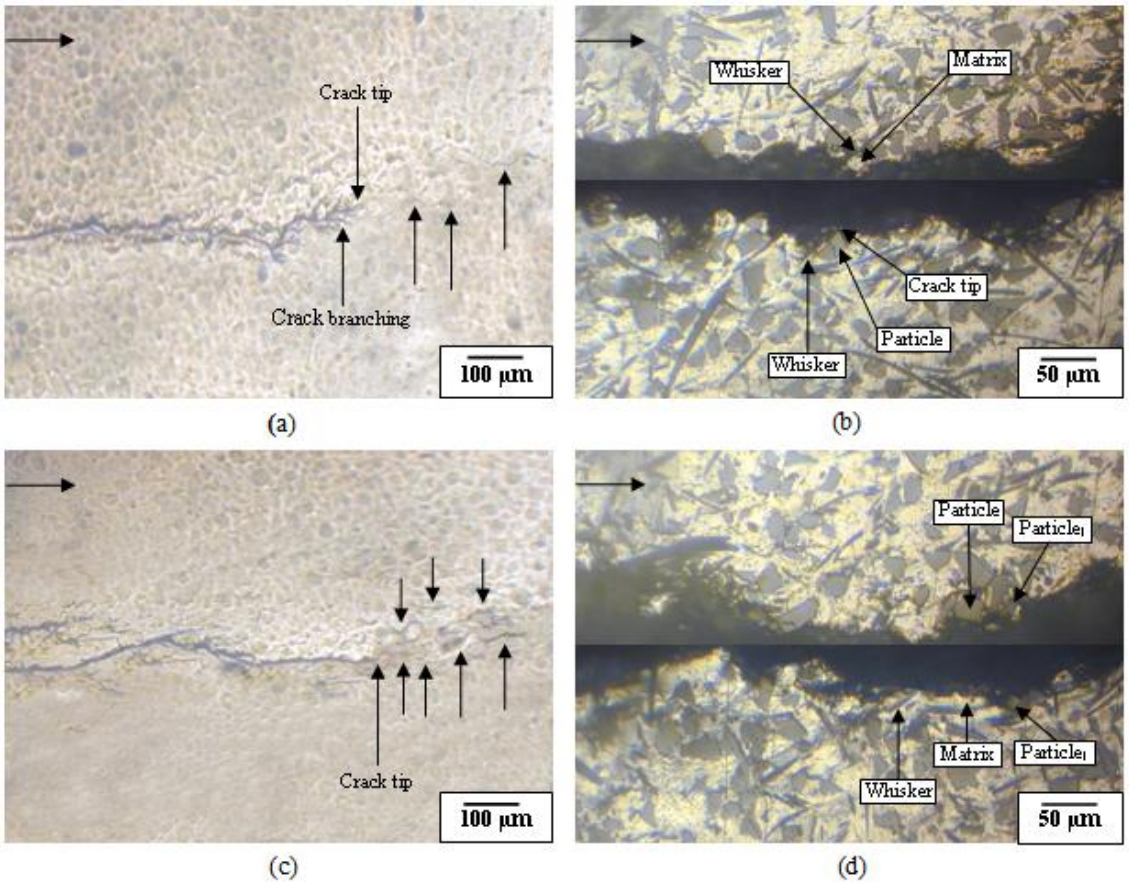

Fig. 3.21 Fatigue crack growth in hybrid MMC: (a) Replica observation at the near threshold region, (b) Matching tensile surface at the near threshold region, (c) Replica observation at the stable crack growth region, (d) Matching tensile surface at the stable crack growth region.

Table 3.3 Number of secondary microcracks formed in front of the crack tip of three materials at the near threshold region (range of ΔK (unit: (MPa $m^{1/2}$): Hybrid MMC 6.6-6.75, MMC with Al_2O_3 5-5.2 and Al alloy 4.2-4.45) and stable crack growth region (range of ΔK (unit: (MPa $m^{1/2}$): Hybrid MMC 12-12.6, MMC with Al_2O_3 10-10.7 and Al alloy 10.5-11)

Crack growth region	Number of secondary microcracks		
	Hybrid MMC	MMC with Al_2O_3	Al alloy
Near threshold	5	3	0
Stable crack growth	14	8	3

The number of secondary microcracks formed within a 300 × 300 μm area ahead of the crack tip was counted in both regions of all three materials and the results are presented in Table 3.3. It is evident from Table 3.3 and Figs. 3.21a and c that the number of secondary microcracks formed ahead of the crack tip in the stable-crack-growth region was reasonably higher than the microcracks formed in the threshold region in the hybrid MMC. Figures 3.21b and d show optical micrographs of the near-threshold and stable-crack-growth regions, respectively, at the matching tensile surface of the fractured specimen. It is apparent that the threshold occurred at the cluster of SiC particles and Al_2O_3 whiskers, as shown in Fig. 3.21b. No broken SiC particles were observed along the crack path in the near-threshold region (Fig. 3.21b), but partially broken particles were observed in the stable-crack-growth region (as indicated by the "$Particle_1$" and the "$Particle_1$" arrows in Fig. 3.21d). Furthermore, the debonding of the SiC particles and Al matrix was frequently seen in both regions (as indicated by the "Particle" and the "Matrix" arrows in Figs. 3.21b and 3.21d). Once a crack meets a particle, it avoids the particle and detours round it. Crack

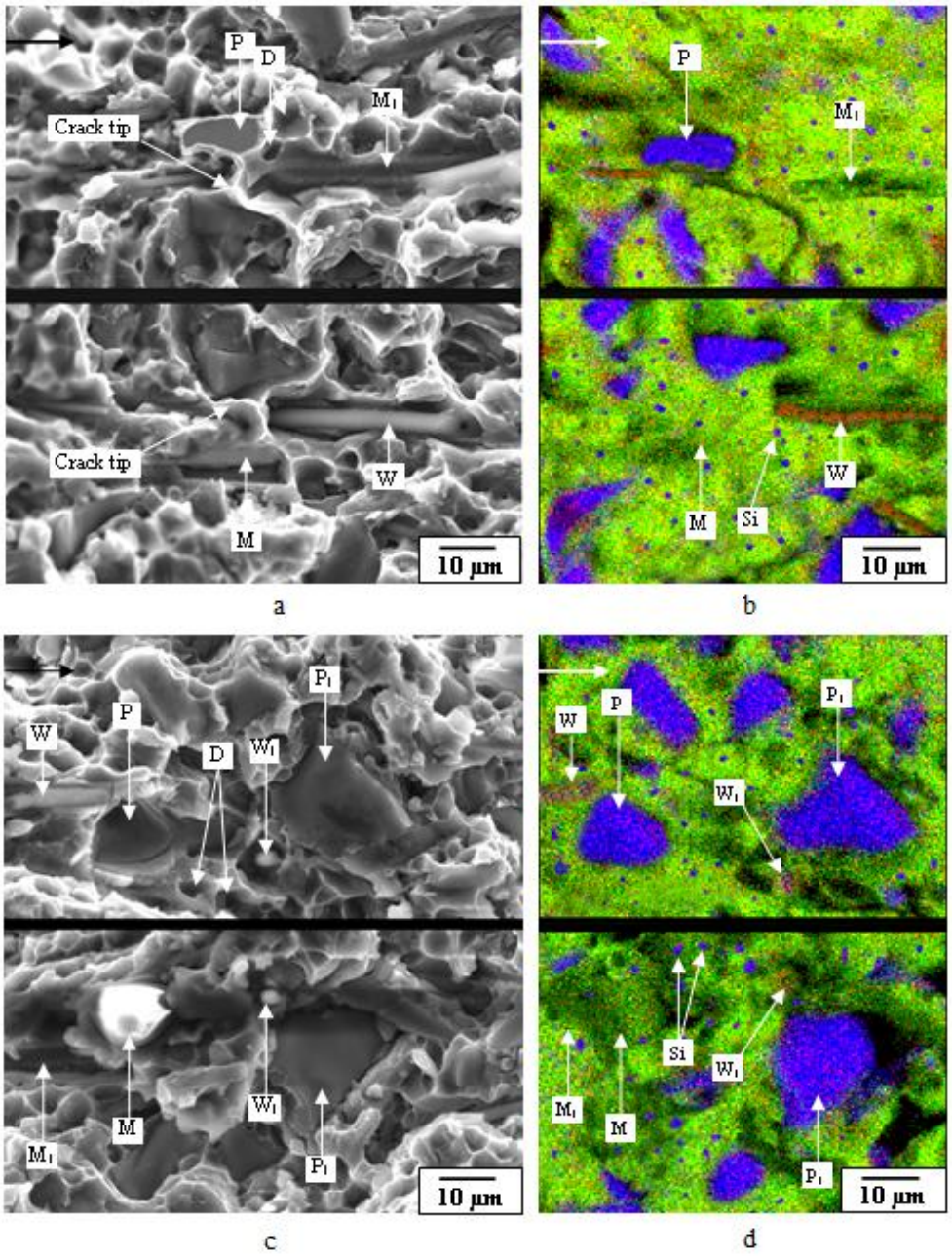

Fig. 3.22 Fatigue crack growth in hybrid MMC: (a) SEM micrograph at the near threshold region, (b) EDS analysis at the near threshold region, (c) SEM micrograph at the stable crack growth region, (d) EDS analysis at the stable crack growth region.

deflection around a particle is quite frequently seen regardless of ΔK value. During cyclic loading, the reinforcing particles deformed elastically within the plastically deforming matrix alloy and the stress on the particle–matrix interface was higher in the hybrid MMC [71]. Moreover, the edges of the stiff ceramic reinforcements acted as stress concentrators, localizing the plastic strain between the particles and the matrix. Thus, a large strain mismatch occurred between the SiC particles and the Al matrix. Under these conditions, the stress became too high on the particle–matrix interface and cracks deflected round the particles. Moreover, many Al_2O_3 whiskers were found fractured or debonded from the Al matrix along the crack path in the near-threshold region as well as in the stable-crack-growth region (as indicated by the "Whisker" arrows in Figs. 3.21b and 3.21d). With planar random orientation of the whiskers, cracks met the reinforcing whiskers either longitudinally or transversely. When a crack met a longitudinal whisker, the whisker fractured ahead of the crack tip (as indicated by the "Whisker" and the "Whisker" arrows in Fig. 3.21b). The fracture mode resembled sectional-cut rather than pull-out, even though sometimes the corresponding ΔK was low. However, when a crack met a whisker in the transverse direction, the whisker pulled the crack into the whisker–matrix interface and successive interfacial separation occurred (indicated by "Whisker" arrows in Fig. 3.21d). Figure 3.22a shows the SEM image of the matching fracture surface of the FCG at the near-threshold region. The clear crack front where the crack was arrested could not be identified on the inner side of the fracture surface. Figure 3.22b shows the EDS mapping analysis results of the areas corresponding to Fig. 3.22a. The green, blue, and red colors in Fig. 3.22b indicate the presence of Al, Si, and O, respectively, on the fracture surfaces. In Fig. 3.22b, the blue area indicated by *P* contains a significant amount of Si (96%) and a small

amount of Al (4%), which identifies the area as a SiC particle (corresponding to *P* in Fig. 3.22a). The green area indicated by *M* contains a large amount of Al (95%) and a small amount of Si (5%), indicating that this area is the Al matrix (corresponding to *M* in Fig. 3.22a). Therefore, the blue and green areas indicated by the *P–M* pairs in the matching halves denote SiC particle–matrix interfacial debonding at the near-threshold region. Moreover, the red area (indicated by *W* in Fig. 3.22b) contains a large amount of Al (84%) and a small amount of O (16%), indicating the presence of an Al_2O_3 whisker (corresponding to *W* in Fig. 3.22a). The green area indicated by M_1 on the opposite side of

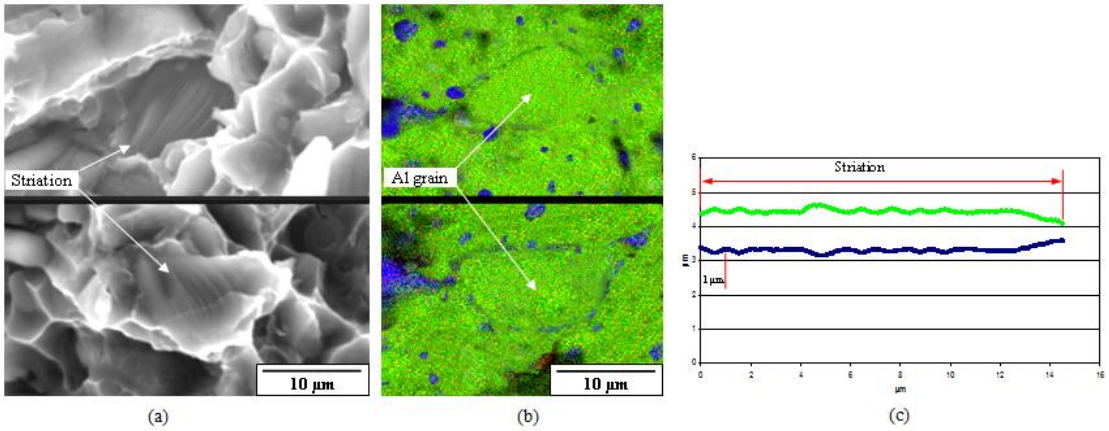

Fig. 3.23 Matching surface of striation formed in the stable crack growth region of hybrid MMC: (a) SEM micrograph, (b) EDS mapping analysis, (c) 3D analysis.

Table 3.4 Area fraction of striation in the stable crack growth region of three materials (ΔK: Hybrid MMC- 16.4 MPa $m^{1/2}$, MMC with Al_2O_3-13 MPa $m^{1/2}$ and Al alloy-18 MPa $m^{1/2}$)

Hybrid MMC	MMC with Al_2O_3	Al alloy
12.4%	41.5%	76.3%

the fracture surface indicates the Al matrix (Fig. 3.22b). Therefore, the *W–M*$_1$ pair in Fig. 3.22b (corresponding to the *W–M*$_1$ pair in Fig. 3.22a) denotes Al_2O_3 whisker–matrix interfacial debonding in the near-threshold region. Around the *P–M* and the *W–M*$_1$ pairs in Fig. 3.22a, a number of dimples were nucleated (indicated by the *D* arrow in Fig. 3.22a) in the Al alloy matrix. EDS mapping analysis confirmed the presence of a few Si particles on the opposite sides of the dimples (as indicated by the *Si* arrows in Fig. 3.22b). Dimple formation indicates the occurrence of void nucleation, which was induced by plastic deformation of the Al matrix around the second-phase Si particles. In addition, the SEM micrograph of the matching fracture surface of the FCG at the stable-crack-growth region and corresponding EDS mapping analysis results are presented in Figs. 3.22c and 3.22d, respectively. Similar observation of particle–matrix interfacial debonding, whisker–matrix interfacial debonding, and void nucleation/coalescence in the Al matrix was found in this region. Moreover, the blue *P*$_1$*–P*$_1$ pair and the red *W*$_1$*–W*$_1$ pair in Fig. 3.22d indicate the presence of SiC particles and Al_2O_3 whiskers, respectively, on both sides of the fractured surface, meaning that interfacial debonding was followed by transgranular fracture in this crack-growth region (corresponding to the *P*$_1$*–P*$_1$ pair and *W*$_1$*– W*$_1$ pair in Fig. 3.22c). Furthermore, striation marks were observed in a few places in the stable-crack-growth region, as shown in Fig. 3.23a. The average spacing of the striations was calculated to be 1.1 μm, which was very close to the d*a*/d*N* value of 1μm/cycle at this stage. Moreover, the area fraction of the striations in the hybrid MMC in the stable-crack-growth region was calculated to be only 12.4%, as shown in Table 3.4. The EDS mapping analysis confirmed that the striations formed in the Al matrix (Fig. 3.23b). Because of the high plastic deformation of the Al matrix, the striation morphologies formed in this crack-growth region

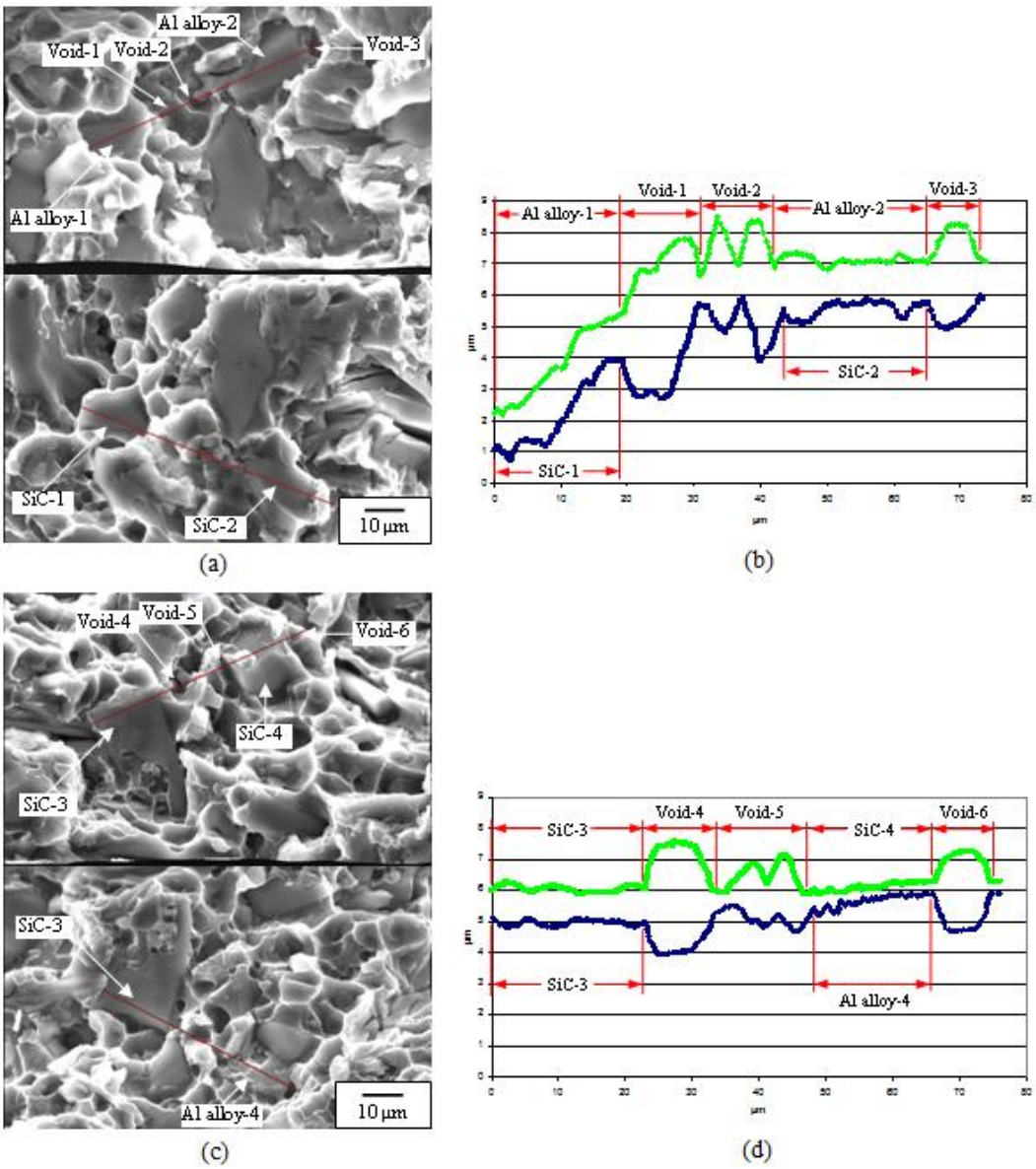

Fig.3.24 3D analysis of crack propagation from one SiC particle to another in hybrid MMC: (a) Matching fracture surface at the near threshold region, (b) Crack surface profile at the near threshold region, (c) Matching fracture surface at the stable crack growth region, (d) Crack surface profile at the stable crack growth region.

Table 3.5 Area fraction of SiC particle and Al_2O_3 whisker fracture and debonding between particle-matrix and whisker-matrix and area fraction of dimples of hybrid MMC in near threshold region (ΔK: 6.6 MPa $m^{1/2}$) and stable crack growth region (ΔK: 16.4 MPa $m^{1/2}$)

Crack growth region	SiC Particle		Al_2O_3 whisker		Dimple
	Fracture (%)	Debonding (%)	Fracture (%)	Debonding (%)	
Near threshold	3.7	17.4	1.6	4.9	72.4
Stable crack growth	19.5	5.6	3.4	6.3	52.8

during cyclic loading. However, the presence of Al_2O_3 whiskers and stiff SiC particles kept the striation formation in a very limited area in the hybrid MMC. Figure 3.23c represents the 3D analysis of the striation. The top-to-top and bottom-to-bottom correspondence of the cyclic roughness indicates the wake of the crack-tip blunting and resharpening. Figure 3.24 demonstrates the 3D analysis of crack propagation from one SiC particle to another SiC particle at the near-threshold and stable-crack-growth regions. The crack surface profile of Fig. 3.24b clearly exhibits the existence of submicron roughness on the debonded particle–matrix interface (indicated by SiC-1/Al alloy-1 pair and SiC-2/Al alloy-2 pair corresponding to the SiC-1/Al alloy-1 pair and SiC-2/Al alloy-2 pair in Fig. 3.24a). The edge of the dimple corresponds to the edge of the debonded interface, which means that the voids between the SiC–Al interfaces grow until they coalesce with the interfacial crack. The crack path was oblique in the near-threshold region depending on the orientation of the SiC–Al interface (SiC-1/Al alloy-1 pair) and became relatively flat with the transgranular fracture of the SiC particles (SiC-3/SiC-3 pair) as the value of ΔK increased, as illustrated by Figs. 3.24b and d. However, the interfacial fracture between SiC-4 and Al alloy-4, indicated as a cross- sectional shape in Fig. 3.24d, showed cyclic roughness, with an

interval having the same order of magnitude as the crack growth rate. This means that the crack grew cycle by cycle on the interface, indicating that debonding took place over a number of cycles. The area fraction of SiC particle and Al_2O_3 whisker fracture and debonding between particle–matrix and whisker–matrix and the area fraction of dimples at the near-threshold and stable-crack- growth regions in hybrid MMC are presented in Table 3.5. The results indicate that interfacial debonding is the dominant mechanism of crack growth in the near-threshold region, whereas particle fracture and whisker fracture play a vital role during crack growth in the mid-growth region. However, dimple formation was highly dominant in both regions. From the above observations, the FCG behavior of hybrid MMC in high cycle fatigue is clearly perceived. At the near-threshold region, where the ΔK value is very low, the crack propagated by particle–matrix and whisker–matrix interfacial debonding followed by void nucleation and coalescence. Further, with the higher ΔK values in the stable-crack-growth region, the crack propagated by the interfacial debonding of particle–matrix and whisker–matrix caused by the cycle-by-cycle crack growth on the interface, as well as by the transgranular fracture of particles and whiskers followed by striation formation and void nucleation in the Al alloy matrix.

3.6.2 MMC with Al_2O_3 whiskers

Figures 3.25a and c show the replica observation of FCG in the near-threshold and stable-crack-growth regions in the MMC with Al_2O_3 whiskers. It was seen on the specimen surface that the threshold occurred at the edge of a whisker angled toward the crack path. The value of da/dN was 1.02×10^{-11} m/cycle in a ΔK_{th} of 5 MPa $m^{1/2}$. Because of the

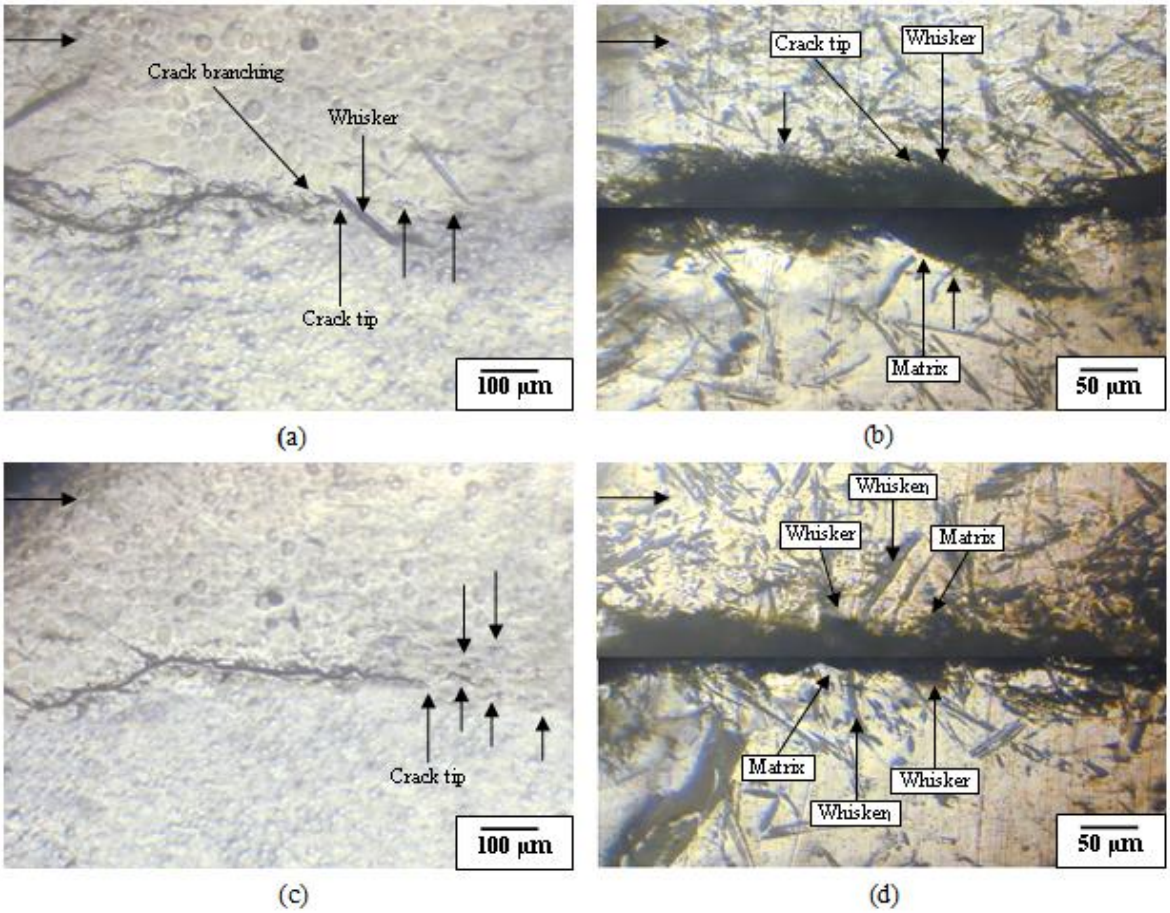

Fig. 3.25 Fatigue crack growth in MMC with Al_2O_3 whisker: (a) Replica observation at the near threshold region, (b) Matching tensile surface at the near threshold region, (c) Replica observation at the stable crack growth region, (d) Matching tensile surface at the stable crack growth region.

absence of interfacial fracture between the SiC particles and the Al matrix, the branching of cracks in the MMC with Al_2O_3 whiskers (indicated by arrow in Fig. 3.25a) was found to be less than that occurred in the hybrid MMC (indicated by arrow in Fig. 3.21a). Moreover, the number of secondary microcracks formed in the stable-crack-growth region of the MMC with Al_2O_3 whiskers was found to be reasonably less than that of the hybrid MMC,

as presented in Table 3.3. Figures 3.25b and d show the optical micrograph of the near-threshold and stable-crack growth regions, respectively. The whisker shown in Fig. 3.25a was debonded from the matrix (indicated by "Whisker" and "Matrix" in Fig. 3.25b) as the crack grew under a ΔK that was relatively higher than the threshold value. Crack deflection was smaller in the MMC with Al_2O_3 than in the hybrid MMC. Figures 3.26a and b illustrate the SEM micrograph and corresponding EDS mapping analysis results, respectively, of the matching fracture surface of the FCG in the near-threshold region. The vertical dotted lines in Figs. 3.26a and 3.26b indicate the locations where the threshold occurred. The observed Al_2O_3 whisker–matrix interfacial debonding (*W–M* pair) and whisker fracture (W_1–W_1 pair) are similar to that in the hybrid MMC at the near-threshold and the stable-crack-growth regions. A few dimples originated at the near-threshold region (indicated by *D* arrow in Fig. 3.26a) in the Al alloy matrix but the edges are indistinct. Al_2O_3 whiskers (*W* and W_1 in Figs. 3.26a and 3.26b) are present ahead of the crack tip when the threshold is reached, which indicates that the crack is arrested when it meets Al_2O_3 whiskers at the inner part of the specimen. Significant numbers of striation marks were observed in the stable-crack-growth region (indicated by the "*Striation*" arrows in Fig. 3.26c). A high-magnification view of the striation is shown in Fig. 3.27a, which correspond to the striation marks shown in Fig. 3.26c. The area fraction of the striations in the MMC with Al_2O_3 in the stable-crack-growth region was calculated to be 41.5%, as shown in Table 3.4. The EDS mapping analysis confirmed that the striations formed at the Al matrix (Fig. 3.26b). Because of the presence of only 9 vol% of Al_2O_3 whiskers as reinforcement, the inter-reinforcement spacing in the MMC with Al_2O_3 whiskers is reasonably large and relatively large Al grains are present as

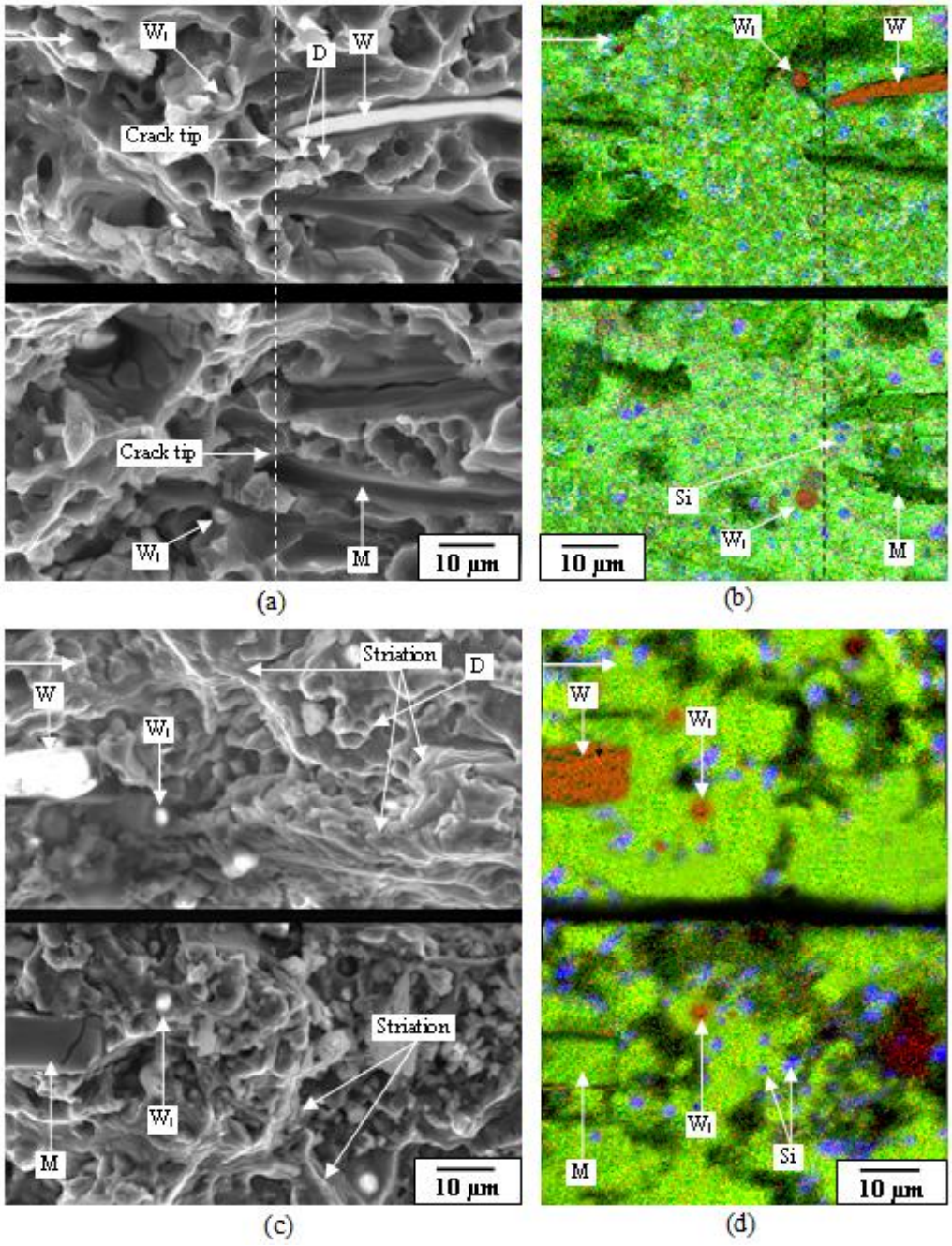

Fig. 3.26 Fatigue crack growth in MMC with Al_2O_3 whisker: (a) SEM micrograph at the near threshold region, (b) EDS analysis at the near threshold region, (c) SEM micrograph at the stable crack growth region, (d) EDS analysis at the stable crack growth region.

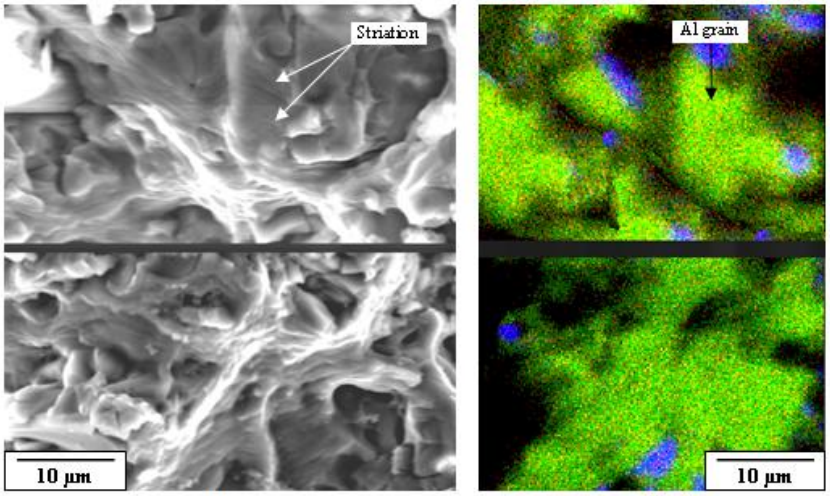

Fig. 3.27 Matching surface of striation formed at the stable crack growth region of MMC with Al_2O_3 whisker (a) SEM micrograph, (b) EDS mapping analysis.

compared to hybrid MMC. Formation of a multiple slip system is available because of the large Al grains. Thus, striation morphologies were formed over a relatively larger area in the MMC with Al_2O_3 whiskers as compared to the hybrid MMC. The 3D analysis of crack propagation from one Al_2O_3 whisker to another Al_2O_3 whisker in the threshold and stable-crack-growth regions is presented in Fig. 3.28. The debonding of the whisker–matrix interface (indicated by Whisker-1/Al alloy-1 pair and Whisker-2/Al alloy-2 pair) and void nucleation in the near-threshold region is observed in the crack surface profile of Fig. 3.28b. The dimple surface connects the interval between the interfacial fractures. Figure 3.28d clearly demonstrates the transgranular fracture of the whisker (indicated by Whisker-4/Whisker-4 pair) and the debonding of the whisker–matrix interface (indicated by Whisker-3/Al alloy-3 pair) in the stable-crack-growth region. The striation morphology on

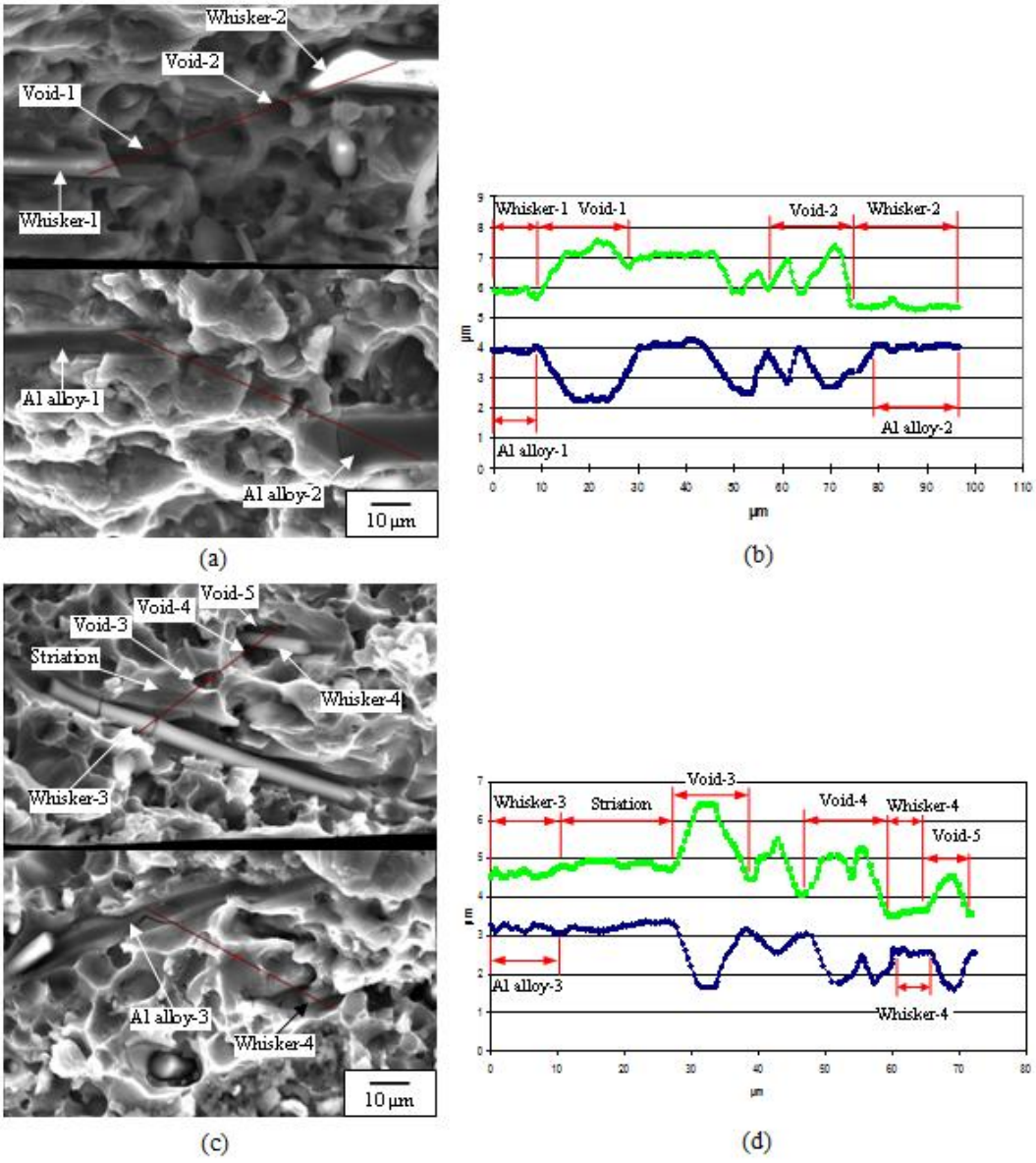

Fig.3.28 3D analysis of crack propagation from one Al_2O_3 whisker to another in MMC with Al_2O_3 whisker: (a) Matching fracture surface at the near threshold region, (b) Crack surface profile at the near threshold region, (c) Matching fracture surface at the stable crack growth region, (d) Crack surface profile at the stable crack growth region.

the whisker–Al matrix interface continues into the Al matrix (Whisker-3 and Al alloy-3 and Striation in Fig. 3.28d) and reaches the voids (Void-3 and Void-4). In addition, in Fig. 3.28d, the interval of the cyclic roughness of the interfacial fracture between whisker-3/Al alloy-3 shows the same order of magnitude as the crack growth rate at this stage. This means that the crack grew on the interface over a number of cycles, causing debonding of the interface. These results indicate that at lower ΔK values, fatigue crack growth is controlled by debonding of the whisker–matrix interface and void nucleation and coalescence in the Al alloy matrix. However, at higher ΔK values, FCG is controlled by debonding of the whisker–matrix interface caused by the cycle-by-cycle crack growth on the interface, as well as whisker fracture followed by striation formation and void nucleation in the Al matrix.

3.6.3 Al alloy

The replica observation and the corresponding surface of FCG in the threshold region of the Al alloy are shown in Figs. 3.29a and 3.29b, respectively. It is obvious from Fig. 3.29b that the fatigue threshold occurred at the cluster of Si particles on the specimen surface. The value of da/dN was 2.72×10^{-11} m/cycle in the ΔK_{th} of 4.2 MPa $m^{1/2}$. Moreover, Figs. 3.29c and 3.29d represent the replica observation and optical micrograph, respectively, of the Al alloy in the stable-crack-growth region. It was observed that the crack moved along the boundary between the Si particle cluster and the Al grains on the specimen surface (as indicated by the "*Si cluster*" and the "*Al grain*" arrows in Fig. 3.29d). Crack branching and secondary microcracks were found very less near the crack tip at the near-threshold and stable-crack-growth regions (Figs. 3.29a and 3.29c) in comparison with the hybrid MMC

and the MMC with Al_2O_3 whiskers. In the Al alloy, only Si particles 3μm in diameter are present as inclusions. Therefore, the microstructural homogeneity of this material is higher than those of the other two composite materials and limited crack branching is seen during FCG.

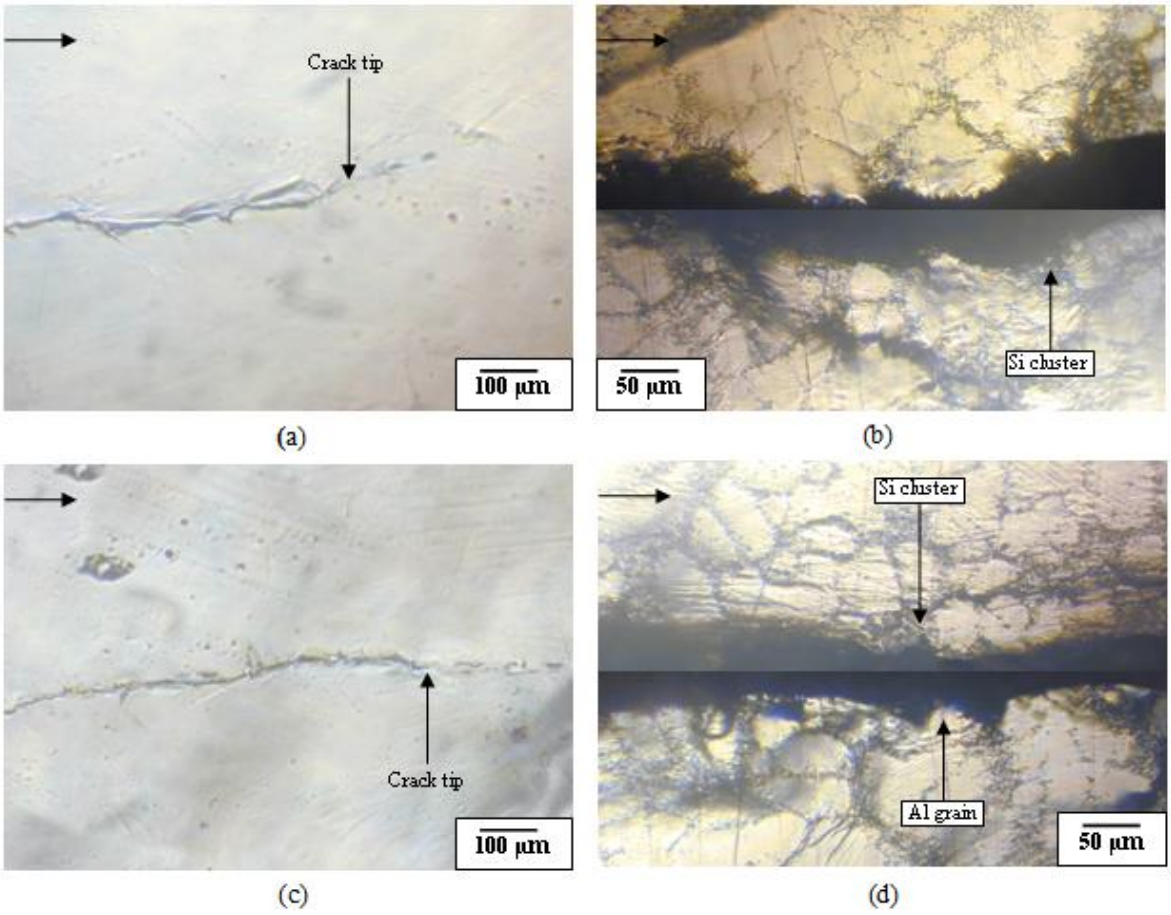

Fig.3.29 Fatigue crack growth in Al alloy: (a) Replica observation at the near threshold region, (b) Matching tensile surface at the near threshold region, (c) Replica observation at the stable crack growth region, (d) Matching tensile surface at the stable crack growth region.

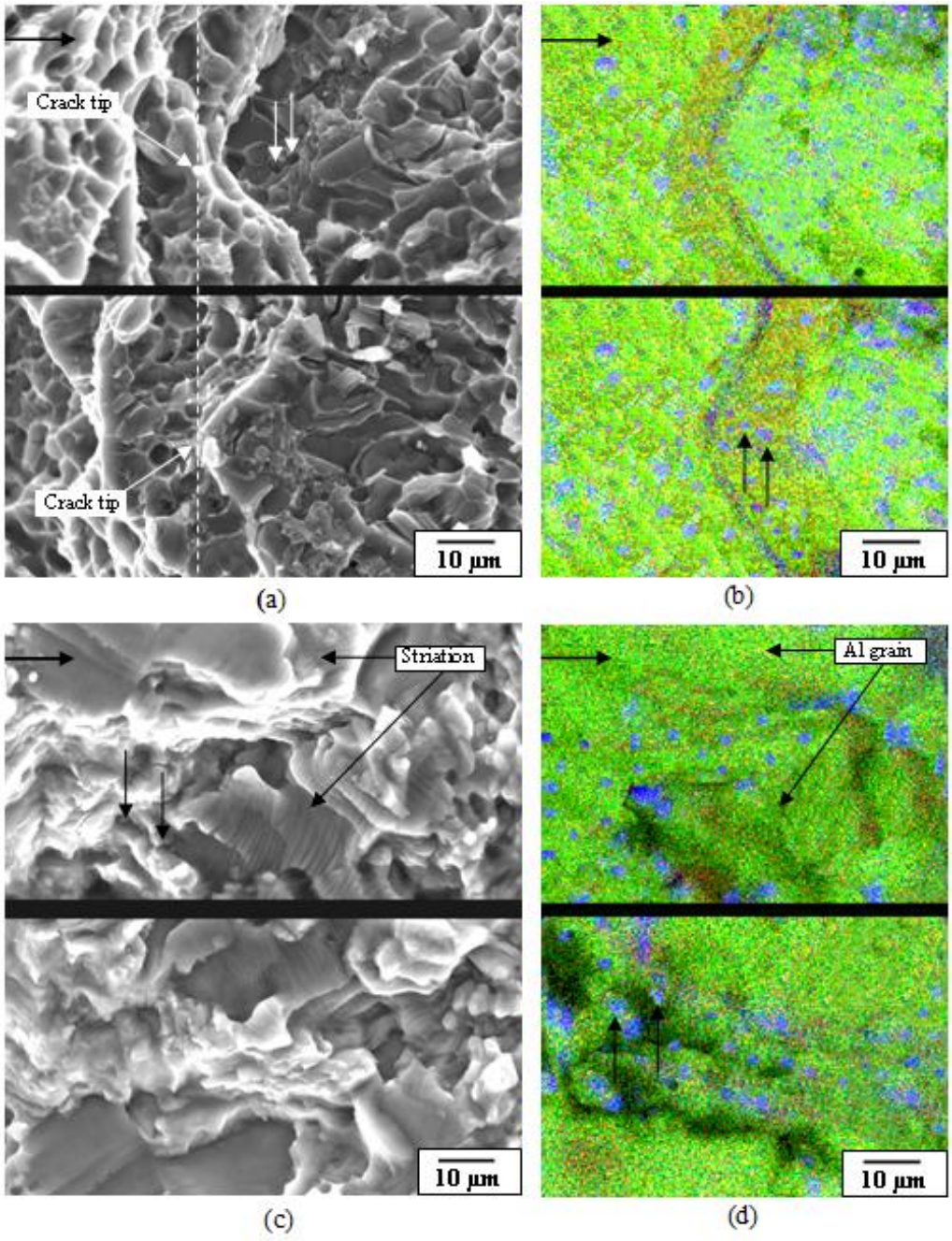

Fig. 3.30 Fatigue crack growth in Al alloy: (a) SEM micrograph at the near threshold region, (b) EDS analysis at the near threshold region, (c) SEM micrograph at the stable crack growth region, (d) EDS analysis at the stable crack growth region.

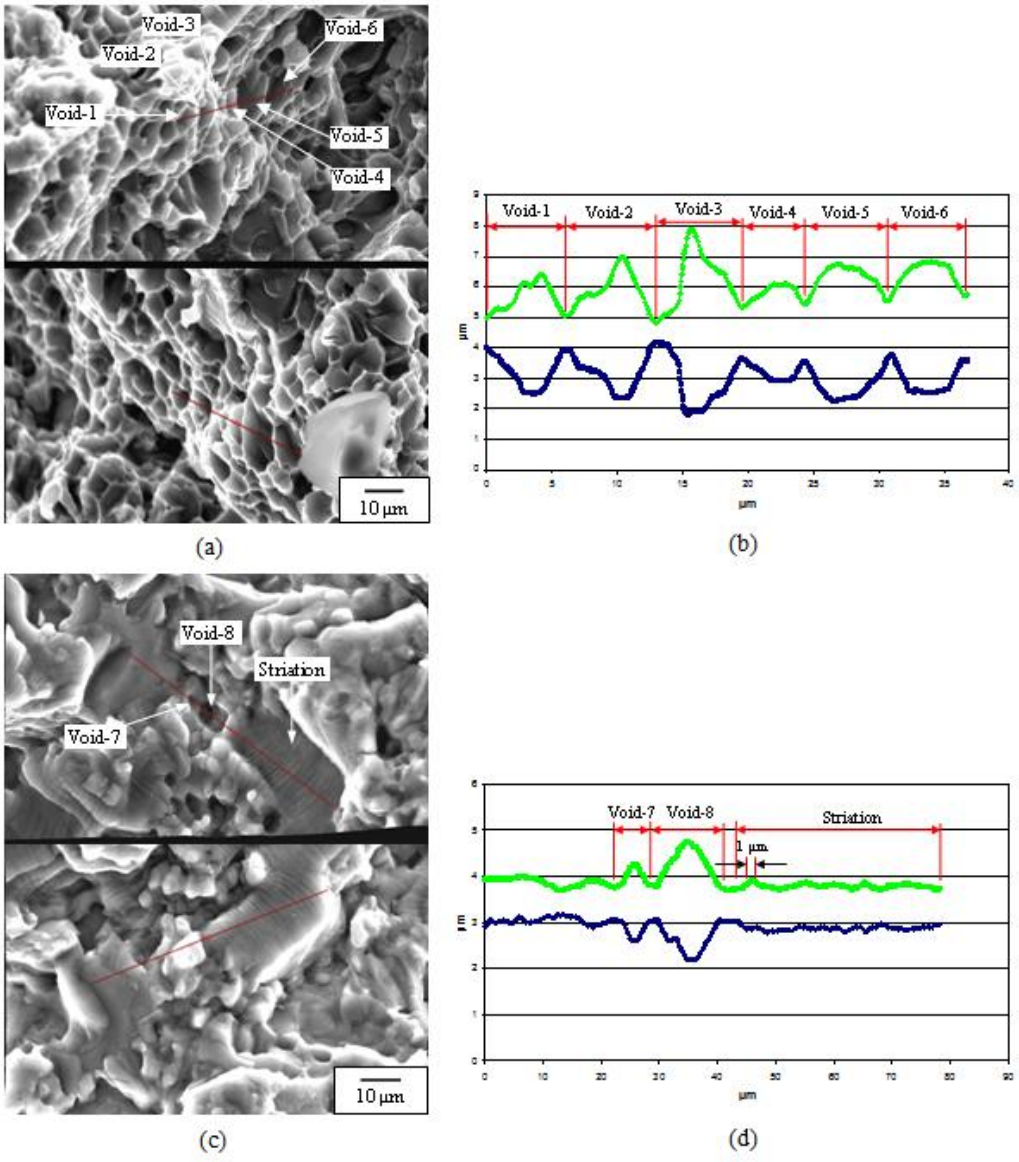

Fig. 3.31 3D analysis of crack propagation in Al alloy: (a) Matching fracture surface at the near threshold region, (b) Crack surface profile at the near threshold region, (c) Matching fracture surface at the stable crack growth region, (d) Crack surface profile at the stable crack growth region.

Figure 3.30a shows the SEM micrograph of the matching fracture surface of the Al alloy at the near-threshold region, showing a relatively smooth surface with dimples (indicated by arrows). In the EDS mapping in Fig. 3.30b, Si particles are observed on the fracture surface, which means the crack has reached its threshold at the particle cluster at the inner side of the specimen. Moreover, Figs. 3.30c and d represent the fracture surface and the corresponding EDS analysis results, respectively, at the stable-crack-growth region. Numerous striation marks were observed in this fracture surface along the crack propagation path (indicated by the "*Striation*" arrow in Fig. 3.30c). The average spacing of the striations was calculated to be 1 μm, which is close to the value of da/dN at this stage. The area fraction of the striations in this region was calculated to 76.3%, as shown in Table 3.4. The large green areas in Fig. 3.30d confirmed the presence of Al grains where striations formed. No Si particles were observed on the striation fracture surface. In the stable-crack-growth region, multiple slip systems were in operation because of the presence of large Al grains. Consequently, striation morphologies were formed in large Al grains along the crack propagation path during cyclic loading. Moreover, in the stable-crack-growth region, the number of dimples were found limited in the cluster of Si particles (indicated by arrows in Fig. 3.30c). Figure 3.31 represents the 3D analysis of crack propagation in the Al alloy at the near-threshold and stable-crack-growth regions. The crack surface profile of both regions clearly demonstrated that the cracks propagated by void nucleation and coalescence in the near-threshold region and by striation formation, as well as void nucleation in the stable-crack-growth region. Moreover, the interval of the cyclic roughness in the striation morphology shown in Fig. 3.31d indicates that the crack

with striation formation penetrated the voids, which means that the two striation facets were formed followed by the void nucleation and coalescence.

3.6.4 Discussion

Figure 3.32 illustrates the FCG mechanism of the hybrid MMC, MMC with Al_2O_3 whiskers, and Al alloy under two different crack growth regimes. The figure shows that the fatigue crack growth mechanism in the two different regimes and three different materials is strikingly different. Figures 3.32a, c, and e illustrate the crack growth mechanism in the near-threshold region of the three materials. It appears that reinforcement debonding is the dominant mechanism of crack growth in the near-threshold region for both composite materials. The fatigue threshold ΔK_{th} and crack growth in the near-threshold regime was previously explained in terms of crack closure [72]. It has been reported that several variables, including crack surface roughness, yield strength, and elastic modulus can influence crack closure and the value of the fatigue threshold ΔK_{th} [72, 73]. Because the hybrid MMC contains SiC particles and Al_2O_3 whiskers, modulus mismatch occurred between the particles, whiskers, and matrix. From the 3D analysis (Figs. 3.24a and b), the fracture of interface between the SiC particles and the Al alloy matrix is very frequently seen in the near-threshold region of hybrid MMCs, which leads to an increase in surface roughness as compared to the other two materials. Consequently, the fatigue threshold ΔK_{th} in the hybrid MMC increased. Furthermore, the elastic modulus and yield strength are also two important variables that can influence crack closure. It has been stated that a high modulus promotes crack closure [74]. In the mechanical properties set out in Table 2.2, the elastic modulus of the hybrid MMC is higher than that of the other two materials. Therefore,

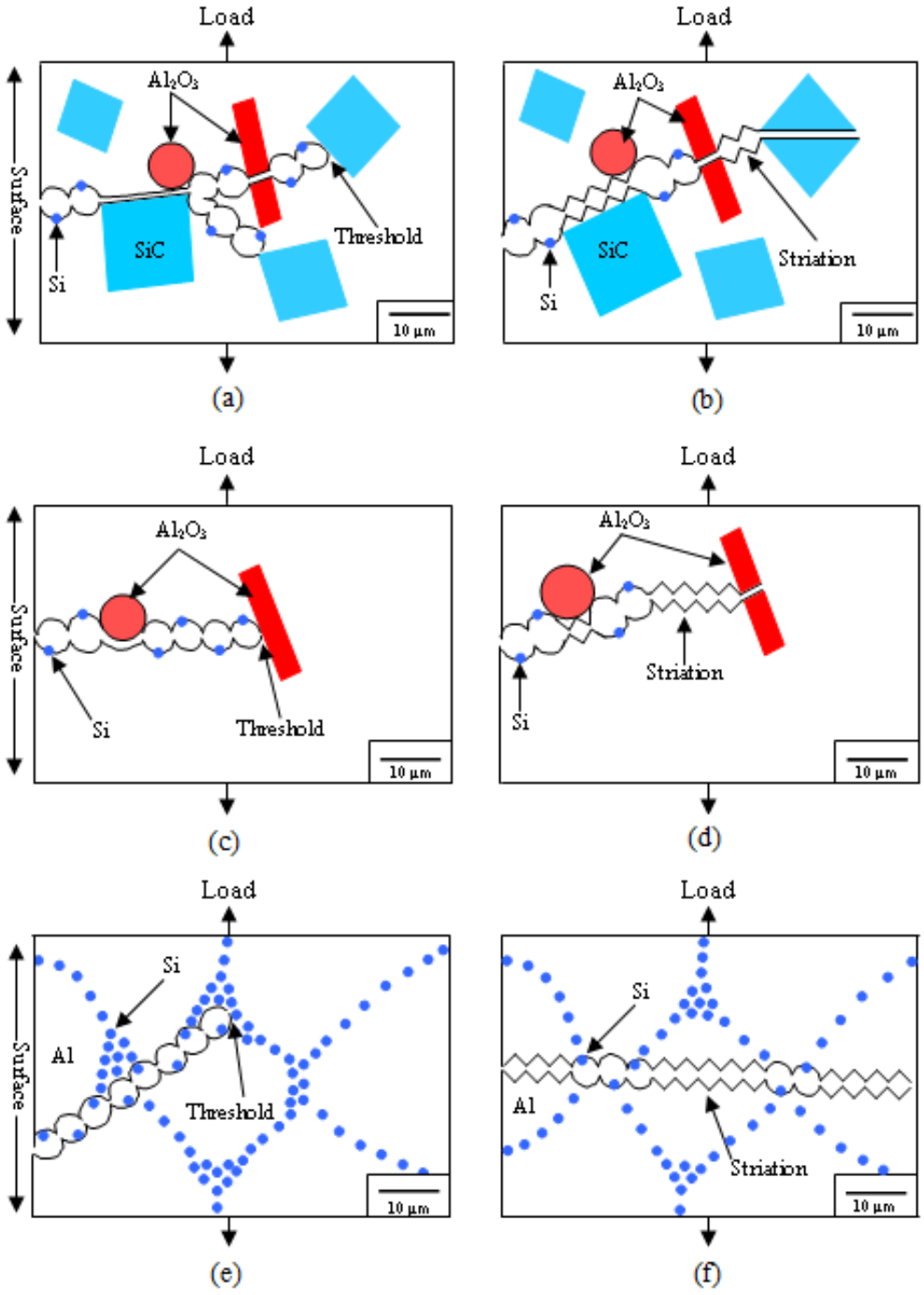

Fig. 3.32 Schematic diagram of fatigue crack growth mechanism at the near threshold region and stable crack growth region (a) (b) Hybrid MMC (c) (d) MMC with Al_2O_3 whisker and (e) (f) Al alloy.

the crack growth resistance of the hybrid MMC was higher and the fatigue threshold increased. Figures 3.32b, d, and f illustrate the crack growth mechanism in the stable- or mid–crack-growth regions of the three materials. Particle and whisker debonding from the matrix caused by the cycle-by-cycle crack growth on the interface and particle fractures in the hybrid MMC are frequently seen in this regime. It has been stated that when the plastic zone is much larger than the size of the particles, particle fracture may take place. Inserting the reinforcing particles and whiskers reduce striation formation owing to the fracture of the reinforcing materials. The reduction of striation formation thus increases the crack propagation rate in the two MMCs.

CHAPTER-4

NUMERICAL ANALYSIS

4.1 Introduction

This chapter describes the hybrid effect and reinforcement clustering effect on the crack initiation mechanism of cast hybrid MMC by using finite element method (FEM). For understanding the characteristics of the elastic-plastic stress fields, a numerical analysis is carried out on the reinforcing particles, whiskers and matrix in the clustering and non-clustering regions of cast hybrid MMC. The stress distribution at the reinforcement–matrix interface in the cast hybrid MMC is also described in this chapter.

In the past many years, many researchers have made use of the computational and analytical method to understand and characterize mechanical properties and performance of metal matrix composite such as mechanisms of strengthening and of microscopic damage and failure [75-80]. To investigate the monotonic and cyclic deformation behavior of MMCs, a large number of finite element analyses have been carried out by using unit cell modeling approach [75-78]. Some of the studies concerned with the effect of particle size, shape and distribution on mechanical performance of MMCs by using multi particle unit cell model [79]. Cubic shaped inclusions in a 3-D unit cell model were used for describing the particle distribution effect in MMCs [80-82]. The influence of the particle shape, size and distribution on ductility of SiC particulate MMC has been successfully predicted by using periodic 3-D unit cell concept [80]. Moreover, several attempts have been made to study the interface strength of either particulate or whisker reinforced MMCs using finite

element method [81-87]. The primary methods used are: the shear lag approach [88-90] and the dislocation-strengthening model [81,91,92]. All these studies are based on the assumption of a strong bonding between the particle and the matrix, and ideal load transfer from the matrix to the reinforcing phase. However, these studies have not considered the characteristics of the interfacial product and the nature of the interface. In most of the practical cases, the interface bonding may not be so strong and the load transfer efficiency across the interface may not be perfect [93-99]. Interface studies on MMCs have reported: (i) generation of stress and strain fields at the interface [93-95], (ii) interface of various strength and bonding [93, 95], (iii) interface damage and cracking [86], and (iv) interface products due to chemical reaction, or due to precipitation during heat treatment [96, 97]. In view of these observations, it can be inferred that the interface bonding and its thickness could vary depending on the matrix-reinforcement system, processing parameters and processing routes. According to Kennedy and Wyatt [95], interface bonding strength in Al-TiCp composites varies significantly with manufacturing route. They reported the least damage accumulation leading to strong composites in cast conditions. The squeeze cast composite provides stronger interface as compared to gravity cast composite [97]. It is further reported [95] that the modulus as well as the work hardening rate of the composites decreases with increase in deformation. Lee et al. [85] simulated the interface between the matrix and the particle as weak or strong by applying the basic Coulomb frictional model at the interface. According to this model, the strength of the interface is modulated by the critical shear strength of the interfacial layer and the orientation of the interface. Besides, Aghdam and Falahatgar [86] simulated the fiber reinforced composite using a representative volume element. In this study they varied the interface strength by varying

the mechanical and physical properties. Thus it is expected from the above discussion that due to the presence of stress or strain field at the interface and the variation of the processing route, the interface bonding strength or its coherency with the matrix may vary. Furthermore, many attempts have been made to understand the plastic flow behaviour of MMCs and to predict their flow stress by analytical methods [90-92]. Some numerical studies have shown that a significant level of hydrostatic stresses develop in the composite matrix due to constrained plastic flow [79-80]. Different levels of plastic flow control the basic failure mechanism of metal matrix composites such as matrix void nucleation, growth and coalescence, reinforcement fracture and interface debonding between matrix and reinforcement. A great deal of research has addressed the fiber/whisker orientation effect on elastic properties and overall strength of the composites by using finite element method, especially for the randomly oriented fiber composite [99-103]. These numerical results have shown that the strength of the composite is strongly influenced by the distribution of the reinforcement. The strength of MMCs is greatly influenced by stress transfer between short fiber/whisker and the matrix alloy. In addition, the whisker direction and interfacial bond has a remarkable effect on stress transfer between matrix and reinforcement. Good interfacial bonding enhances the stress transfer between matrix and reinforcement which results increase of the overall strength of the composites [101]. Several researchers have also carried out numerical simulation which allowed the study of reinforcement clustering effect on the failure mechanism in MMCs. Geni and Kikuchi [104] obtained through a simulation an ultimate strain lower for clustered MMC than for an un-clustered one. Li et al. [105] showed experimentally and verified by simulation on an Al/SiC_p composite that rupture localizes preferentially in particle-rich regions. Moreover, Tszeng [106] modeled

MMC in order to point out the influence of some cluster characteristics. This simulation showed that the elastic strength decreases as the cluster aspect ratio increases, the load at which crack nucleation occurs is lower in the cluster than outside. Zhang et al [107] have analyzed the effect of particle clustering on the flow behaviour of SiC particulate reinforced Al-MMC by using the microstructure based cell model. They successfully predicted the flow behaviour and revealed that the percentage of the particle cracking in the particle clustering model is higher compared with that in the particle random distribution model.

At present number of researches have been employed the numerical analysis to predict the effects of reinforcements on the fatigue and fracture behaviour of the MMCs. By and large, these analyses approached the problem by considering the unit cell model, where one particle or whisker was embedded in matrix [108, 110]. In addition, the shape of the particle or whisker was assumed to be cylindrical, spherical, rectangular or cubical [110, 111]. However, the above discussion concerning the prediction of damage initiation and fracture weigh in favor of either particulate- or whisker-reinforced MMCs. The numerical analysis for fatigue fracture behaviour in hybrid MMC is rare. The effect of reinforcement clustering on the initiation of microcracks in hybrid MMC is very complicated due to the presence of particles and whiskers together. Due to the complicated microstructure, various experimental and numerical investigations are needed to be explained to clarify the damage nucleation and fracture mechanism of the cast hybrid MMC.

The aim of this chapter is to investigate the stress distribution around the interface of particle-matrix and whisker-matrix located in the reinforcement clustering and non-clustering regions in the cast hybrid MMC and to analyze the hybrid effect and reinforcement clustering effect on microcrack initiation mechanism in cast hybrid MMC.

Many researchers have successfully predicted the failure mechanism (particle fracture, debonding and matrix void nucleation) of composites [75-79] by using 2-D periodic cell models with realistic microstructural arrangements within the cell. There is only limited study on 3-D inclusion model which were used for describing the reinforcement effect on strength, ductility and fracture mechanism in MMCs [80, 112, 113]. Therefore, this chapter describes the characteristics of the elastic-plastic stress field by using 3-D unit cell model of hybrid MMC

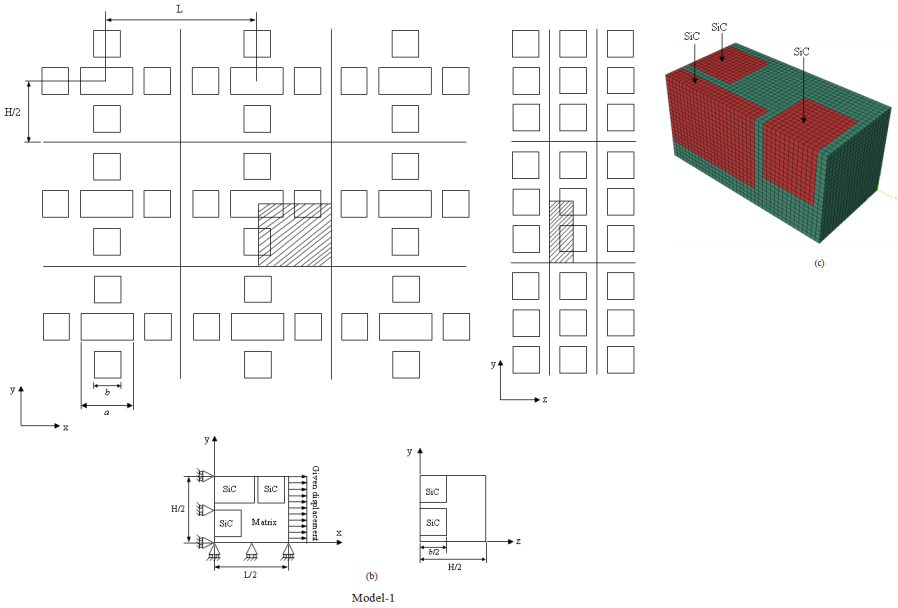

Fig. 4.1 Model-1 representing SiC particles reinforced clustering region with 58 vol% of reinforcement in hybrid MMC: (a) schematic illustration of the periodic particle and whisker arrangement (b) 1/8 of one unit cell, analysis based on symmetry (c) finite element mesh.

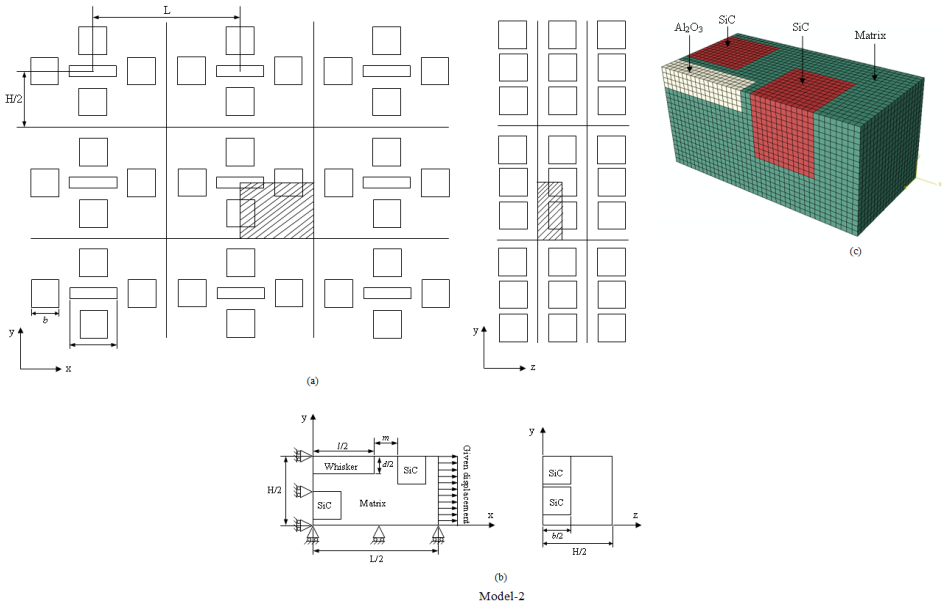

Fig. 4.2 Model-2 representing reinforcement clustering region (SiC particles and Al_2O_3 whisker) with 51 vol% of reinforcement in hybrid MMC: (a) schematic illustration of the periodic particle and whisker arrangement (b) 1/8 of one unit cell, analysis based on symmetry (c) finite element mesh.

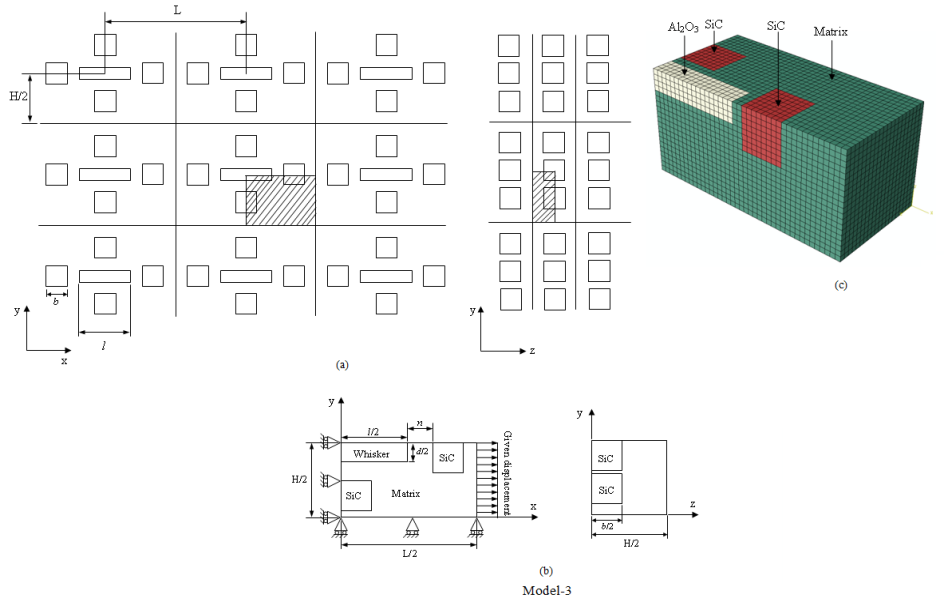

Fig. 4.3 Model-3 representing reinforcement clustering region (SiC particles and Al_2O_3 whisker) with 30 vol% of reinforcement in hybrid MMC: (a) schematic illustration of the periodic particle and whisker arrangement (b) 1/8 of one unit cell, analysis based on symmetry (c) finite element mesh.

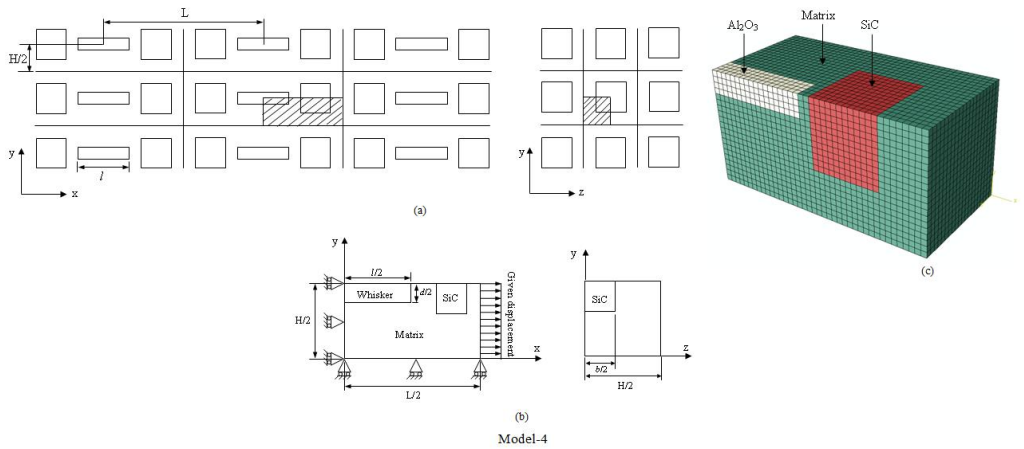

Fig. 4.4 Model-4 representing the non-clustering region of hybrid MMC where particle and whisker is placed in series: (a) schematic illustration of the periodic particle and whisker arrangement (b) 1/8 of one unit cell, analysis based on symmetry (c) finite element mesh.

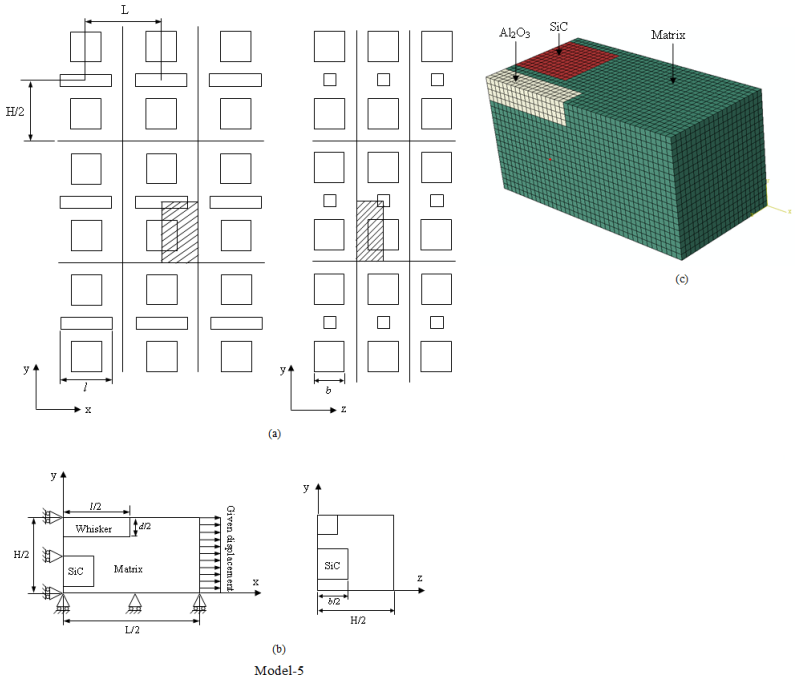

Fig. 4.5 Model-5 representing the non-clustering region of hybrid MMC where particle and whisker is placed in parallel: (a) schematic illustration of the periodic particle and whisker arrangement (b) 1/8 of one unit cell, analysis based on symmetry (c) finite element mesh.

4.2 Numerical model

To contribute to a better understanding of the stress distribution on the reinforcing particles and whiskers, and on the Al matrix in cast hybrid MMC (reinforced by SiC particles and Al_2O_3 whiskers), three-dimensional (3-D) unit cell models using finite element method (FEM) were developed. ABAQUS software [114] was used for the calculation. The models consist of SiC particles, Al_2O_3 whiskers and Al alloy matrix. The schematic illustrations and finite element mesh of the models are shown in Figs. 4.1-4.5. In this numerical analysis, it is assumed that all the SiC particles other than the center particles in model-1 are cubic shape of length *b* and the whiskers are rectangular shape of length *l* and width *d* respectively. However, the center SiC particles of model-1 (Fig. 4.1) are considered as the rectangular shape of length *a*, width *w* and height *h*. Only 1/8 of one unit cell is treated because of the symmetry of the cell. In model-1 (Fig. 4.1), SiC particulate reinforced clustering region is shown. In model-2 and 3 (Fig. 4.2 and 4.3), particles are located around a whisker, showing the clustering of both the SiC particles and Al_2O_3 whiskers, representing the hybrid clustering regions. Whereas, model-4 and 5 (Fig. 4.4 and 4.5) includes a particle and a whisker which are located in series and parallel orientation to each other, representing the non-clustering region of hybrid MMC. For models-3, 4 and 5, reinforcement volume fractions is modeled as real microstructure of hybrid MMC of 9 vol% Al_2O_3 whiskers and 21 vol% SiC particles in an Al alloy matrix. On the other hand, the reinforcement volume fraction of model-1 and model-2 is kept 58 vol% and 51 vol% respectively as the local volume fraction of the reinforcements usually increases in the clustering region. Size determination of the model was made by the following formulae:

$b^3 / LH^2 = V_p$ (for cubic shaped particle)...……(4.1)

and, $ld^2 / LH^2 = V_w$ (for whisker)…….(4.2)

where, V_p and V_w is the particle and whisker volume fraction respectively. L and H are the length of the cell in longitudinal and transverse direction respectively. The SiC particles and Al_2O_3 whiskers were modeled as linear elastic. The behaviour of Al alloy matrix was modeled as isotropic elastic-plastic response. Symmetric boundary condition is applied to the Y-Z plane at the left, X-Y plane at the front and X-Z plane at the top of the models. Moreover, periodic boundary condition is applied to the X-Z plane at the bottom and X-Y plane at the back of all the models. A uniform displacement of 0.04 μm for the half length of the unit cell, 20 μm is applied to the Y-Z plane at the right of all the models which is corresponding to a 308 MPa nominal stress for the hybrid MMC.

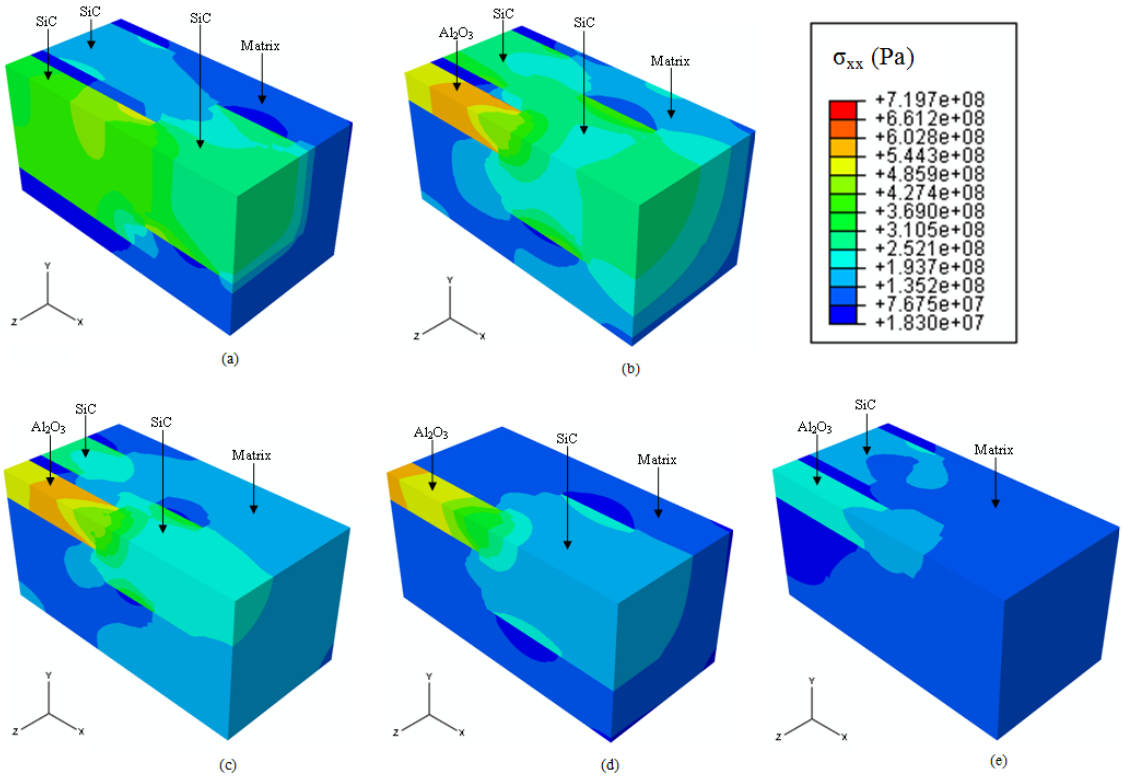

Fig. 4.6 Numerical results normal stress along loading direction (a) in the SiC particulate reinforcement clustering region model-1, (b) in the SiC particle and Al_2O_3 whisker reinforcement clustering region model-2, (c) in the SiC particle and Al_2O_3 whisker reinforcement clustering region model-3, (d) in the reinforcement non-clustering region model-4 and (e) in the reinforcement non-clustering region model-5 .

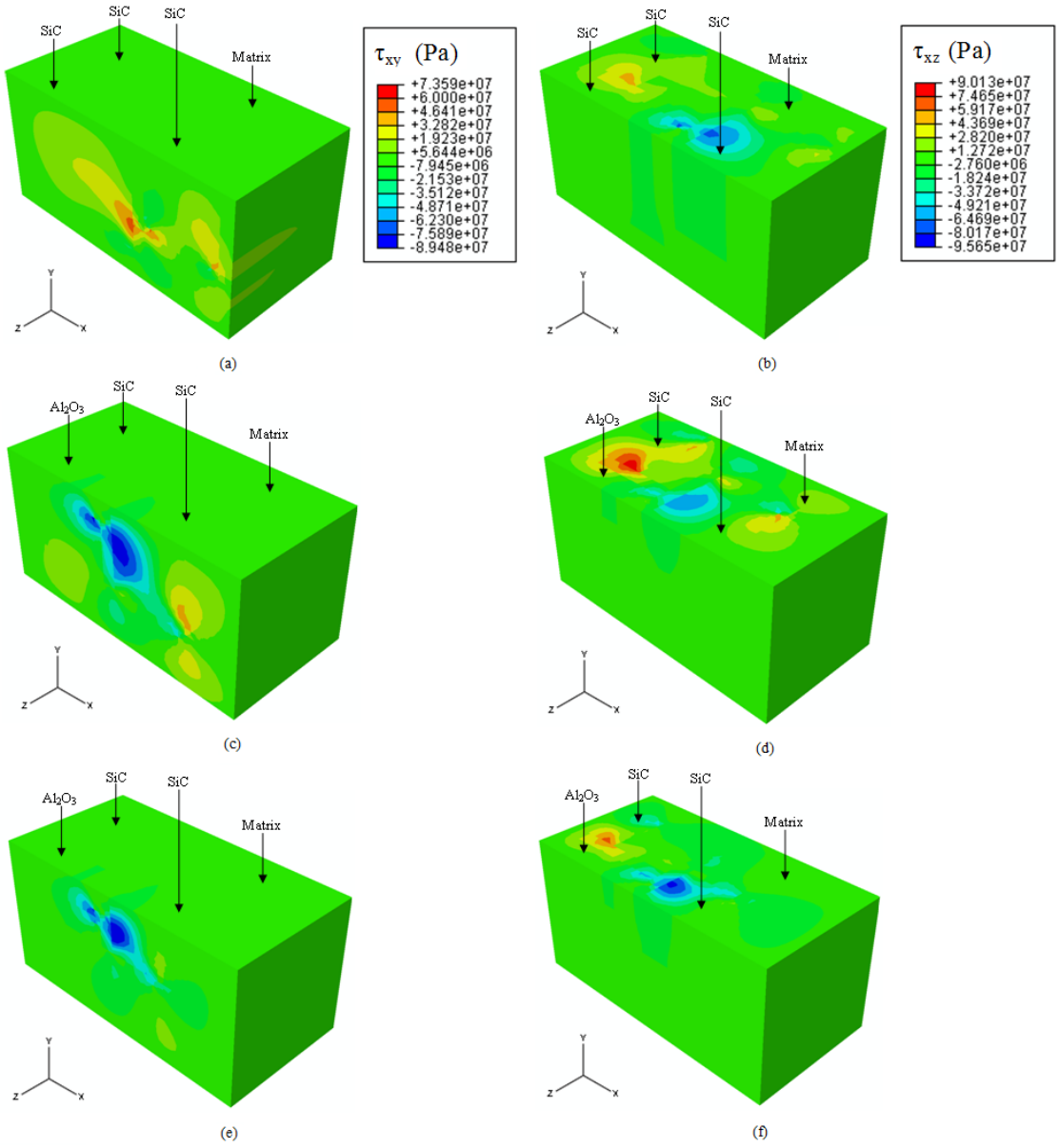

Fig. 4.7 Shear stresses developed in the clustering region of hybrid MMC (a), (c) and (e) τ_{xy} in model-1, model-2 and model-3 respectively, (b), (d) and (f) τ_{xz} in model-1, model-2 and model-3 respectively.

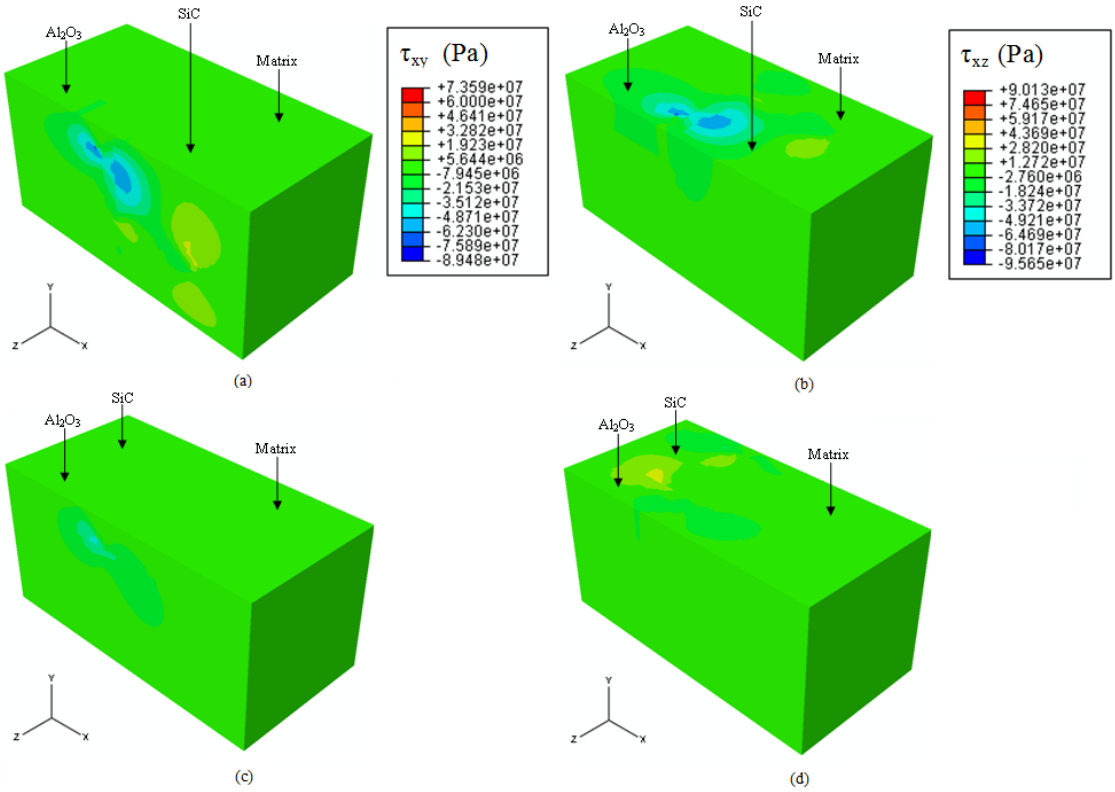

Fig. 4.8 Shear stresses developed in the non-clustering region of hybrid MMC (a), (c) τ_{xy} in model-4 and model-5 respectively, (b) and (d) τ_{xz} in model-4 and model-5 respectively

4.3 Numerical results and discussion

In order to study the crack initiation mechanism and to analyze the hybrid effect, the stress distribution in hybrid MMC is highlighted in Fig. 4.6. Figure 4.6a, b and c represent normal stresses acting along the loading direction in the reinforcement clustering regions (Model-1, 2 and 3) whereas Fig. 4.6d and e represent the normal stresses developed in the non-clustering regions (Model-4 and 5). It can be apparently found that the normal stresses developed in the reinforcement clustering regions (Fig. 4.6a, b and c) are significantly greater than that of the non-clustering regions (Fig. 4.6d and e). It is noteworthy that the

clustering regions reinforced with both SiC particles and Al_2O_3 whiskers, i.e. hybrid clustering region (model-2 and 3, Fig. 4.6b and c) experiences reasonably higher normal stresses than that of the clustering regions which is reinforced with only SiC particles (model-1, Fig. 4.6a), indicating the hybridization effect on the stress concentration and vulnerability of crack initiation in this region. Moreover, the hybrid clustering region with high volume fraction reinforcements (model-2, Fig. 4.6b) have greater stresses than that of the clustering region with low volume fraction reinforcement (model-3, Fig. 4.6c), indicating the influence of local volume fraction on the stress development in the clustering region of hybrid MMC. Besides, in all the models, the SiC particles-Al alloy interface edges experience higher stresses. This is attributed to the fact of the stress concentration in the vicinity of the reinforcement. Furthermore, the maximum stress concentration at the particle–matrix and whisker–matrix interface located in the clustering regions (Fig. 4.6b and c) is much higher than that in the non-clustering regions (Fig. 4.6d and e), suggesting the early interface debonding at the clustering regions and initiation of crack. In addition, it can be seen from Fig. 4.6b and c that the stresses developed in the particle–matrix and whisker–matrix interfaces in the areas indicated by "*m*" and "*n*" in model-2b, Fig. 4.2 and model-3b, Fig. 4.3 respectively, are reasonably higher than the stresses developed in other sides of the particle–matrix and whisker–matrix interfaces in the clustering regions. This clearly indicates the hybrid effect of the hybrid MMC. The SiC particle and Al_2O_3 whisker deform elastically within the plastically deforming Al alloy matrix. Once the particle and whisker existed very close to one another, the elastic-plastic interaction occurs between these three materials, results the higher stress concentration at this location and cracks likely to initiate in this place. Therefore, the reinforcement clustering region where SiC

particles and Al_2O_3 whisker exist very close to one another is highly vulnerable for crack initiation. The contour plots of the shear stresses developed in the hybrid MMC in both the clustering and non clustering regions are shown in Fig. 4.7 and 4.8 respectively. It can be seen that the shear stresses developed on the interface of particle–matrix and whisker–matrix in the clustering regions (Fig. 4.7) are much higher than that in the non-clustering regions (Fig. 4.8). The SiC particulate reinforced clustering regions (model-1, Fig. 4.7a and b) experiences reasonably lower shear stresses than that of the hybrid clustering regions (model-2 and 3, Fig. 4.7c, d, e and f). Moreover, the hybrid clustering region with high volume fraction reinforcements (model-2, Fig. 4.7c and d) experiences higher shear stresses than that of the clustering region with low volume fraction reinforcement (model-3, Fig. 4.7e and f), indicating the stress dependency on the reinforcement volume fraction. However, the values of the shear stresses (Fig. 4.7 and 4.8) is found to be very low than that of the normal stresses (Fig. 4.6) developed on all the models.

The comparison of the maximum normal stresses along the loading direction developed in the Al_2O_3 whisker, SiC particles and Al alloy matrix in both the clustering and non-clustering regions of hybrid MMC are shown in Fig. 4.9a. It is noteworthy that the maximum normal stresses developed in the reinforcements and matrix in the clustering regions is significantly higher than the stresses developed in the non-clustering regions. Moreover, the normal stresses developed in the SiC particle and Al-matrix in the particulate clustering region (Model-1) is relatively lower than that of the hybrid clustering regions (Model-2 and model-3). Besides, it is remarkable from Fig. 4.9a that the maximum normal stress in the Al_2O_3 whisker, SiC particle and Al alloy matrix in the reinforcement non-clustering region where SiC particle and Al_2O_3 whisker is placed in series (Model-4) are

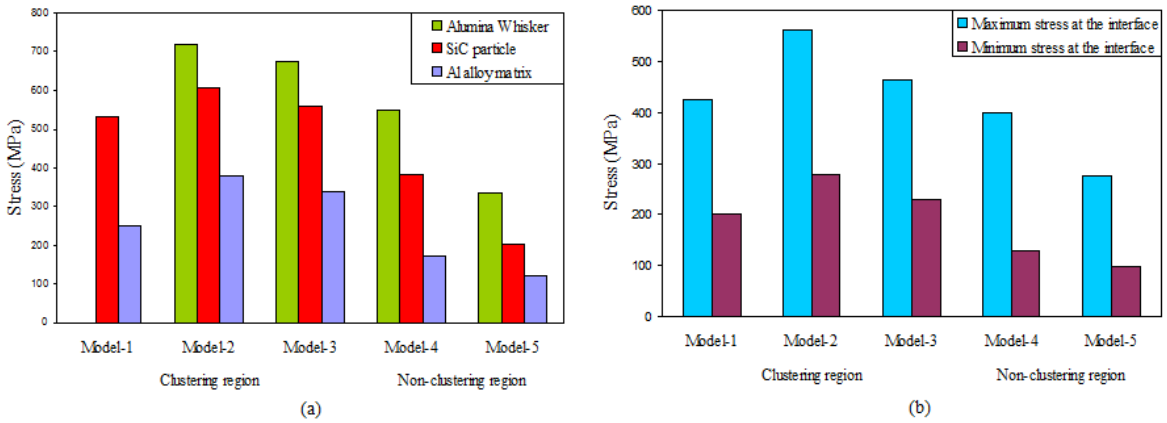

Fig. 4.9 Comparison of (a) the maximum normal stress developed in the clustering and non-clustering regions, (b) the maximum and minimum normal stresses developed on the reinforcement–matrix interfaces in the clustering and non-clustering regions.

Comparatively higher than those of the non-clustering region of model-5. From the maximum normal stress values, it is concluded that the stress is increased in the hybrid clustering region where both SiC particles and Al_2O_3 whisker is located and the location is highly sensitive to crack initiation. Figure 4.9b represents the variation of the maximum and minimum normal stresses developed on the interface of the reinforcement–matrix in all the models of both the clustering and non-clustering regions. It is obvious from Fig. 4.9b that the maximum and minimum normal stresses developed on the reinforcement–matrix interface in the clustering regions are extensively higher than that of the non-clustering regions. Moreover, from Fig. 4.9b, it is significant that the maximum normal stress on the particle–matrix interface in the reinforcement non-clustering region where SiC particle and Al_2O_3 whisker is placed in series (Model-4) are reasonably higher than those of the non-clustering region of model-5, where SiC particle and Al_2O_3 whisker is placed in parallel

orientation. Thus, it can be concluded that the reinforcements located in the clustering region experience higher stress than the non-clustering region and stress concentration at the interface of reinforcement–matrix is very high in the clustering region. In elastic state this clustering effect occurs because the ceramics have elastic stiffness one order higher than that of the Al alloy. In low cycle fatigue, elastic deformation occurred in the reinforcing SiC particles and Al_2O_3 whiskers whereas the matrix alloy deformed plastically during cyclic loading. As the reinforcements did not experience plastic deformation, the stress on the particle–matrix or whisker–matrix interfaces was higher in the hybrid MMC. In addition, the edge of the stiff ceramic reinforcements acted as stress concentrators that localizing the plastic strain between the particles and the whiskers. Thus, a large strain mismatch occurred between these two reinforcement materials and the Al alloy. For this large strain mismatch, the stress became too high on the particle–matrix interface, and cracks initiated at these locations. Moreover, it can also be concluded that the stress concentration at the reinforcements has the dependency on the reinforcement volume fraction as well as at the reinforcement–matrix interface, indicating the vulnerability of the reinforcement cluster on fatigue crack initiation.

4.4 Summery

In this chapter, the hybrid effect and reinforcement clustering effect on microcrack initiation mechanism in cast hybrid MMC reinforced with SiC particles and Al_2O_3 whiskers were discussed based on a three-dimensional (3-D) unit cell model by using finite element method (FEM). The stress distribution in the reinforcement clustering and non-clustering regions of cast hybrid MMC was presented. The numerical results showed very close agreement with the experimental results.

CHAPTER-5

CONCLUSIONS AND RECOMMENDATIONS

5.1. Conclusions

In this research, the fatigue crack initiation and propagation mechanisms as well as the crack growth behaviour in cast hybrid metal matrix composites reinforced with SiC particles and Al_2O_3 whiskers during low cycle and high cycle fatigue were investigated experimentally and numerically. The effect of hybrid reinforcement on crack initiation and early propagation mechanism in cast MMCs during low cycle fatigue was investigated. The study focused on the crack initiation cycle and the location of the microcrack formation in a smooth specimen of three types of materials: cast hybrid MMC, cast MMC with Al_2O_3 whiskers, and cast Al alloy. Moreover, the mechanism of fatigue crack growth in cast MMCs during high cycle fatigue was studied. The crack propagation behavior at the near-threshold and stable-crack-growth regions was thoroughly investigated. Moreover, the hybrid effect and the reinforcement clustering effect on the crack initiation mechanism in cast hybrid MMC were investigated numerically by using the finite element method (FEM). The key findings of this research are summarized below:

1. Four major processes were observed in the low cycle fatigue of hybrid MMC and MMC with Al_2O_3 whiskers: microcrack initiation, growth, arrest, and coalescence.

2. The addition of reinforcement changed the crack initiation site. In Al alloy, microcracks initiated in the Al grain. As Al_2O_3 whiskers were added to the Al alloy as reinforcement (as in the specimen composed of MMC with Al_2O_3 whiskers), cracks initiated at the whisker/matrix interface. When SiC particles were also added to the MMC (as in the hybrid MMC specimen), cracks originated from the particle–matrix interface.
3. In the hybrid MMC, during low cycle fatigue cracks initiated very early in the fatigue life, around 11-16% of the total fatigue life. For the MMC with Al_2O_3 whiskers, cracks originated at 16-19% of the fatigue life, and at 60-74% of the fatigue life for the Al alloy. The interaction between SiC particles and Al_2O_3 whiskers shortened the crack initiation period in the hybrid MMC, indicating that the hybridization reduced the resistance to crack initiation.
4. In Al alloy, cracks propagated through the Al grain and on the boundary between Si particle clusters and the Al grain during low cycle fatigue, whereas in hybrid MMC, cracks propagated along the SiC particle–Al alloy and Al_2O_3 whisker–Al alloy interfaces as well as through the Al alloy. Cracks moved in the MMC with Al_2O_3 whiskers such that they broke the perpendicular whiskers and debonded the parallel whiskers along the crack path.
5. The fracture mechanisms observed in both MMC materials due to low cycle fatigue loading were found to be quite similar. For both materials, the initiation of fracture was dominated by the interfacial debonding of particle–matrix and whisker–matrix interfaces followed by void nucleation in the Al alloy matrix. On the contrary, the

fatigue fracture in Al alloy was directed by plastic slip in the Al grain followed by extensive void nucleation and coalescence and striation formation in the Al grain.

6. The fatigue strength of the hybrid MMC during low cycle fatigue was found to be somewhat higher than that of the MMC with Al_2O_3 whiskers.
7. The presence of SiC particles and Al_2O_3 whiskers in very close proximity facilitates the microstructural inhomogeneity of the cast hybrid MMC. In the low ΔK region, the SiC particles either acted as barriers to cracks and or deflected the growth planes of cracks. In addition to the high elastic modulus, crack deflection gives the cast hybrid MMC better fatigue crack growth resistance than the cast MMC with Al_2O_3 whisker and the cast Al alloy in the low ΔK region during high cycle fatigue.
8. The FCG mechanism during high cycle fatigue of both MMC materials at decreasing ΔK in the near-threshold region was found to be quite similar. For both materials, FCG was dominated by the debonding of particle–matrix and whisker–matrix interfaces followed by void nucleation in the Al alloy matrix. The fatigue crack growth reached its threshold when the crack encountered the inhomogeneous distribution of the reinforcement or second-phase particles, i.e., the cluster of SiC particles and Al_2O_3 whiskers in the cast hybrid MMC, the Al_2O_3 whiskers in the cast MMC with Al_2O_3, and the cluster of Si particles in the cast Al alloy.
9. The high cycle FCG mechanism of both MMCs with increasing ΔK value in the stable- or mid-crack-growth region was the cycle-by-cycle crack growth along the particle–matrix and whisker–matrix interface, as well as by the transgranular fracture of particles and whiskers. The crack growth resistance deteriorated because of either fracture along the matrix–reinforcement interface or transgranular fracture of the

reinforcement. In addition, striation formation and void nucleation in the Al alloy matrix become the influential factor of crack growth in this region. Moreover, in the Al alloy, the FCG during higher ΔK values was controlled mainly by the striation formation owing to the availability of multiple slip systems in the large Al grains followed by the void nucleation and coalescence in the Si cluster.

10. The numerical analysis showed that the high stress was developed in the reinforcements located in the clustering region and stress concentration occurred on the particle–matrix interfaces. The stress concentration on the particle–matrix interface located in the high volume fraction reinforced hybrid clustering region is found to be very high compared to that in the SiC particulate reinforced clustering region and low volume fraction reinforced hybrid clustering region. Moreover, the non-clustering region where SiC particle and Al_2O_3 whisker located in series experienced higher stresses than that of the non-clustering region where SiC particle and Al_2O_3 whisker located in parallel orientation.
11. The high volume fraction reinforced hybrid clustering region is found to be highly vulnerable to initiate crack in cast hybrid MMC during low cycle fatigue.

5.2 Recommendations for further studies

In this research, the microcrack initiation and propagation mechanisms as well as the crack growth behaviour in cast hybrid metal matrix composites reinforced with SiC particles and Al_2O_3 whiskers during low cycle and high cycle fatigue were studied experimentally and the results were validated by the use of numerical simulation. The hybridization effect on microcrack initiation and early propagation mechanism in cast

MMCs during low cycle fatigue was thoroughly investigated. In addition, the fatigue crack propagation behavior at the near-threshold and stable-crack-growth regions during high cycle fatigue was also studied. However, there are still few areas which need to be addressed more meticulously to get the clear knowledge on the fracture behaviour of cast hybrid MMC. Some of the areas for future investigation are recommended as follows:

1. The load ratio has significant effect on the fatigue crack growth behaviour. In this research, constant load ratio, R= 0.1 was used. Therefore, further research can be carried out to investigate the effect of load ratio in the microcrack initiation and propagation mechanism in cast hybrid MMC.
2. The phenomena of fatigue crack growth may change in the boundary when crack moves from homogeneous MMC material to Al alloy part. In this research, the fatigue crack initiation and propagation mechanism were investigated in the homogeneous MMC materials. Therefore, further research can be carried out to investigate the crack growth phenomena at the boundary between cast hybrid MMC and Al alloy.
3. The present research did not investigate the residual stress in the hybrid MMC that may occur during fatigue loading. Therefore, the future research may investigate the residual stress in the hybrid MMC.

REFERENCES

[1] Suresh S, Mortensen A, Needleman A. Fundamentals of metal matrix composites. London: Butterworth/Heinemann;1993.

[2] Kainer KU. Basic of metal matrix composite, in custom made materials for automotive and aerospace engineering. Wiley-VCH Verlag Gmbh and Co. Weinheim;2006.

[3] Maxwel PB, Martins GP, Olsen DS, Edwards GR. The infiltration of aluminium into silicon carbide compacts. Metall Trans 1990;21B:475-85.

[4] Clyne TW, Manson JF. The squeeze infiltration process for fabrication of metal matrix composites. Metall Trans A 1987;18A:1519-30.

[5] Miracle DB. Metal matrix composite-from science to technological significance. Compos Sci Technol 2005;65:2526-40.

[6] Zeuner T, Stojanov P, Sahm PR, Ruppert H, Engels A. Developing trends in disc brake technology for rail application. Mater Sci Technol A 1998;14:857-63.

[7] Davis Jr. Metals handbook. ASM international 1998;657-63.

[8] Llorca J. Fatigue of particle and whisker reinforced metal matrix composites. Prog Mater Sci 2002;47:283-353.

[9] Harris SJ, Wilks TE. Fibre Reinforced Composites. Mech Eng Publ 1986;19-28.

[10] Davidson DL. Fatigue and fracture toughness of aluminium alloys reinforced with SiC and alumina particles. Compos 1993;24:248-55.

[11] Bonnen JJ, Allison JE, Jones JW. Fatigue behaviour of 2xxx series aluminium alloy reinforced with 15 vol % SiC_p. Metall Trans A 1991;22:1007-19.

[12] Mkaddem A, Mansori M. On fatigue crack growth mechanisms of MMC: Reflection on analysis of 'multi surface initiations'. Mater Des 2009;30:3518-24.

[13] Larid C. The influence of metallurgical structure on the mechanism of fatigue crack propagation. ASTM STP 1967;425:131-80.

[14] Suresh S. Fatigue of materials. Cambridge: Cambridge University Press 1991.

[15] Poza P, Llorca J. Mechanical behavior and failure micro-mechanisms of Al/Al_2O_3 composites under cyclic deformation. Metall mater Trans A 1995;26A: 3131-41, 1995. 62

[16] Llorca J, Poza P. Influence of reinforcement fracture on the cyclic stress-strain curve of metal matrix composites. Acta Metall Mater 1995;43:3959-69.

[17] Poza P, Llorca J. Mechanical behaviour of Al-Li-SiC composites: part 1. Microstructure and tensile deformation. Metall Mater Trans A 1999;30:845-55.

[18] Li C, Ellyin F. Fatigue damage and its localization in particulate metal matrix composites. Mater Sci Eng 1996;A214:115.

[19] Singh PM, Lewandowski JJ. The effects of reinforcement additions and heat treatment on the evolution of poisson's ratio during straining of discontinuously reinforced aluminium alloys. Metall Mater Trans A 1995;26:2911-21.

[20] Bao G, Hutchinson WJ, Mcmeeking RM. Particle reinforcement of ductile matrices against plastic flow and creep. Acta Metall Mater 1991;39:1871-82

[21] Llorca J. A numerical study of the mechanisms of cyclic strain hardening in metal-ceramic composites. Acta Metall Mater 1994;42:151-62.

[22] Chen EY, Lawson L, Meshii M. The effect of fatigue microcracks on rapid catastrophic failure in Al-SiC composites. Mater Sci Eng A 1995;200:192-206.

[23] Sasaki M, Lawson L, Meshii M. Low cycle fatigue properties of a SiC whisker-reinforced 2124 aluminium alloy. Metall Mater Trans A1994;25:2265-74.

[24] Chawla N, Andres C, Jones JW, Allison JE. Effect of SiC volume fraction and particle size on the fatigue resistance of a 2080 Al/SiCp composite. Metall Mater Trans A 1998;29:2843-54.

[25] Levin M, Karlsson B. Crack initiation and growth during low cycle fatigue of discontinuously reinforced metal matrix composites. Int J fatigue 1993;15:377-87.

[26] Chen ZZ, Tokaji K. Effects of particle size on fatigue crack initiation and small crack growth in SiC-particulate reinforced aluminium matrix composites. Mater Lett 2004;58:2314-21.

[27] Williams DR, Fine ME. Proceedings of the 5th International Conference on Composite Materials. Harrigan WC, Strife J, Chingra AK eds., TMS, Warrendale PA 1985;639-70.

[28] Ochi Y, Masaki K, Matsumura T, Wadasako M. Effects of volume fraction of alumina short fibers on high cycle fatigue properties of Al and Mg alloy composites. Mater Sci Eng A 2007;468:230–36

[29] Kumai S, King JE, Knott JF. Fatigue in SiC-particulate-reinforced aluminum alloy composites. Mater Sci Eng A 1991;146:317-26.

[30] Wang Z. Fatigue of particulate ceramics reinforced metal matrix composites. Key Eng Mater 1995;104:765-90.

[31] Davidson DL. Effect of particulate SiC on fatigue crack growth in a cast extruded aluminum alloy composite. Metall Trans A 1991;22:97-112.

[32] Kumai S, King JE, Knott JF. Fatigue crack growth behavior in molten-metal processed SiC particle-reinforced aluminum alloys. Fatigue Fract Eng Mater Struct 1992;15:1-11.

[33] Sugimura Y, Suresh S. Effects of SiC content of fatigue crack growth in aluminum alloys reinforced with SiC particles. Metall Trans A 1992;23:2231-42.

[34] Chawla N, Ganesh VV. Fatigue crack growth of SiC particle reinforced metal matrix composites. Int J Fatigue 2010;32:856-63.

[35] Wang Z, Zhang RJ. Microscopic characteristics of fatigue crack propagation in aluminum alloy based particulate reinforced metal matrix composites. Acta Metall 1994;42:1433-45.

[36] Liu G, Shang JK. Fatigue crack tip opening behavior in particulate reinforced Al alloy composites. Acta Metall 1996;44:79-91.

[37] Crawford BR, Griffiths JR. Role of reinforcement particles during fatigue cracking of a micral-20-reinforced 6061 alloy. Fatigue Fract Eng Mater Struct 1999;22:811-20.

[38] Shang JK, Yu W, Ritchie RO. Role of silicon carbide particles in fatigue crack growth in SiC-particulate-reinforced aluminum alloy composites. Mater Sci Eng A 1988;102:181-92.

[39] Mason JJ, Ritchie RO. Fatigue crack growth resistance in SiC particulate and whisker reinforced P/M 2124 aluminum matrix composites. Mater Sci Eng A 1997;231:170-82.

[40] Botstein O, Arone R, Shpigler B. Fatigue crack growth mechanisms in Al-SiC particulate metal matrix composites. Mater Sci Eng A 1990;128:15-22.

[41] Knowles DM, King JE. The influence of ageing on fatigue crack growth in SiC particulate reinforced 8090 Al alloy. Acta Metall Mater 1991;39:793-806.

[42] Liaw PK, Leax TR, Logsdon WA. Near-threshold fatigue crack growth behaviour in metals. Acta Mater 1983;31:1581-7.

[43] Kumai S, Yoshida K, Higo Y, Nunomura S. Effects of the particle distribution on fatigue crack growth in particulate SiC/6061 aluminum alloy composites. Int J Fatigue 1992;14:105-12.

[44] Davidson DL. The growth of fatigue cracks through particulate SiC reinforced aluminum alloys. Eng Fract Mech 1989;33:965-77.

[45] Shang JK, Ritchie RO. On the particle-size dependence of fatigue-crack propagation thresholds in SiC-particulate-reinforced aluminum-alloy composites: role of crack closure and crack trapping. Acta Metall 1989;37:2267-78.

[46] Xu XX, King JE, Bhattacharjee D. Crack deflection during fatigue and monotonic fracture of a SiC whisker reinforced 2009 aluminium alloy. Acta Metal Mater 1994;42: 2353-63.

[47] Oh KH, Han KS. Short-fiber/particle hybrid reinforcement: Effects on fracture toughness and fatigue crack growth of metal matrix composites. Compos Sci Technol 2007;67:1719-26.

[48] Chen AL, Arai Y, Tsuchida E. An experimental study on effect of thermal cycling on monotonic and cyclic response of cast aluminum alloy-SiC particulate composites. Compos Part B 2005;36:319-30.

[49] Chen AL, Arai Y, Tsuchida E. A numerical study on effect of thermal cycling on monotonic and cyclic response of cast aluminum alloy-SiC particulate composites. Theoretical App Mech 2004;53:63-73

[50] Srivatsan TS, Al-Hajiri M. The fatigue and final fracture behavior of SiC particle reinforced 7034 aluminum matrix composites. Compos Part B 2002;33:391-404.

[51] Zhang Q, Zhang H, Mingyuan G, Yanping J. Studies on the fracture and flexural strength of Al/Si_p composite. Mater Lett 2004;58:3545-50.

[52] Xu XQ, Watt DF. A finite element analysis of plastic relaxation and plastic accumulation at second phase particles. Acta Mater 1996;44:801-11.

[53] Xu XQ, Watt DF. A numerical analysis of the effects of reinforcement content on strength and ductility in $Al/(SiC)_p$ MMCs. Acta Mater 1996;44:4501-11.

[54] Llorca L, Suresh S, Needleman A. An experimental and numerical study of cyclic deformation in metal-matrix composites. Metall Trans A 1992;23A:919-34.

[55] Llorca L, Needleman A, Suresh S. An analysis of the effects of matrix void growth on deformation and ductility in metal-ceramic composites. Acta Metall Mater 1991;39:2317-35.

[56] Christman T, Needleman A, Suresh S. An experimental and numerical study of deformation in metal-ceramic composites. Acta Mater 1989;37:3029-50.

[57] Song JI, Bae SI, Ham KC, Han KS. Abrasive wear behavior of hybrid metal matrix composites. Key Eng Mater 2000;183:1267-72.

[58] Fu H, Han K, Song J. Wear properties of saffil/Al, saffil/Al_2O_3/Al and saffil/SiC/Al hybrid metal matrix composites. Wear 2004;256:705-13.

[59] Jung SW, Lee JH, Nam JB, Nam HW, Han KS. Analysis of strengthening mechanism in hybrid short fiber/particle reinforced metal matrix composites. Key Eng Mater 2000;183:1297-1302.

[60] Zhang XN, Geng L, Wang GS. Fabrication of Al-based hybrid composites reinforced with SiC whiskers and SiC nanoparticles by squeeze casting. J Mater Proc Technol 2006;176:146-51.

[61] Jiang JQ, Liu HN, Ma AP, Tan RS. The structure and tensile properties of Al-Si alloy hybrid reinforced with alumina-aluminosilicate short fiber. J Mater Sci 1994;29:3767-73.

[62] Gurcan AB, Baker TN. Wear behaviour of AA6061 aluminium alloy and its composites. Wear 1991;188:185-91.

[63] Rafiquzzaman MD, Arai Y, Tsuchida E. Fracture mechanism of aluminium cast alloy locally reinforced by SiC particles and Al_2O_3 whiskers under monotonic and cyclic load. Mater Sci Technol 2008;24:273-80.

[64] Rafiquzzaman Md, Arai Y. Hybrid effect on whisker orientation dependence of composite strength of aluminum cast alloy reinforced by Al_2O_3 whiskers and SiC particles. J Solid Mech Mater Eng 2010;4:303-14.

[65] Ibrahim IA, Mohamed FA, Lavernia EJ. Partculate reinforced metal matrix composites- A review. J Mater Sci 1991;26:1137-56.

[66] Kaczmar JW, Pietrzak K, Wlosinski W. The production and application of metal matrix composite materials. J mater Proc Technol 2000;106:58-67.

[67] Cornie JA. Advanced pressure infiltration casting technology produces near absolute net shape MMC components cost competitively. Mater Technol 1995;10:43-58.

[68] 'Aluminium Alloy casting', JIS H5202. Japan Industrial Standard; 2002.

[69] 'Mex 5.1, Alicona Imaging GmbH'.

[70] Anderson TL. Fracture Mechanics: Fundamentals and applications. CRC press 1995.

[71] Bruzzi MS, McHugh PE. Micromechanical investigation of the fatigue crack growth behaviour of Al-SiC MMCs. Int J Fatigue 2004;26:795-804.

[72] Meggiolaroa MA, Mirandab ACO, Castroa JTP, Marthac LF. Crack retardation equations for the propagation of branched fatigue cracks. Int J Fatigue 2005;27:1398-407.

[73] Lawson L, Chen EY, Meshii M. Near threshold fatigue: a review. Int J fatigue 1999;21:15-34.

[74] Wasen J, Heier E. Fatigue crack growth thresholds-the influence of young's modulus and fracture surface roughness. Int J fatigue 1988;20:737-42.

[75] Chen AL, Arai Y, Tsuchida E. A numerical study on effect of thermal cycling on monotonic and cyclic response of cast aluminum alloy-SiC particulate composites. Theoretical App Mech 2004:53:63-73.

[76] Llorca L, Suresh S, Needleman A. An experimental and numerical study of cyclic deformation in metal-matrix composites. Metall Trans A 1992;23A:919-34.

[77] Llorca L, Needleman A, Suresh S. An analysis of the effects of matrix void growth on deformation and ductility in metal-ceramic composites. Acta Metall Mater1991;39:2317-35.

[78] Christman T, Needleman A, Suresh S. An experimental and numerical study of deformation in metal-ceramic composites. Acta Mater 1989;37:3029-50.

[79] Borbely A, Biermann H, Hartmann O. FE investigation of the effect of particle distribution on the uniaxial stress-strain behavior of particulate reinforced metal-matrix composites. Mater Sci Eng A 2001;313:34-45.

[80] Watt DF, Xu XQ, Llyod DJ. Effect of particle morphology and spacing on the strain fields in a plastically deforming matrix. Acta Mater 1996;44:789-99.

[81] Mondal DP. Ramakrisnan N, Das S. FEM modeling of the interface and its effect on the elasto-plastic behaviour of metal matrix composites. Mater Sci Eng A 2006;433:286-90.

[82] Kamat SV, Rollet AD, Hirth JP. Plastic Deformation in Al-Alloy Matrix-Alumina Particulate Composites. Scripta Metall Mater 1991;25:27-32.

[83] Varma VK, Kamat SV, Kutumbarao VV. Tensile behaviour of powder metallurgy processed (Al–Cu–Mg)/SiCp composites. Mater Sci Technol 2000;17:93-101.

[84] Preuss M, Rauchs G, Withers PJ. Maire E, Buffiere JY. Interfacial shear strength of Ti/SiC fibre composites measured by synchrotron strain measurement. Compos Part A: Applied Science and Manufacturing 2002;33A:1381-85.

[85] Lee JH, Maeng DY, Hong SI, Won CW. Prediction of cracking mode and hardening behaviour of MMC via FEM. Mater Sci Eng A 2003;339:175-82.

[86] Aghdam MM, Falahatgar SR. Micromechanical modeling of interface damage of metal matrix composites subjected to transverse loading. Composites Struct 2004;66:415-20.

[87] Mammoli AA, Bush MB, effects of reinforcement geometry on the elastic and plastic behaviour of metal matrix composites. Acta Metall Mater 1995;43:3743-54.

[88] Balashivananda SP, Karunamoorthy L, Kandasami GS. A finite element analysis study of micromechanical interfacial characteristics of metal matrix composites. J Mater Proc Technol 2004;153:992-97.

[89] Craig LH. Three-dimensional finite element analysis of plastic deformation in a whisker-reinforced metal matrix composite. J Mech phy solids 1992;40:991-1008.

[90] Ganesh VV, Chawla N. Effect of particle orientation anisotropy on the tensile behaviour of metal matrix composites: experiments and microstructure based simulation. Mater Sci Eng A 2005;391:342-53.

[91] Zhu HT, Zbib HM. Strain gradients and continuum modeling of size effect in metal matrix composites. Acta Mechanica 1997;121:165-71.

[92] Ramakrishnan N. An analytical study on strengthening of particulate reinforced metal matrix composites. Acta Mater 1996;44:69-77.

[93] Jiang QC, Li XL, Wang HY. Fabrication of TiC particulate reinforced magnesium matrix composites. Scripta materialia 2003;48:713-17.

[94] Xing YM, Tanaka Y, Kishimoto S, Shinya N. Determining interfacial thermal residual stress in SiC/Ti-15-3 composites. Scripta Mater 2003;48:701-6.

[95] Kennedy AR, Wyatt SM. Characterizing particle-matrix interfacial bonding in particulate Al-TiC MMCs produced by different methods. Compos Part A 2001;32:555-59.

[96] Silvain JF, Proult A, Lahaye M, Douin J. Microstructure and chemical analysis of C/Cu/Al interface zone. Compos Part A 2003;34:1143-49.

[97] Vicens J, Chedru M, Chermant JL. New Al-AlN composites fabricated by squeeze casting: interfacial phenomena. Compos Part A 2002;33:1421-23.

[98] Ho S, Sagai A. Three-dimensional modeling of thermal residual stresses and mechanical behaviour of cast Al/SiC composites. Mater Sci Eng A 1994;183:39-47.

[99] Nutt SR, Needleman A. Void nucleation at fiber ends in Al-SiC composites. Scripta Metall 1987;21:705-10.

[100] Arsenault RJ, Flom Y. Proc. Symp. Phase Boundary Effects on Deformation. TMS, AIME, Toronto, Canada 1985:261-79.

[101] Guo-Zheng, Kang, Quing Gao. Tensile properties of randomly oriented short δ-Al_2O_3 fiber reinforced aluminium alloy composites: 2. Finite element analysis for stress transfer, elastic modulus and stress-strain curve. Compos part A 2002;33:657-67.

[102] Li AB, Geng L, Meng QY, Zhang J. Simulation of the large compressive deformation of the metal matrix composites with misaligned whiskers. Mater Sci Eng A 2003;358:324-33.

[103] Levy A, Papazian JM. Tensile properties of short fiber-reinforced SiC/Al composites: part 2 Finite-Element analysis. Metall Trans A 1990;21:411-20.

[104] Geni M, Kikuchi M. Damage analysis of aluminium matrix composite considering non uniform distribution of SiC particles. Acta Mater 1998;46(9):3125-33.

[105] Li M, Ghosh S, Richmond O. An experimental–computational approach to the investigation of damage evolution in discontinuously reinforced aluminium matrix composite. Acta Mater 1999;12(47):3515-32.

[106] Tzeng TC. The effect of particle clustering on the mechanical behaviour of particle reinforced composites. Compos part B 1998;29B:299-308.

[107] Zhang P, Li F. Effects of particle clustering on the flow behaviour of SiC particle reinforced Al metal matrix composites. Rare Metal Mater Eng 2010;39(9):1525-31.

[108] Zhang WX, Li LX, Wang TJ, Interphase effect on the strengthening behaviour of particle-reinforced metal matrix composites. Computational Mater Sci 2007;41: 145-55

[109] Yan YW, Geng L, Li AB. Experimental and numerical studies of the effect of particle size on the deformation behaviour of metal matrix composites. Mater Sci Eng A 2007;448:315-325.

[110] Xu, Na; Zong, Yaping; Zhang, Fang. Acta Metallurgica Sinica, 2007, 43: 863

[111] Yu, Jingyu; Li, Yulong; Zhou, Hongxia. Acta Materiae Compositae Sinica, 2005, 22: 31

[112] Xu XQ, Watt DF. A finite element analysis of plastic relaxation and plastic accumulation at second phase particles. Acta Mater 1996;44:801-11.

[113] Xu XQ, Watt DF. A numerical analysis of the effects of reinforcement content on strength and ductility in Al/$(SiC)_p$ MMCs. Acta Mater 1996;44:4501-11.

[114] ABAQUS 6.9, Dassault Systems, 2009.